UCSF
UC San Francisco Electronic Theses and Dissertations

Title
Advanced H-1 Lung Magnetic Resonance Imaging

Permalink
https://escholarship.org/uc/item/5n69x8rg

Author
Zhu, Xucheng

Publication Date
2020

Peer reviewed|Thesis/dissertation

Advanced H-1 Lung Magnetic Resonance Imaging

by

Xucheng Zhu

DISSERTATION
Submitted in partial satisfaction of the requirements for degree of
DOCTOR OF PHILOSOPHY

in

Bioengineering

in the

GRADUATE DIVISION

of the

UNIVERSITY OF CALIFORNIA, SAN FRANCISCO
AND
UNIVERSITY OF CALIFORNIA, BERKELEY

Approved:

DocuSigned by:

_____   Peder Larson
1644A2CD853841E...   Chair

DocuSigned by:

_____   Youngho Seo
DocuSigned by:5484...

_____   Thomas Hope
121B032C6073427...

_____

_____
                                                          Committee Members

Dedicated to my parents,

Lan Chen and Shijing Zhu

Acknowledgements

Every time I read others dissertations, I would first read the acknowledgements. Right now, I feel very excited because I am actually writing this section.

First and foremost, I'd like to thank my advisor, Peder Larson, for being a fantastic mentor during my PhD. Even though his schedule is tight every day, he would squeeze the time out to meet with me and make sure I'm on the right track. In addition, Peder always gives me a great degree of independence to do research and build collaborations. And he always encourages and supports me to attend different seminars and workshops to broaden my vision. When I was close to graduation, he gave me lots of suggestions and connected me to other faculty. Without him, this dissertation was not made possible.

And I'd like to thank Michael (Miki) Lustig and Kevin Johnson. Miki is very good teacher, he can always explain things in a very clear way. I did my one of the first-year rotations with Miki. Every time I met with him, he tried to push my work a little further. Even after my rotation, I still work very closely with Miki. Some ideas in this dissertation are from the conversations with Miki. And I met Kevin in 2018 when I attended the GE pulse sequence workshop. Kevin is one of the pulse sequence masters I've ever known. After the workshop, I spent two weeks in his lab and learned a lot of advanced pulse sequence techniques, which made my research much easier.

I would also like to thank Dan Vigneron, who serves as my graduate advisor as well as my qualifying exam committee chair. I'm very impressed by his passion towards science and academic leadership. I would not be surprised if Dan can come up with a

Many thanks go to my research colleagues. Fei Tan, Andrew Leynes, Qing Dai, Nikhil Deveshwar, Nick Dwork, Manuska Vaidya, Kirti Magudia, Abhejit Rajagopal, Jess Scholey from Peder's Lab. And Jon Tamir, Karthik Gopalan, Alan Dong, Michael Kellman, Ke Wang, Ekin Karasan, and Suma Anand from Miki's lab. Hong Shang, Zihan Zhu, Hsin-Yu Chen, Brian Chung, Philip Lee, Jasmine Graham, and Yaewon Kim from Dan's group. Renuka Sriram, Dave Korenchan and Jinny Sun from John's lab.

And I also want to thank Jenny Che, Ana Maria Deluca, Kim Semien, SarahJane Taylor, Kristin Olson, and Kevin Long for all their kind administrative support in the past few years.

I would like to thank my friends at Berkeley as well as UCSF: Xiang Gao, Yicheng chen, Dan Shen, Ruoxing Lei, Bingqi Tong, Rui Yan, Xingjie Pan. I would also like to thank Qing Ye, Wenzhang Xie, Zhilong Pan, Jiayue Wang, Lianxiao Xue, my undergrad colleagues and friends, for their friendship and support remotely!

Lastly, I'd like to end this section with thanks to my grandparents, and parents. Without their unconditional love and support, I cannot have made everything happen today. I am grateful for their encouragement, sacrifices, and support!

Xucheng Zhu

March, 2020

Abstract

Advanced ^{1}H Lung Magnetic Resonance Imaging

By Xucheng Zhu

Doctor of Philosophy in Bioengineering

University of California, San Francisco and University of California, Berkeley

Professor Peder E.Z. Larson, Chair

Magnetic resonance imaging (MRI) is one of the widely used medical imaging modalities, since it can provide both structural and functional assessment in a single imaging session.

However, two major challenges should be addressed when using MRI for lung imaging. The first challenge is the intrinsic low SNR of ^{1}H lung MRI due to the low proton density as well as the fast decay of the lung parenchyma signal. And the second challenge is subject motion. To achieve high resolution structural image, MRI requires a long scan time, usually a few minutes or even longer, which make MRI sensitive to subject motion.

To address the first challenge, an ultra-short echo time (UTE) MRI sequence is used to capture the lung parenchyma signal before it decays.

As for subject motion, two major strategies are widely used. One strategy is fast breath-holding scan, in which the subjects are asked to hold their breath for a short duration, and the fast 3D MR sequence would be used to acquire data within that duration. This dissertation proposes a new acquisition scheme based on the standard UTE sequence, which could largely increase the encoding efficiency and improve the breath-holding scan images.

The other is free breathing scan with motion correction. The subjects are allowed to breathe during the MR acquisition. After the acquisition, the motion corrupted data would go through a motion correction step to reconstruct motion free images. In this dissertation, two novel motion correction reconstruction strategies are proposed to incorporate the motion modeling and compensation into the reconstruction to get high SNR motion corrected 3D and 4D images.

When translating the developed techniques to clinical studies, specifically for pediatric and neonatal studies, more practical problems need to be considered, such as smaller but finer anatomy to image, the different respiratory patterns of the young subjects etc. This dissertation proposes a 5-minute free breathing UTE MRI strategy to acquire a 3D high resolution motion free lung image for pediatric and neonatal studies.

Table of Contents

List of Figures

List of Tables

Introduction

Magnetic resonance imaging (MRI) is one of the widely used medical imaging modalities, since it can not only provide high spatial resolution structural information, but also functional information. Clinically, MRI has a broad range of applications, such as distinguishing and staging tumors[1,2], detecting neurodegenerative disorders[3,4], as well as assessing the structure and the function of the heart[5,6], etc.

However, to assess lung anatomy, Computed tomography (CT) is still the standard imaging technique[7,8], which can achieve high spatial resolution images within a few seconds. However, ionizing radiation exposure is one of the major concerns with CT , especially for neonatal and pediatric patients[9–11]. MRI would be an alternative to CT for neonatal and pediatric pulmonary imaging[12,13].

Two major challenges should be addressed to use MRI for lung imaging[14]. One is the low SNR of the ^{1}H lung MRI. Due to low proton density of the lung parenchyma, the signal intensity in the lung is expected lower than in other organs. In addition, the large susceptibility difference between the air and lung tissue results in very short T2*, which would further reduce the parenchymal signal. The other is subject motion. To achieve high resolution structural image, MRI requires a much longer scan time, usually a few minutes or even longer, which could be completed in a few seconds with CT. Under that situation, lung MRI scan needs to consider subject motion, such as respiratory motion, cardiac motion, and bulk motion etc.

This dissertation will focus on developing novel techniques to improve ^{1}H lung MRI. First of all, a high scan efficiency image acquisition and reconstruction strategy, called

iMoCo-UTE[15], is proposed to achieve high SNR motion corrected 3D lung image volume. Then, the technique is extended from 3D to 4D, reconstructing 3D respiratory motion resolved lung images and the contrast dynamics of 3D dynamic contrast-enhanced (DCE) MRI acquisition.

Further, I propose a 5-min free-breathing lung MRI strategy for pediatric and neonatal studies, by using the proposed techniques as well as optimizing the clinical setups.

However, the free breathing scan still needs a few minutes even with the optimized acquisitions and reconstructions. In the end, I propose a fast UTE acquisition scheme to fit a 3D UTE acquisition within single breath-hold, which can achieve moderate resolution but high image quality lung volume in 15 seconds.

1.1. Outline

Chapter 2 provides the background knowledge for this dissertation, covering basic MR physics, MR sequence, and signal equation. At the end of the chapter, the generalized MRI reconstruction framework, as well as compressed sensing MRI technique are introduced that pertain to the rest of the dissertation.

Chapters 3 to 6 describe the technical innovations as well as clinical translational research related to ^{1}H lung MRI.

In Chapter 3, I proposed a high scanning efficiency, motion corrected imaging strategy for free-breathing pulmonary MRI by combining a motion compensation reconstruction with a UTE acquisition, called iMoCo UTE. The proposed strategy showed improvements in the free breathing lung MRI scans, especially in very challenging application situations, such as pediatric and neonatal studies.

In Chapter 4, I extended the iMoCo reconstruction from 3D to 4D reconstruction, by adding a low-rank constraint in the reconstruction framework, named Motion Compensated Low-Rank (MoCoLoR) reconstruction. The proposed method was applied to both 3D motion resolved lung MRI and 3D DCE MRI, and showed improvements in the final reconstruction.

In Chapter 5, I proposed an optimized 5-minute non-sedated neonatal and pediatric pulmonary UTE strategy. Multiple technical improvements were implemented including the novel acquisition and reconstruction proposed in Chapter 3, customized hardware design for pediatric patients, and scan parameters optimization. The lung MR images acquired with the proposed strategy were able to capture different abnormalities, suggesting the feasibility of MRI for regular clinical pediatric lung imaging in the future.

In Chapter 6, a novel acquisition scheme for UTE with a reduced spoiling gradient was proposed for shortening the free breathing scans as well as improving breath-holding scans. The proposed scheme was validated on both phantom and volunteers, and the results showed the proposed scheme with a reduced spoiler gradient could achieve comparable image quality but saving up to 40% scan time for free breathing scan and get better image quality compared to standard UTE for breath-holding scan.

In the final chapter, I summarize the work presented in the previous chapters and also outline some future research directions related to this dissertation.

Chapter 2 MR Physics, Imaging and Reconstruction

Magnetic resonance (MR), also known as nuclear magnetic resonance (NMR), is a phenomenon that certain nucleus absorbs and re-emits electromagnetic radiation, was first observed by Isidor Isaac Rabi in 1938. In late 1970s, physicists Peter Mansfield and Paul Lauterbur first created images of organs and soft tissues by introducing gradient magnetic fields to NMR, and they named the technique magnetic resonance imaging (MRI)[16]. Modern physics usually describes NMR via quantum mechanics approach, however, in the scope of MRI, it is easier to understand by describing MRI from the classical physics point of view[17]. This chapter would firstly introduce the basic concepts in MRI, including resonance, spin relaxation, and spatial encoding. Then, one specific MRI sequence called ultra-short echo time (UTE), and generalized reconstruction framework are introduced for understanding MR acquisition and reconstruction methods described in the following chapters.

2.1. Magnetic Resonance Physics

2.1.1. Magnetization and Free Precession

Certain atomic nuclei, such as ^{1}H, ^{13}C, possess an intrinsic angular momentum. And the amount of angular momentum is called spin. In the context of MRI, a group of spins are usually considered as a whole system, and a macroscopic magnetization is used to represent the amount of angular momentums contributed from all the spins in the

system. Without an external magnetic field, spins have a randomly distributed angular momentums, resulting in a zero bulk magnetization, as shown in **Figure 2.1 (a)**. When an external magnetic field is applied to the spins system, the spins would no longer distribute randomly, in **Figure 2.1 (b)**.

(a)   (b)
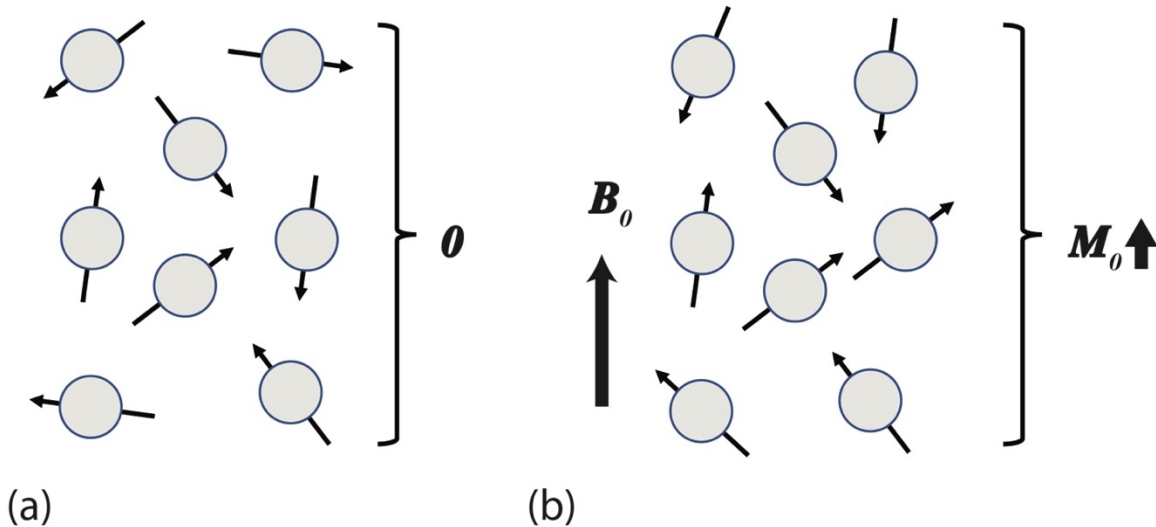
Figure 2.1 Spins behavior in external magnetic field. Without external magnetic field, spins are randomly distributed, and the observed bulk magnetization is 0, as shown in (a). By adding an external magnetic field, spins tend to align with the direction of the external field, formulating a non-zero net magnetization parallel to the external field, as shown in (b).

From the classical physics point of view, the spins would tend to align with the direction of the applied field to reduce the energy of the system. It turns out the system would generate a small non-zero magnetization, and magnetization is given by:

$$\boldsymbol{M}_0 = \frac{N_p (\gamma/2\pi)^2 h^2 B_0}{4kT_s} \boldsymbol{e}_z$$
(2-1)

Here, $\boldsymbol{M}_0$ represents the bulk magnetization induced by the external field. N_p are the population of spins, T_s is temperature. $\gamma/2\pi$, h, and k are gyromagnetic ratio, Planck's constant, and Boltzmann's constant. B_0 is the magnitude of the external field, and $\boldsymbol{e}_z$ is

the direction of the field. According to the equation, bulk magnetization is proportional to the strength of the external field.

The spins would resonate at a certain frequency ω_0 in the static $\boldsymbol{B}_0$ field, called Larmor frequency. And Larmor frequency is given by:

$$\omega_0 = \gamma B_0 \tag{2-2}$$

When another external oscillating magnetic field named $\boldsymbol{B}_1(t)$, with the appropriate Larmor frequency, is applied to the spins system, the bulk magnetization would be tilted to the transverse plane. Because the Larmor frequency is typically in the range of radiofrequency, this process is termed radiofrequency (RF) excitation, similarly, $\boldsymbol{B}_1(t)$ is also called RF pulse. When the magnetization, noted as $\boldsymbol{M}'$, is tipped away from $\boldsymbol{e}_z$ direction, the magnetization would precess about $\boldsymbol{e}_z$ with ω_0. Meanwhile, a RF signal is re-emitted from the spins system, which could be captured by NMR or MRI receiver coil as the NMR signal. And the signal intensity is proportional to the projection of magnetization in the transverse plane, which is perpendicular to $\boldsymbol{e}_z$. The acquired NMR signal is usually represented by a complex value or a 2D vector.

2.1.2. Relaxation

When $\boldsymbol{M}'$ precesses about the $\boldsymbol{e}_z$ axis, it would experience relaxation process to return to the equilibrium state $\boldsymbol{M}_0$. Two different relaxations, T1 relaxation and T2 relaxation, are involved, and they could be characterized by two relaxation time, T_1, and T_2. To help explain the relaxation process, $\boldsymbol{M}'$ could be decomposed to $[M_x, M_y, M_z]$, illustrated in **Figure 2.2 (a)**.
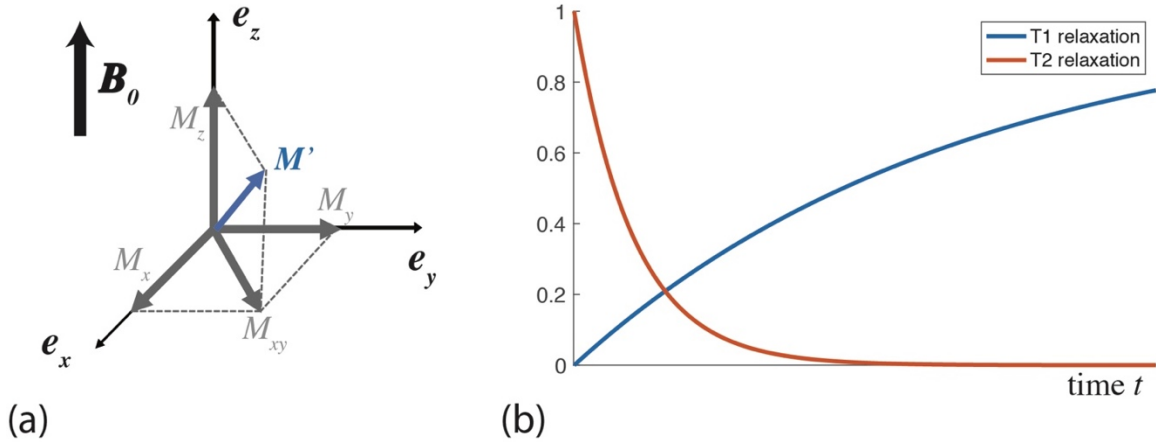
Figure 2.2 Description of magnetization decomposition and T1, T2 relaxation. Magnetization could be decomposed to longitudinal component M_z, which experiences T1 relaxation, and transverse components M_x and M_y, that experience T2 relaxation. T1 and T2 relaxation over time are compared in (b).

The T1 relaxation is also called the longitudinal relaxation, describes the longitudinal magnetization M_z returns to the equilibrium state. The T2 relaxation is also called the transverse relaxation, describes the transverse magnetizations $[M_x, M_y]$ decay or dephase. T1 and T2 relaxations follow the equations below:

$$\frac{dM_z}{dt} = -\frac{M_z - M_0}{T_1} \tag{2-3}$$

$$\frac{dM_{xy}}{dt} = -\frac{M_{xy}}{T_2} \tag{2-4}$$

Here, T_1 and T_2 are the relaxation times describing the two relaxation processes respectively. And there are closed-form solutions for equations (2-3) and (2-4),

$$M_z(t) = M_0 + [M_z(0) - M_0]e^{-\frac{t}{T_1}} \tag{2-5}$$

$$M_{xy}(t) = M_{xy}(0)e^{-\frac{t}{T_2}} \tag{2-6}$$

Figure 2.2 (b) shows the T1 and T2 relaxations start with the initial state, $M_z(0) = 0$. Different biological tissues might have different sets of T_1 and T_2. Therefore, T_1 and T_2 could provide different MR image contrasts to characterize tissue properties.

2.1.3. Spatial Encoding and K-space

According to Equation (2-2), the magnetization precesses at the same frequency in the same strength static field, all the spins have the same phase in transverse plane, shown in **Figure 2.3 (a)** .
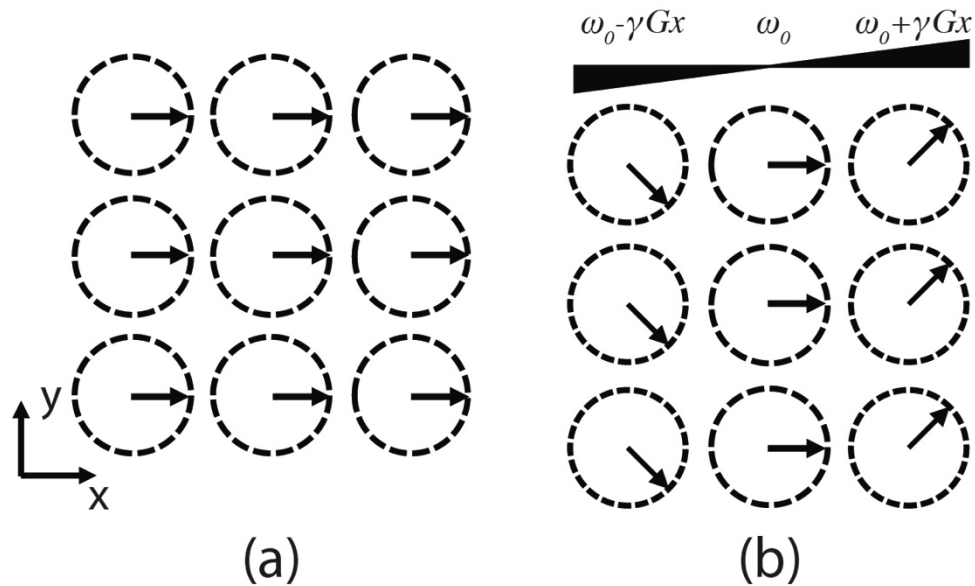
Figure 2.3 Effect of gradient magnetic field on transverse magnetizations. Without gradient magnetic field (a), transverse magnetizations from different locations share the same phase. When an extra gradient magnetic field is applied in the x direction, transverse magnetizations with different x locations would have different phases due to different precession frequencies.

If the external field is no longer spatially homogeneous, magnetizations in different locations could precess at different frequencies. Assuming a small linear magnetic field, named gradient field G, is added on top of the strong B_0 field, shown in **Figure 2.3 (b)**, precession frequencies at different locations are given by:

$$\omega = \gamma(B_0 + Gx) \tag{2-7}$$

When a 3D gradient field is applied, it could be extended accordingly to:

$$\omega = \gamma(B_0 + \boldsymbol{G} \cdot \boldsymbol{r}) \tag{2-8}$$

Here, the inner product of gradient vector G and location vector r is used to replace the scalar multiplication. By manipulating the gradient field, including changing gradient direction and strength, spins in different locations would be differentiated based on their phases, which results in the spatial encoding in MRI. Then the total received signal with spatial encoding could be represented by the integral of all the transverse magnetizations within the volume.

$$s(t) \propto \iiint M_{xy}(x,y,z)e^{-i\omega_0 t}e^{-i\gamma \int_0^t G(\tau)\cdot r d\tau} \, dxdydz \qquad (2\text{-}9)$$

Here, $r = [x,y,z]^T$ represents the 3D location. $M_{xy} = M_x + iM_y$, is the complex-valued NMR signal. Because all the spins share the same default phase term $e^{-i\omega_0 t}$, we can move this term out of the integral, and even remove this term. In addition, a new variable $k(t) = \frac{\gamma}{2\pi}\int_0^t G(\tau)d\tau$ is introduced. Then, the signal equation could be simplified as below:

$$s'(t) = s(t)e^{i\omega_0 t} \propto \iiint M_{xy}(x,y,z)e^{-i2\pi k(t)\cdot r} \, dxdydz \qquad (2\text{-}10)$$

The integral term is a 3D continuous Fourier transform of the image volume. Further, because k is a function about t, signal without the constant phase term could be rewritten as a function of k,

$$s'(k) \propto FT[M_{xy}(r)] \qquad (2\text{-}11)$$

Signal could be considered as the spatial frequency domain, always called "k-space" in MRI. To image a volume, different gradient pulses are designed to fully sample the whole k-space, then the images of the volume could be reconstructed from the full k-space via inverse Fourier transform. k-space is one of the most important concepts in MRI, because it connects the signal acquisition and image formulation. In the next a few

chapters, it would be mentioned in both the sequence design and the image reconstruction.

2.2. MRI Sequence and Short T2* Components Imaging

2.2.1. Gradient Echo Acquisition and Spoiling

Pulse sequence is another core concept in MRI, which consists of a number of RF pulses and gradients to sample the k-space. In addition, by changing the shapes and magnitudes of the RF and gradient pulses and the timings of them, different contrasts images would be generated.

One major category of the MRI sequences are called gradient-recalled echo (GRE) sequences. The basic unit of a GRE sequence, as plotted in **Figure 2.4 (a)**, consists of a RF excitation pulse, and different spatial encoding gradient pulses. The duration of the basic unit is called repetition time (TR). For convenience, TR is also used to represent the basic unit in the sequence.
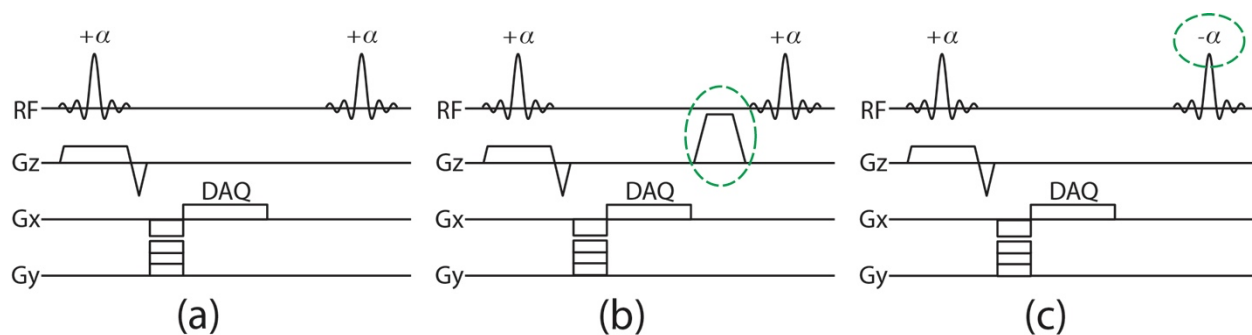
Figure 2.4 Illustration of GRE sequences. (a) shows the basic GRE sequence, which includes RF excitation, phase encoding and frequency encoding(DAQ) gradients. (b) and (c) respectively illustrate two different spoiling strategies, gradient spoiling and RF spoiling in the GRE sequence, modifications on basic GRE sequence are highlighted.

To avoid the transverse magnetization coherence interference from previous excitations, TR of basic GRE sequence needs to be long enough, which allows transverse magnetization decay to nearly zero through T2 relaxation. An alternative is to disrupt the transverse magnetizations before the next excitation, named spoiling strategies[18,19]. The spoiling strategies ensure that the steady-state magnetization has effectively no transverse magnetization before the next excitation even without a long TR. The GRE sequence with spoiling strategies are also called fast or rapid GRE.

Two types of spoiling strategies are introduced here. One is gradient spoiling, an additional gradient with certain amplitude and direction is added before the next excitation to suppress the transverse magnetization, as shown in Figure 4 (b). The other is RF spoiling, the phase of the RF pulse is changed from TR to TR, which leads to the transverse magnetizations from previous TRs with different phases cancelling each other out, as shown in Figure 4 (c).

2.2.2. Ultra-short Echo Time (UTE) Acquisition

As mentioned in the previous section, magnetization would experience a T2 relaxation decay after the RF excitation, and the decay rate is characterized by T_2, according to Equation (2-6). However, a faster signal decay rate would be observed in the GRE sequence, because the local field inhomogeneity would lead to local transverse magnetization dephasing, which leads to a faster signal decay on a macroscopic scale. A new relaxation time constant T_2^*, shorter than T_2, is defined to describe the decay rate of GRE sequence. The echo time (TE) represents the time from the center of the RF-

pulse to the center of the echo, with T_2^* together could be incorporated in the signal

equation, reflecting the signal decay during the acquisition.

$$s'(\mathbf{k}) \propto FT[M_{xy}(\mathbf{r})e^{-\frac{TE}{T2^*}}] \tag{2-12}$$

Usually, the TE of GRE sequence is around or longer than 1ms, because of the slice

selection rephasing and phase encoding gradients, as shown in **Figure 2.5**. When

imaging very short T_2, or T_2^* components with GRE sequence, the signal would

dramatically decay, especially for $T_2^* \ll TE$.

Ultra-short echo time (UTE) sequence is one of the variants of the GRE sequence.

UTE sequence can push the TE close to zero by modifying the standard GRE

sequence. **Figure 2.5** shows some differences between UTE and standard GRE

sequences. Firstly, the selective excitation is replaced by a non-selective hard pulse

without rephasing gradient. Secondly, instead of having phase encoding gradients, the

UTE sequence starts frequency encoding and data acquisition immediately at the end of

RF excitation. By definition, the echo happens right at the end of the RF excitation,

creating an ultra-short TE, usually at the sub-millisecond level.

Components with different T_2^*s acquired by two sequences are illustrated in the right

column of **Figure 2.5**. When imaging very short T_2^* components, such as 0.1 or 0.5ms,

with standard GRE sequence, the signals have already decayed to close to 0 at TE_1, in

contrast, with UTE sequence, the signals are preserved at TE_2.
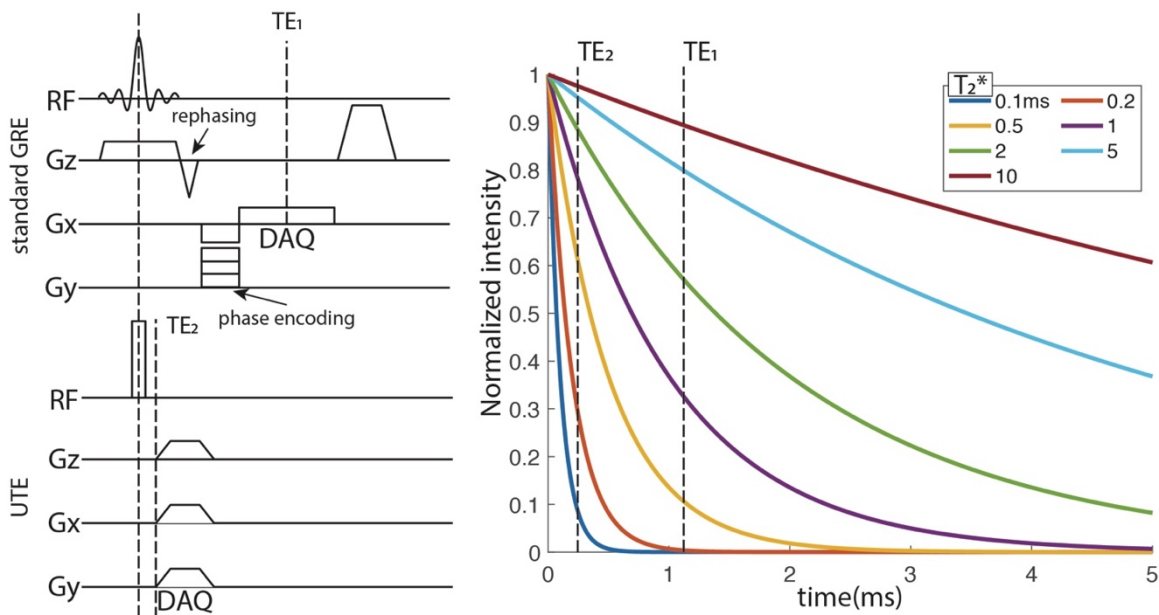
Figure 2.5 Ultra-short echo time(UTE) sequence for short T_2* imaging. Left column shows comparison of standard GRE and UTE sequences. Right column shows signal evolution of different T_2^* components and the UTE sequence can preserve the signals from short T_2^* components.

2.2.3. UTE Trajectory

Because the UTE sequence often uses a non-selective hard pulse for RF excitation, UTE sequences are usually designed as a 3D acquisition. To image the 3D volume, a 3D k-space sampling strategy is needed. In addition, because UTE sequence starts acquisition as soon as the end of excitation, k-space sampling in each TR always start from the center or the zero frequency point.

To fully cover the 3D k-space, two typical acquisition patterns or trajectories are used, 3D radial[20,21] or 3D conical[22,23] trajectory, as plotted in Figure 6.
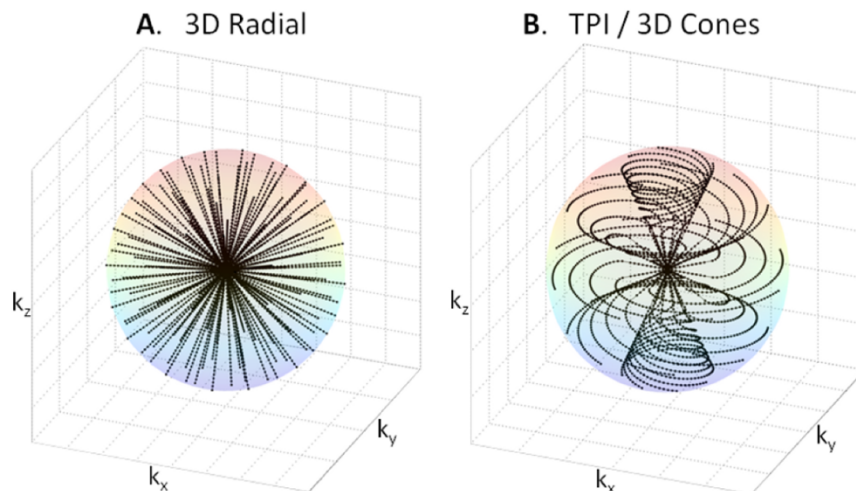
Figure 2.6 3D UTE trajectory examples. Left shows the center-out radial trajectory acquisition, right shows the conical trajectory acquisition. [Adapted from Madelin, Guillaume 2012.[24]]

2.3. MRI Reconstruction

2.3.1. MRI Signal Equation

Once the k-space data are acquired, the final step is to reconstruct the image from the data. According to Equation (2-11), images could be reconstructed by applying the inverse Fourier transform on the k-space as long as the k-space is fully sampled. However, more components in the reconstruction need to be considered in practice.

Firstly, noise always exists in the acquired data. In MRI, the acquisition noise is modeled as a complex-valued additive white Gaussian noise (AWGN)[25]. Then the signal equation could be rewritten as:

$$\widehat{s'}(t) = \iiint M_{xy}(x, y, z)e^{-i2\pi k(t)\cdot r}\, dxdydz + n(t) \qquad (2\text{-}13)$$

Here, $\widehat{s'}(t)$ represents the acquired data, and $n(t)$ is the complex AWGN acquisition noise. The continuous signal equation should be discretized before the reconstruction. t would be discretized as the index of the time point, at each time point, one point in the k-space is sampled. After the signal discretization, the Fourier transform could be replaced by the discrete Fourier transform (DFT), represented by linear operator F.

Secondly, the acquisition pattern $k(t)$, could be also formulated as a linear operator $P(t)$ representing sampling in the k-space.

$$\widehat{s'}(k(t)) = P(t)FI + n(t) \qquad (2\text{-}14)$$

Thirdly, a multi-coil acquisition mode, which is widely used in modern MRI, should be considered. The spatially localized coils would have different coil sensitivity maps, which can be also modeled as a linear operator and because signals are acquired by each coil independently, the noise term should also extend to include a coil dimension.

$$\widehat{s}_j'(\boldsymbol{k}(t)) = P(t)FS_jI + n_j(t) \tag{2-15}$$

One assumption made on the multi-coil acquisition mode is that the noise at different time points as well as different coils are independent and identically distributed (i.i.d). However, sometimes noise of different coils are with varied amplitudes and correlated with each other, then the i.i.d assumption does not hold. To preserve the assumption, a noise pre-whitening step is always required before the reconstruction step[26].

Figure 2.7 summarizes the signal equation (2-15), including components we mentioned above. The next step is to reconstruct the image based on the signal equation.
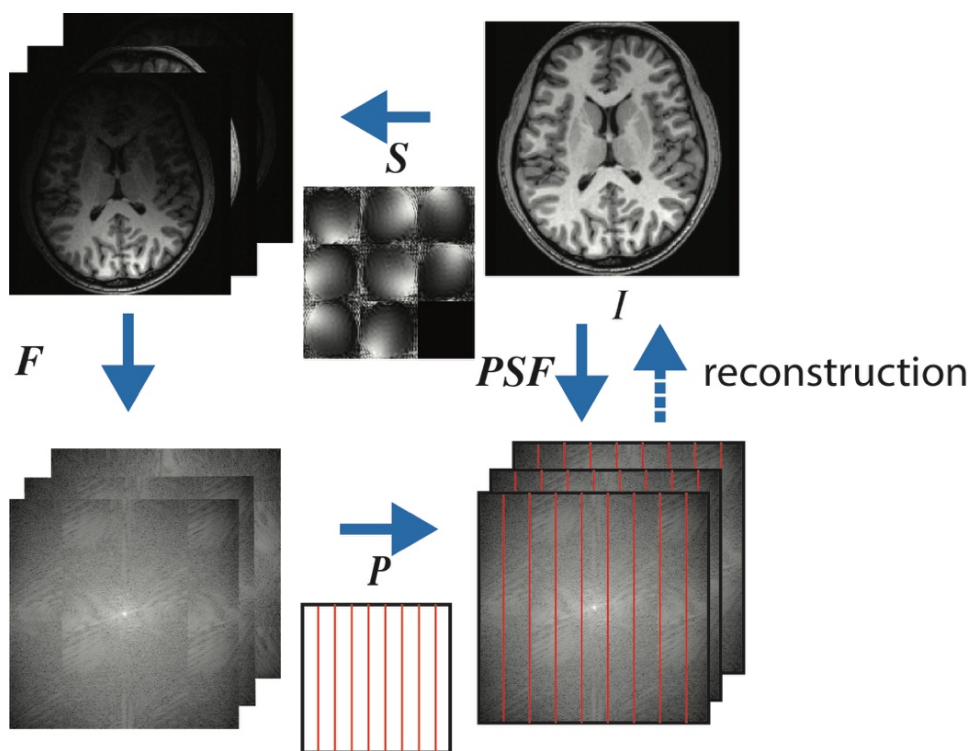
Figure 2.7 Illustration of the MRI signal equation. The image would multiply with different sensitivity maps to represent multi-channel MRI acquisition. Then multi-channel images are transformed to k-space via discrete Fourier transform (DFT). Sampling k-space data could be modeled as applying a binary mask on the k-space. All the operations above could be formulated as linear operators.

2.3.2. Generalized MRI Reconstruction Framework

Once the discrete signal equation (2-15) is established, the reconstruction step could be formulated as a least-square optimization problem:

$$\underset{I}{\arg\min} \sum_j^N \left\|PFS_jI - d_j\right\|_2^2 \tag{2-16}$$

Here, d_j replaces the acquired data $\widehat{s}_j^j(\boldsymbol{k}(t))$ in Equation (2-15). The problem can be easily fit in different trajectory designs and different coil setups. And the problem is a linear least squares problem, which can be solved by standard iterative methods such as conjugate gradient descent algorithm[27]. Because most of the MRI reconstruction problems can be formulated and solved by following the above framework, the framework is called generalized MRI reconstruction framework.

Especially, when the framework utilizes multi-channel coils and certain k-space undersampling schemes to accelerate the MRI acquisition, it is also known as parallel imaging (PI) technique.

2.3.3. Compressed Sensing MRI

Compressed sensing (CS) MRI is also developed for MRI acquisition acceleration[28]. CS MRI includes a few components. Firstly, a random or pseudo-random sampling scheme is required. Then, a sparsifying transform, such as wavelet transform, which can use a sparse representation to represent the signals from the original domain, is required. Finally, a constrained reconstruction problem is formulated and solved by an iterative algorithm.

CS MRI can also be incorporated in the generalized reconstruction framework as below.

$$\underset{I}{\operatorname{argmin}} \sum_{j}^{N} \left|\left| PFS_j I - d_j \right|\right|_2^2 + \lambda_s \left|\left| \Phi(I) \right|\right|_1 \tag{2-17}$$

Compared to the (2-16), another l1-norm term with a sparsifying transform, Φ, is added into the framework. And λ_s is a regularization term.

2.3.4. Beyond Theoretical MRI

By now, most of the basic MRI concepts related to this dissertation have been introduced. However, in the real world, problems are much more complicated than what the basic MRI theory can describe. For instance, subject motion is one of the most challenging problems in MRI, especially in body MRI. Lots of strategies from different aspects are proposed to solve the problem. From the reconstruction aspect, fast 3D acquisition strategies with parallel imaging and compressed sensing are proposed. From the acquisition aspect, non-Cartesian acquisition strategies, which are robust to motion, are proposed. From the hardware aspect, external devices, such as an ultrasound system or MRI compatible camera, are designed to monitor and correct subject motion. In the rest of this dissertation, I would focus on how to deal with the practical problems related to ^{1}H lung MRI.

Chapter 3 Iterative Motion Compensation Reconstruction Ultra-short TE (iMoCo UTE) for High Resolution Free Breathing Pulmonary MRI

3.1. Introduction

MRI has the potential to assess pulmonary diseases by providing soft-tissue contrast and structural information within the lung[29]. Unlike X-ray CT, MRI avoids ionizing radiation exposure, which would be safer for pediatric subjects[30], or patients requiring longitudinal follow-up imaging[31]. However, pulmonary MRI is challenging due to short T2*, low proton density of the lung parenchyma[32,33] and subject motion, especially respiratory motion[34].

UTE and zero echo time (ZTE)[35] type acquisition strategies have been developed to preserve short T2* signal in the lung by providing the means to collect images with a sub-millisecond echo time (TE). Such sequences use optimized excitation pulses and readouts strategies to maximize SNR for pulmonary imaging[36]; however, most UTE/ZTE sequences still take a few minutes or longer, usually 5 to 10 minutes[33,37,38], required to obtain sufficient lung parenchyma SNR with high spatial resolution. During the scan, there are inevitable motion effects, especially from respiratory motion. In addition, longer scan time increases the possibility of irregular motion of the subject, especially for pediatric subjects[39] and subjects with poor pulmonary function.

A variety of respiratory motion compensation strategies have been developed, most of which utilize motion tracking for retrospective motion correction or compensation.

External respiratory belts are widely used to indirectly track the motion by measuring the respiratory-induced abdomen stretching. An alternative way is to use the repeatedly acquired k-space center (DC), which is feasible for center-out UTE sequences, measuring the signal change caused by respiratory motion[38,40–42]. To more accurately and directly characterize subject motion, low spatial but high temporal resolution 2D/3D images could be reconstructed and used as a self-navigator [34,43–45].

Most of the motion correction and compensation methods can be classified into three categories. 1) Respiratory gating: based on the respiratory motion signal, only data acquired within a certain motion state, usually the end expiratory state, is used for reconstruction[46] . However, gating based methods reduce scan efficiency and prolong the scan time. To increase the scan efficiency, the soft-gating method was proposed to add non-zero weightings on the data[34,47,48], but it reduces the ability to correct motion[37]; 2) Motion resolved reconstruction: instead of reconstructing a single motion gated image, all acquired data are grouped in different motion states, and spatial correlation of the different images are used as the prior information for compressed sensing based reconstruction, such as XD Golden-angle RAdial Sparse Parallel reconstruction (XD-GRASP)[49,50], kt- FOCal Underdetermined System Solve (kt-FOCUSS)[51]; 3) Motion compensation (MoCo) reconstruction with image registration: Unlike gating or soft-gating strategies, motion compensation strategies align all motion states images to the same state via image based registration. After registration, all motion states images are summed to compose a single image, therefore increasing the data acquisition efficiency[52]. MoCo type strategies have been applied in simultaneous PET/MR applications for increase PET image SNR[53–57]. A more sophisticated way that

Batchelor[58] first proposed is the generalized matrix description (GMD), to formulate the motion deformation as a matrix operator to describe the motion propagation in signal space. A few motion compensation reconstruction strategies[59–63] based on GMD have been proposed and applied to cardiac MRI.

In this chapter, I propose a new free breathing motion corrected pulmonary MRI strategy, iterative Motion Compensation reconstruction ultra-short TE, called iMoCo UTE, to improve high spatial resolution free breathing lung MRI. There are three main components of the proposed method: 1) a pseudo random non-Cartesian UTE sequence, 2) motion resolved reconstruction and motion estimation, and 3) a novel iterative motion compensation (iMoCo) reconstruction with compressed sensing. The iMoCo reconstruction iteratively fits the data to a non-rigid motion model, and leverages compressed sensing principles to further suppress noise and artifacts. When combined with a UTE sequence, the proposed method addresses the challenges in lung MRI of intrinsically low SNR and motion by providing a high acquisition efficiency and motion robust pulmonary MR images, especially in challenging situations, such as pediatric MRI studies. The proposed strategy is evaluated on both healthy volunteers and pediatric patients, and compared to other motion correction strategies, such as soft-gating, motion resolved reconstruction, and image based motion compensation (MoCo) strategies.

3.2. Methods

3.2.1. Overview of iMoCo UTE

The overall workflow of proposed iMoCo UTE is summarized in **Figure 3.1**.
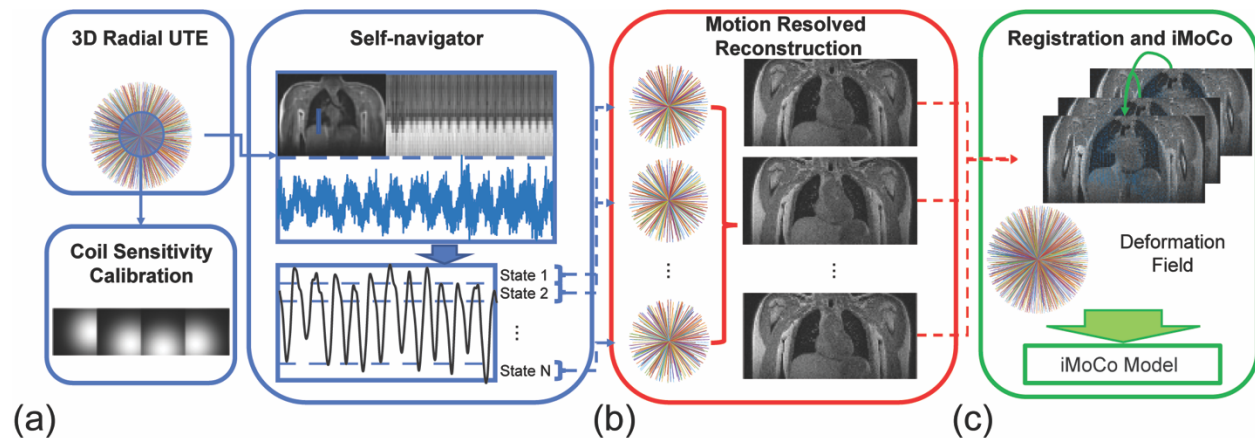
Figure 3.1 Overview of the iMoCo UTE workflow. (a) After optimized 3D radial UTE data are acquired, the center k-space is cropped out for coil sensitivity calibration, then used to estimate the respiratory motion signal via the k0 signal or a reconstructed 3D image navigator. (b) Based on the self-navigator signal, data are grouped in different motion states, then motion resolved images with medium spatial resolution are reconstructed. (c) All motion states images are registered to the selected reference state image via non-rigid image registration, then the deformation fields and the whole dataset are fed in the iterative motion compensation reconstruction model.

Data are acquired with a pseudo randomly sampled 3D radial UTE sequence which results in k-space sample ordering being uncorrelated with the respiratory motion. Then, data are binned to different motion states according to respiratory tracking signals. Respiratory tracking is first determined using a k0/DC navigator signal. Then, additional image based navigator is used to remove the data with irregular motion (**Figure 3.1** (a)). Instead of doing high spatial resolution motion resolved reconstruction, the motion resolved data is used first to reconstruct ~1.5 times coarser spatial resolution motion resolved images (**Figure 3.1** (b)). Motion fields from different motion states to a reference state then are estimated via non-rigid registration[64] (**Figure 3.1** (c)). Finally,

the estimated motion fields and a spatial total generalized variation (TGV) sparsity constraint[65] are added into the iterative motion compensated reconstruction (iMoCo) model to reconstruct a single state high resolution motion-free image.

3.2.2. UTE Sequence

An optimized 3D UTE sequence with slab selection and variable density readout acquisition[36], which increases the SNR efficiency and reduces aliasing artifacts, was used for pulmonary imaging scans. A golden angle ordering acquisition scheme was used to randomize undersampling artifacts over time and improve the motion resolved reconstruction and motion estimation. All the studies were performed on 3T MRI clinical scanners (GE Healthcare, Waukesha, WI, USA). More specific acquisition parameters are listed in the experiment section.

3.2.3. Respiratory Motion Detection and Motion Resolved Reconstruction

A DC based self-navigator was used for initial respiratory motion detection, in which the first points of the radial readouts are used as self-navigator signals. The multi-channel data were combined via the adaptive navigator strategy[66]. Then DC signals were filtered by low-pass (0.5~1 Hz cut-off frequency) filter to reduce high frequency noise. The DC navigator was used as long as no large fluctuation of the DC signal (defined as having a signal deviation from base line that was 3 times greater than range of the respiratory signal) was observed. If there was a baseline fluctuation of the DC signal, alternatively,

a 3D image based navigator, generated by a locally low rank constrained

reconstruction[34], was used to identify and discard bulk motion corrupted data. The

respiratory motion signal was derived from the DC signal after discarding the irregular

motion corrupted data and baseline correction. (The 3D image navigator was not used

for respiratory motion estimation due to limitations on the spatial (~3mm isotropic) and

temporal resolution (~300ms) that were not sufficient to capture pediatric respiratory

motion.)

Based on the motion estimates, the acquired data was binned into different

respiratory motion states for motion resolved reconstruction, a process similar to XD-

GRASP[49]. Even when data are binned into different motion states, there is inevitable

residual motion among data within the same motion state. To minimize this effect, a

large number of motion states, between 8 and 10, was used. This is in contrast to

standard XD-GRASP, which typically uses 4 to 6 motion states[50]. However, since the

full dataset (all spokes) are usually 3 to 4-fold undersampled, if number of motion states

increases to 8 or higher, the undersampling factor would go up to 30, which would lead

to strong streaking artifacts and lower SNR even with compressed sensing and parallel

imaging. To accommodate the higher undersampling and to reduce the reconstruction

artifacts, a coarser resolution (~1.5 times the native resolution) was used, which

maintains a reasonable undersampling factor in this workflow. Since the purpose of the

binning is for estimating motion between the bins and correct for it, a full resolution

reconstruction is not necessary. Reducing the resolution has the added benefit of

reducing the computational load. The reconstruction was done via an XD-GRASP type

reconstruction solving,

$$\underset{X}{\text{argmin}} \sum_{i,k}^{N,m} \left|\left|W(FS_i X_k - d_{ik})\right|\right|_2^2 + \lambda_s \left|\left|\Phi X\right|\right|_1 + \lambda_t TV_t(X) \qquad (3\text{-}1)$$

Here, the squared-error data consistency term (left) includes multi-channel sensitivity

maps $S_i (i = 1,2, \dots N)$, motion states sorted multi-channel data d_{ik}, W is sampling

density compensation weights, F is the non-uniform Fourier transform operator,

implemented via gridding algorithm, and X_k are the motion-state 3D images,

parametrized by motion state index k. A spatial sparsity 3D l1-wavelet term, where Φ is

the wavelet transform, and a motion dimension total variation term, $TV_t()$, are added to

the reconstruction.

Following the motion resolved reconstruction, one of the motion states (e.g. typically the

end expiratory state) was selected as a reference frame. All other motion state images

were then registered to the reference via Demons non-rigid registration[64] (4 pyramid

levels coarse-to-fine registration and 100 iterations are used in Demons). Estimated

motion fields were interpolated to match the full resolution image, and used in the

following motion compensation reconstruction.

3.2.4. Iterative Motion Compensated (iMoCo) Reconstruction

Once the motion fields were derived, the entire data is used to reconstruct a single

frame, that is motion corrected. We leverage the relation that $M_k \hat{X} = X_k$, where $M_k (k =$

$1,2 \dots m)$ are derived motion fields, $\hat{X}$ is the final reconstructed image, to include our

motion estimates in the forward model. As described in the GMD model, the motion field

can be formulated as a linear operator. Although the inverse operator of non-rigid

deformation is difficult to calculate, the adjoint operator can be simply estimated as

reverse deformation from the reference to a certain state image. To further reduce streaking artifacts caused by undersampling and residual motion, a spatial total generalized variation (TGV) sparsity regularization term is added to the model. Unlike TV regularization, TGV relaxes the assumption that image is piecewise constant, which would be more suitable for continuous signal changes of tissues[65]. So the reconstruction problem can be reformulated as optimization problem:

$$\underset{\hat{X}}{\arg\min} \sum_{i,k}^{N,m} \left\| W\left(FS_i M_k \hat{X} - d_{ik}\right) \right\|_2^2 + \lambda_s \text{TGV}_s\left(\hat{X}\right) \tag{3-2}$$

In the data consistency term (left), I, d_{ik}, and F are the same notations as the motion resolved reconstruction (Eq. 1) with the addition of derived motion fields $M_k(k = 1,2 \ldots m)$. $\hat{X}$ is the final reconstructed, single state high resolution image. The sparse penalty term(right) is spatial TGV. The optimization problem is solved by using first order primal-dual algorithm[67].

3.2.5. Experiments

All human studies conducted were approved by UCSF Institutional Review Board (IRB). Several different types of studies are included in the results and discussions.

For adult healthy volunteer studies (N=7), scan parameters included: prescribed field of view(FOV) $= 32 \times 32 \times 32 \text{cm}^3$ ($64 \times 64 \times 64 \text{cm}^3$, 2-fold oversampling on readout direction for radial sequence), flip angle $= 4°$, 1.25mm or 1mm isotropic resolution, readout bandwidth $= \pm 125 kHz$, $TE = 70 \mu s$, $TR = 2.7 - 3.1 ms$, TR increased as the prescribed FOV was reduced. The total scan time was approximately 5 min to 5 min 30 s. Number of total acquired spokes of each scan was approximately 100,000.

For pediatric patients diagnosed with pulmonary diseases studies (N=4), the FOV was prescribed based on the size of the subject (22~26cm), and spatial resolution

(isotropic) was kept to 1.1mm or higher (<1mm) due to their smaller anatomical structure size. Both TE and TR ($TE = 80\sim110\mu s, TR = 3.1\sim3.7ms$) increased compared to adult studies due to smaller FOV and excitation slab. The number of spokes was adjusted between 80,000 to 90,000 to keep the total scan time no more than 5 min 30 s. Due to varied scan subject size, different receiver coil arrays were used in pediatric scans to improve SNR: 8-channel and 32-channel cardiac arrays (GE Healthcare, Waukesha, WI, USA), and a 12-channel flexible screen-printed coil array (Inkspace Inc., Moraga, CA, USA)[68].

For the infant patient study (N=1), the following scan parameters were used. FOV was 18cm, spatial resolution (isotropic) was 0.9 mm, $TE = 170\mu s, TR = 4.6ms$, the number of spokes was 75,000, and total scan time was around 5 min 30 s. 8-channel head coil (GE Healthcare, Waukesha, WI, USA) was used in the experiment due to very small subject size.

3.2.6. Data Processing and Imaging Reconstruction

The self-navigator, motion signal processing, and iMoCo reconstruction were implemented in MATLAB (Mathworks, Natick, MA). Coil sensitivity maps calibration, motion resolved reconstruction and soft-gating reconstructions were carried out by the Berkeley Advanced Reconstruction Toolbox (BART)[69]. All the quantitative measurements were also implemented in MATLAB.

3.2.7. Image Quality Comparison and Evaluation

For image quality comparisons, we implemented non-gating, soft-gating, motion resolved, and non-rigid motion compensation (MoCo) reconstruction and motion correction strategies following the details in previous works[34,47,50]. Briefly, the MoCo method used the motion resolved reconstruction from XD-GRASP to genereate images across motion states, which were then non-rigidly registered using Demons and then averaged together. Hyperparameters used were kept the same in all the reconstructions.

To quantitatively compare the image quality among different motion correction strategies, several image metrics were computed. The sharpness of the lung-liver interface or diaphragm was measured via the relative maximum derivative (MD), defined as the maximum intensity change between lung-liver interfaces divided by mean intensity in the liver.

Apparent signal-to-noise ratio (aSNR), defined as the average signal over a small region of interest (ROI) divided by standard deviation of area out of the subject, was measured. Three representative areas were selected as ROIs: an airway, lung parenchyma, and the aortic arch. Instead of SNR, aSNR was measured in this work because the reconstruction methods could introduce spatially varying noise and also perform inherent denoising. Images reconstructed with different strategies were spatially aligned, so ROIs at the same locations could be manually drawn on all the reconstructed images for measurement.

Contrast-to-noise ratio (CNR), defined as the contrast difference over noise level, was also computed. In lung MRI, it is valuable to distinguish air, lung parenchyma, and

vessels. Therefore, CNR between lung parenchyma and air, and between aortic arch and air were measured.

A paired sample t-test (p<0.05) method was used for statistical comparison of the quantitative measurements MD, aSNR, and CNR.

3.3. Results

3.3.1. Volunteer Studies Comparison

Volunteer study results are shown in Figure 3.2. One sagittal slice image from two adult volunteer studies with the proposed iMoCo and other motion correction strategies are shown in the first rows.

The overall image quality of both subjects with iMoCo method is better than motion resolved and soft-gating methods, due to higher data usage efficiency and a more accurate motion model. The zoomed-in images show that the proposed reconstruction has better lung parenchyma contrast and less residual motion compared to the soft-gating method, and sharper edges of airways and vessels compared to the MoCo method.
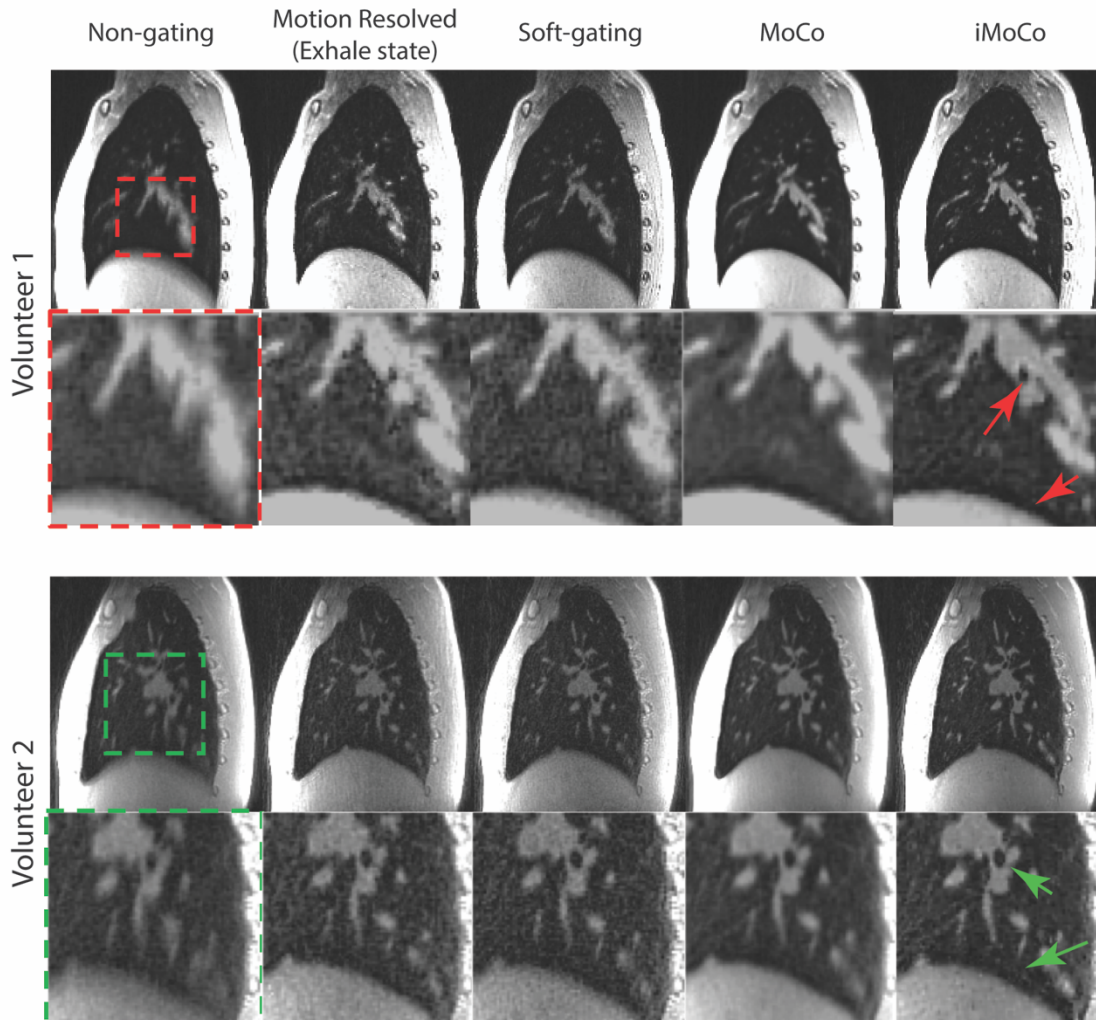
Figure 3.2 Example of volunteer study image results. The same slice images of each subject reconstructed with different motion correction and reconstruction strategies are plotted in the first rows, and a dashed square targeting at the center area of the lung are zoomed in and plotted in the second rows. In both cases, the iMoCo strategy had the sharpest image features and highest apparent SNR.

To compare the capability to visualize small vessels and airways in the lung, two higher spatial resolution(1mm isotropic resolution versus 1.25 mm isotropic resolution in Figure 3.2) examples are shown in Figure 3.3.
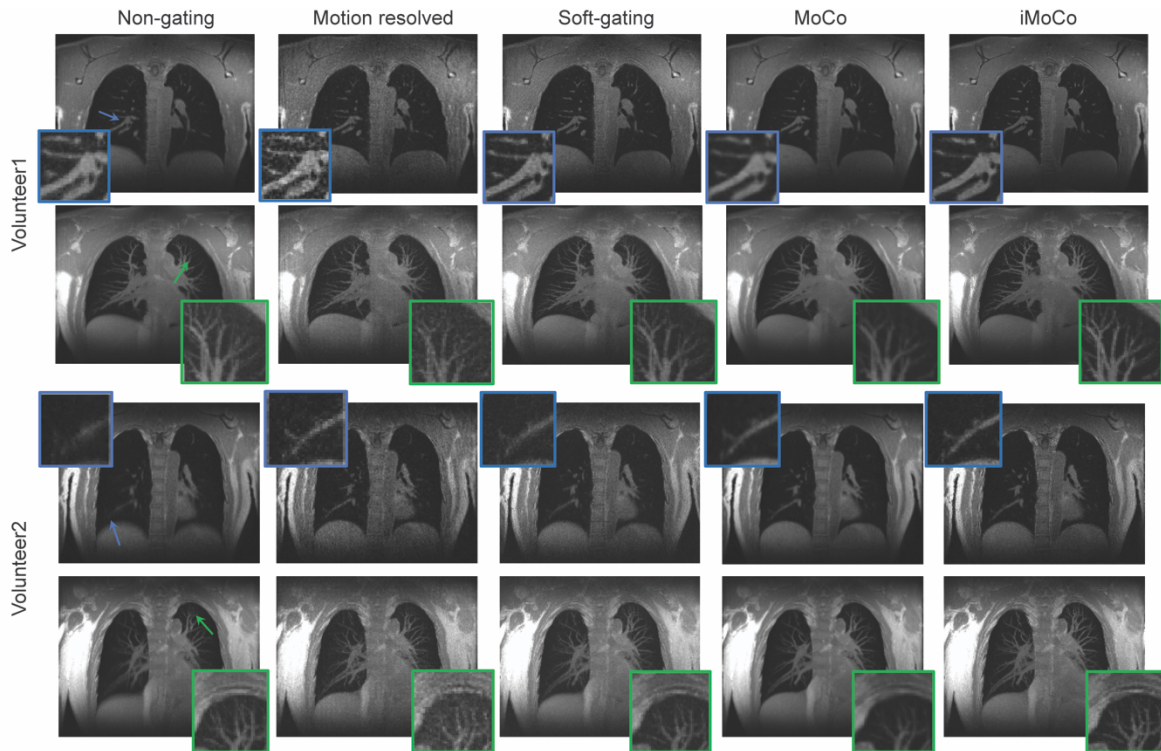
Figure 3.3 Example of high spatial resolution (1mm isotropic) lung images. The proposed iMoCo reconstruction is compared to non-gating, motion resolved reconstruction(exhale state), soft-gating and motion compensation(MoCo) reconstructions. In each volunteer example, the first row shows the one slice from different reconstructed images, and the second row shows the maximum intensity projection(MIP) of 30 slices in the AP direction. The area pointed with the arrows in the non-gating images are zoomed in. The iMoCo reconstruction was able to delineate the smallest pulmonary vessels.

One coronal slice from each study is shown in the first row, and a maximum intensity projection (MIP) of 30 slices centered at the first row coronal images positions are plotted in the second row. Images with the iMoCo reconstruction have the best visual image quality, and show lower noise level, sharper vascular structures and more small blood vessels compared to other methods.

3.3.2. Pediatric Patient Studies

Pediatric pulmonary MRI studies are much more challenging, especially for non-sedated free breathing scans. First of all, it is difficult for children to keep still during a long scan. Also, their respiration rates tend to be higher and less regular. In addition, the quiescent period after exhalation is much shorter, which might reduce the SNR efficiency and image quality of gating and soft-gating based methods[37]. Pediatric patients with different types of lung diseases and of different ages were scanned to show the capability of imaging different lung abnormalities with iMoCo UTE.

Results of 3 representative pediatric studies with different observed abnormal lung structures are shown in Figure 3.4. An image slice with the abnormality is shown in the first row, and a zoomed-in image in the second row. Images carried out by different reconstruction algorithms are compared for 3 patients: Patient 1 was a 5-year old female who had a severe combined immunodeficiency (SCID) post stem cell transplant with several observed lung nodules (red dashed circles); patient 2 was a 4-year old male with systemic juvenile idiopathic arthritis and childhood interstitial lung disease (chILD) with observed ground-glass opacity (green dashed circle, this opacity was also observed on CT); and patient 3 was a 8-year old female with surfactant protein C deficiency who had small pneumatoceles (lung cysts, blue arrow). Images with the iMoCo reconstruction had the best depiction of these pathologic features. Particularly in patient 3, the pneumatocele has a much sharper boundary and better contrast with iMoCo compared to other methods.
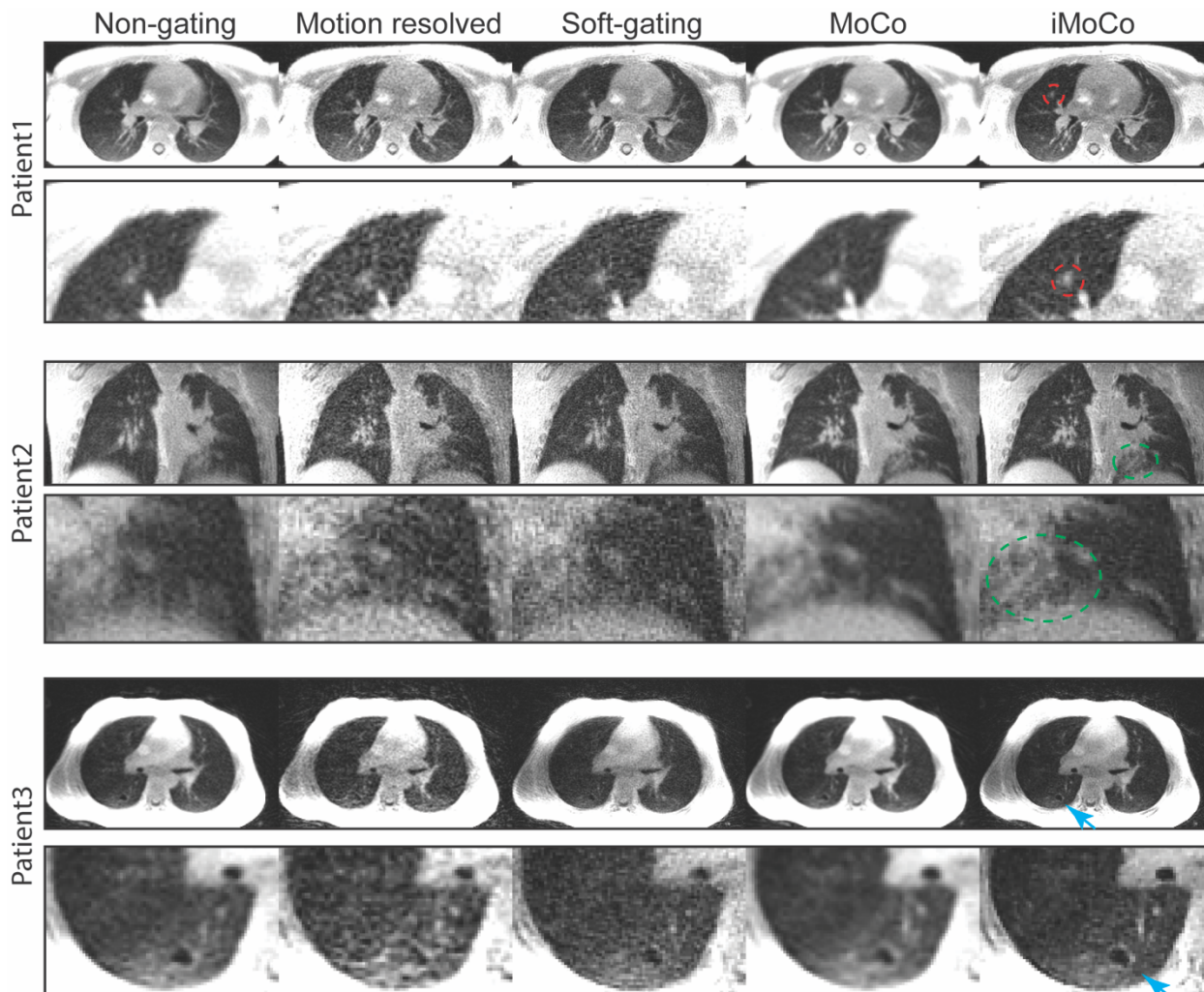
Figure 3.4 Pediatric patient study examples. Three different patient lung UTE scan (1mm isotropic resolution) results with different motion correction and reconstruction strategies are plotted. A lung nodule is pointed out (red dashed circle) in patient 1 (5 y/o). A region of ground-glass opacity is shown (green dashed circle) in patient 2 (4 y/o). Small pneumatoceles (lung cysts) are pointed out (blue arrow) in patient 3 (8 y/o). Abnormality regions of all examples are zoomed in, shown in the second rows.

3.3.3. Hyperparameters Selection

In the proposed iMoCo reconstruction Equation (3-2), there are two tunable

hyperparameters, one is number of motion states, and the other is the TGV

regularization weighting. Experiments with different hyperparameters were designed to

investigate the selection of hyperparameters for the reconstruction.

iMoCo reconstructions carried out using different numbers of motion states are

compared in Figure 3.5.

In the example, the diaphragm motion range was ~1cm, the motion resolved spatial

resolution was 1.5mm, and the final resolution was 1.25mm. As the number of motion

states increased from 2 to 6, the reconstructions improved, especially close to

diaphragm (green arrow), however, trivial improvement was observed as the number

increased from 6 to 8. We also quantitatively evaluated the effects from number of

motion states on the final motion correction performance. The diaphragm maximum

derivative (MD) were used to represent the motion correction performance, plotted in

(b). Higher MD means better motion correction result. As number of states increase 2 to

6, 4 out of 4 cases show MD increase. As number of states goes larger, the

improvement is inconsistent among different cases. Therefore, we believe the number

of states could be estimated by the motion range divided by the motion resolved

reconstruction resolution (in this example, 1cm / 1.5mm = 6.6). 8 motion states were

used in all the results in this work.

Exhale ⟶ Inhale

1cm

(a)

bin=2   4   6   8

(b)

(c)
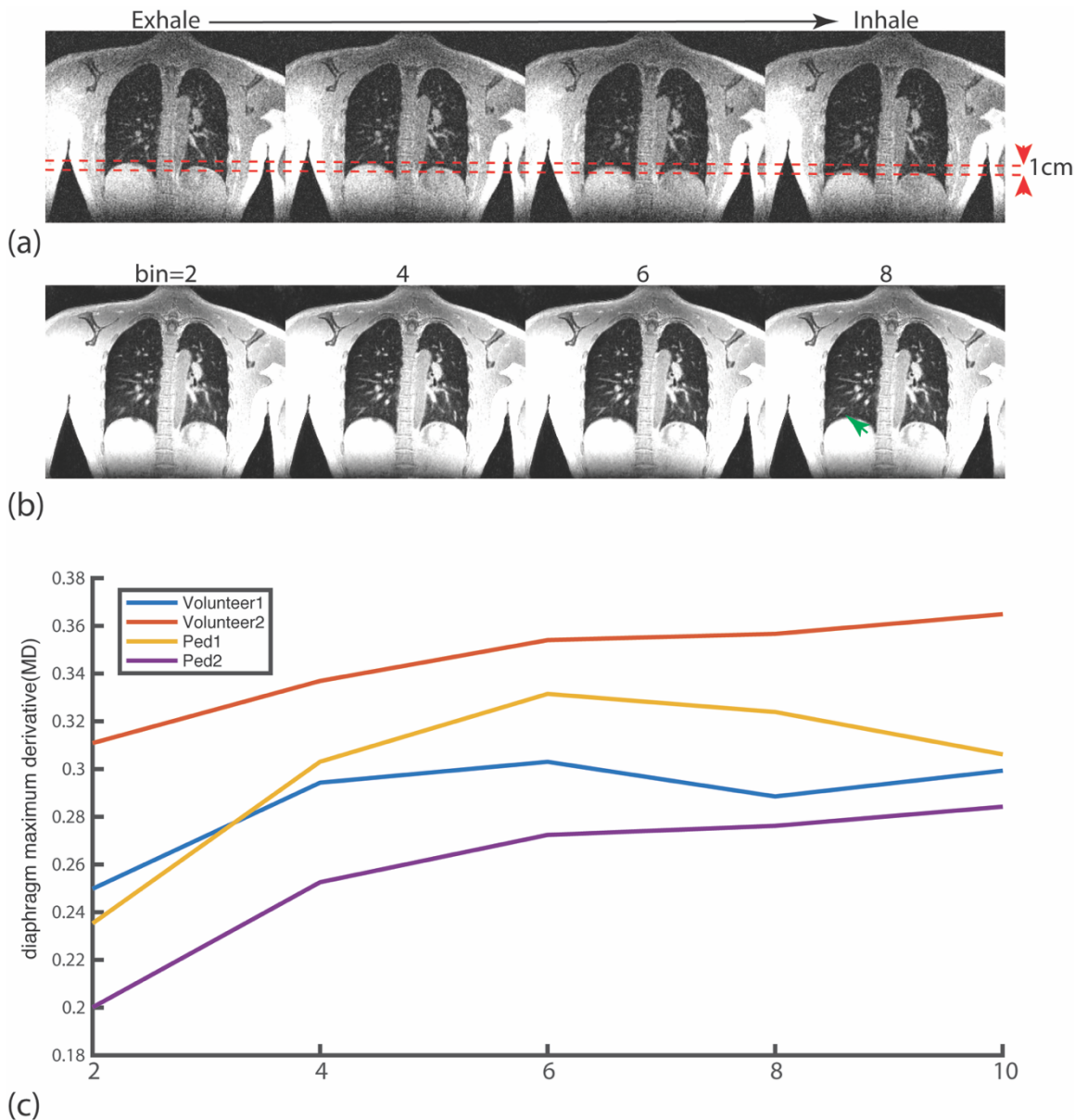
Figure 3.5 Effect of the number of motion states on the iMoCo reconstruction. An example in a healthy volunteer is shown. A motion resolved reconstruction (8 motion states) is shown in (a), where the diaphragm motion from exhale to inhale state is ~1cm. The iMoCo reconstruction with different motion states bin numbers are plotted in (b). Diaphragm maximum derivative (MD) are from 4 cases (2 from volunteers and 2 from pediatric patients) reconstructed via iMoCo using different number of motion states are plotted in (c).

In Eq. 2, λ_s is the hyperparameter tuned to control spatial TGV regularization term. The reconstruction with TGV regularization will reduce the noise, and suppress undersampling and residual motion artifacts. Reconstructed images with different λ_s are

shown in Figure 3.6, using image data from one of the high resolution studies shown in

Figure 3. As λ_s increases, the noise and streaking artifacts are reduced. However, as λ_s

increases to 0.1, the overall images look over-smoothed, especially as some small

vessels are blurred out, seen in the green circle area in Figure 3.6 (a). MIP of 30 slices

are shown in (b) to further compare the effect of λ_s on small structures. $\lambda_s = 0.05$ shows

less noisy without sacrificing the small vessels structures. aSNR measurements are

used to present quantitatively present the effect of λ_s, where Figure 3.7 shows the

aSNR change from airway, lung parenchyma and aortic arch as λ_s increases. Although

the all the aSNRs increase along λ_s, aSNR in airway is expected to be 0, which

indicates that λ_s goes to 0.1 or higher is over-regularized. Therefore, λ_s was set to 0.05

for the iMoCo reconstructions.
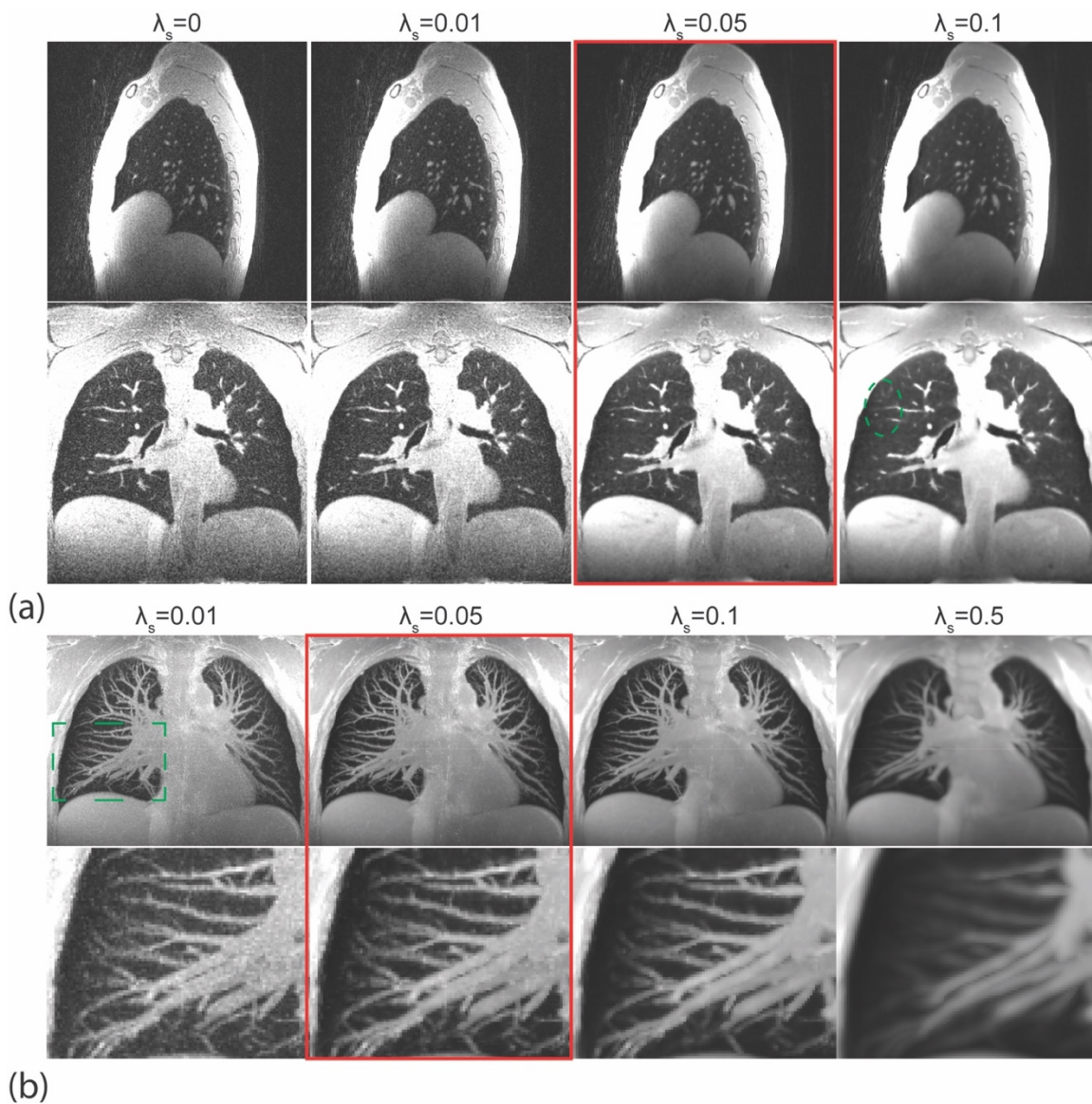
Figure 3.6 Effect of TGV sparse constraint parameter λ on the iMoCo reconstruction. A sagittal and coronal slice from a healthy volunteer with different TGV constraint parameter λ, from 0 to 0.1, are shown in (a). Maximum Intensity Projection (MIP) of 20 coronal slices of the reconstructed volume with different regularization levels are shown in (b), first row shows the MIP images, second shows the zoomed-in image of rectangular area in the first image.
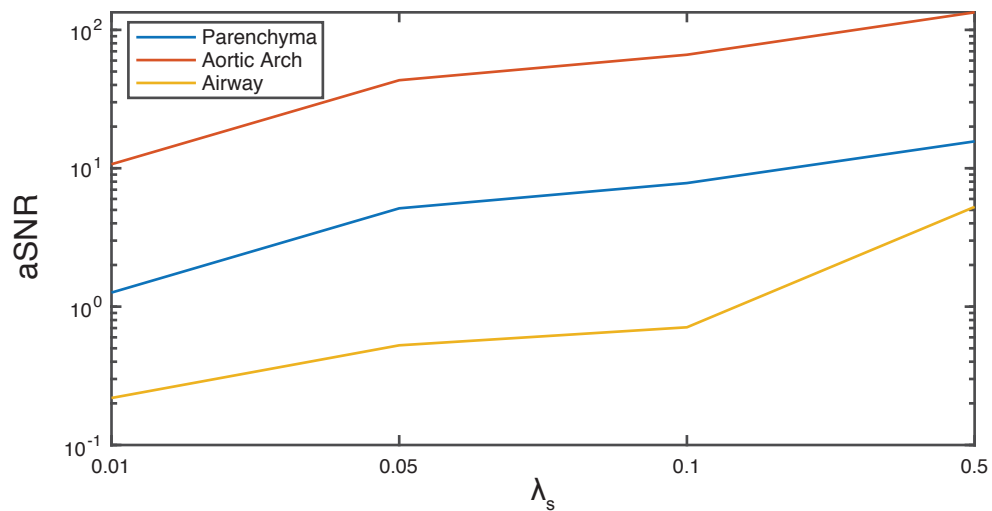
Figure 3.7 aSNRs comparison with different TGV regularization. aSNRs in three different areas (lung parenchyma, aortic arch, and main airway) with different TGV regularization λ_s levels from one of the cases shown in Figure 3.6.

3.3.4. Quantitative Measurement

For all volunteer (n=7), and pediatric patient (n=4) studies, we quantitatively measured the MD on 10 sagittal slices with different motion correction strategies, and normalized the MD to the mean liver signal intensity close to the diaphragm. Measurements are summarized in Figure 3.8.

   Images carried out by iMoCo methods show significantly higher MD value compared to non-gating, soft-gating ,and MoCo methods. 6 out of 11 subjects had the highest diaphragm MD with iMoCo reconstruction.
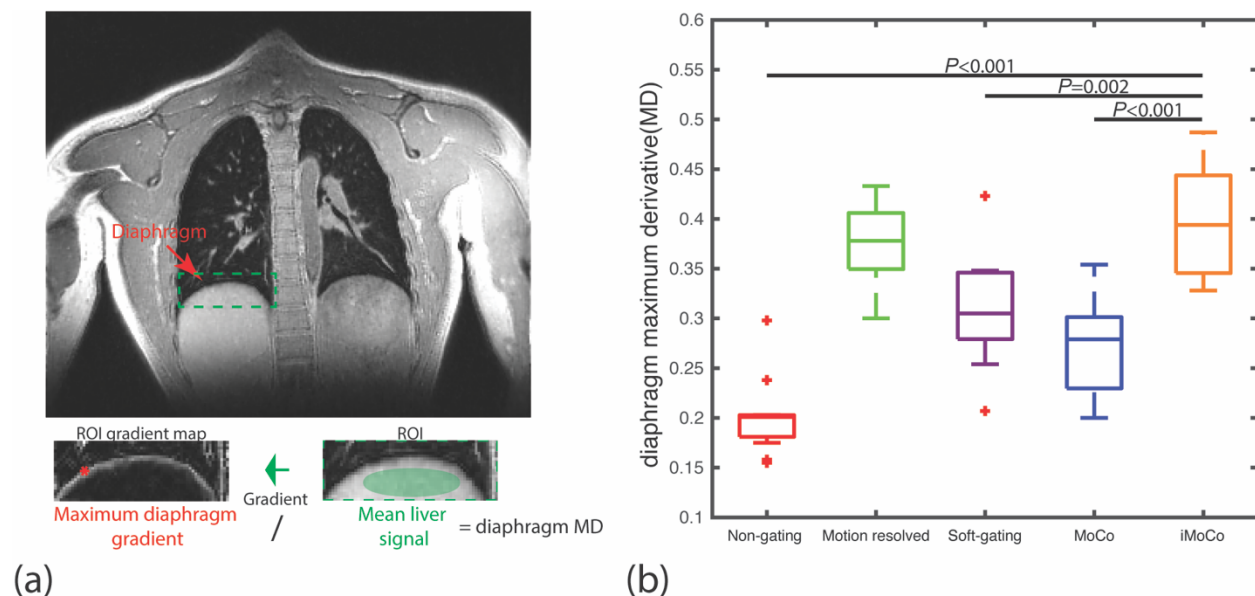
Figure 3.8 Diaphragm maximum derivative (MD) comparison, where a higher MD corresponds to a sharper edge. The MD calculation process is shown in (a). A MD comparison evaluated on 11 subjects (7 adult volunteers, and 4 pediatric patients) across different methods are plotted in (b).

   We also measured the aSNR and CNR of certain regions in the lung, and the results are summarized in Figure 3.9. The aSNR in airways is expected to be close to 0 since there is very little ^{1}H density in air, and aSNR in lung parenchyma and aorta approximate the SNR level of short and long T2* tissues, respectively, with the

reconstruction methods. The aSNR increase in MoCo images can be attributed to the lower apparent spatial resolution due to smoothing effects induced by the deformation interpolation, which can be observed in the image results in Figure 3.2-Figure 3.4. Images with iMoCo reconstruction have higher lung parenchyma and aortic arch aSNR, compared to motion resolved and soft-gating reconstructions. In addition, the airway aSNR with iMoCo is relatively low, which would benefit distinguishing airways from lung parenchyma. In Figure 3.9 (c), iMoCo has significant higher CNR of the lung parenchyma and aortic arch, compared to soft-gating and motion resolved reconstructions.
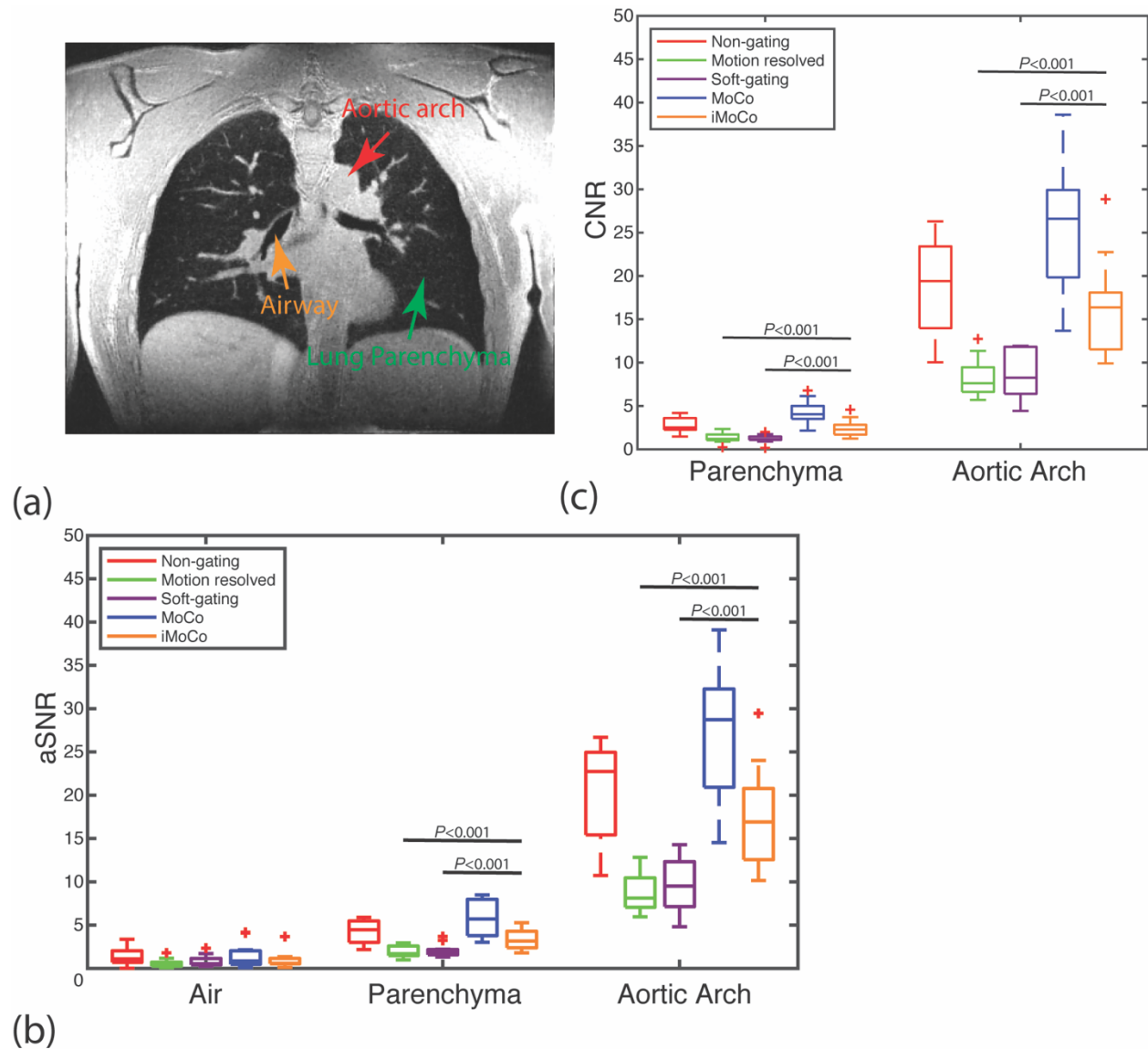
Figure 3.9 Apparent SNR(aSNR) and contrast-to-noise ratio (CNR) comparison between the reconstruction methods. Three different anatomical structures, a major airway, representative lung parenchyma ,and the aortic arch were manually annotated for aSNR and CNR measurements. An example of anatomical structures used for the measurements are shown in (a). Comparison of aSNR and CNR are separately plotted in (b), and (c). The increase in aSNR for the MoCo can be partially attributed to a loss of resolution due to smoothing in the reconstruction, which can be observed in Figs. 2-4. iMoCo had significantly higher parenchyma and aorta aSNR and CNR compared to motion-resolved and soft-gating reconstructions.

These quantitative measurements indicate that iMoCo method can not only achieve higher aSNR, but also reduce respiratory motion artifacts, which would benefit the relatively low SNR found in lung MRI.

3.3.5. Feasibility of Infant Study

The significance and feasibility of infant and neonatal lung MRI studies has been reported in previous work[39,70,71]. High spatial resolution and sufficient SNR are required to visualize smaller structures of the lungs. Figure 3.10 shows one 5-minute UTE scan of an unsedated 10-week-old infant with Pulmonary Interstitial Glycogenosis (PIG) with 0.9mm isotropic resolution.
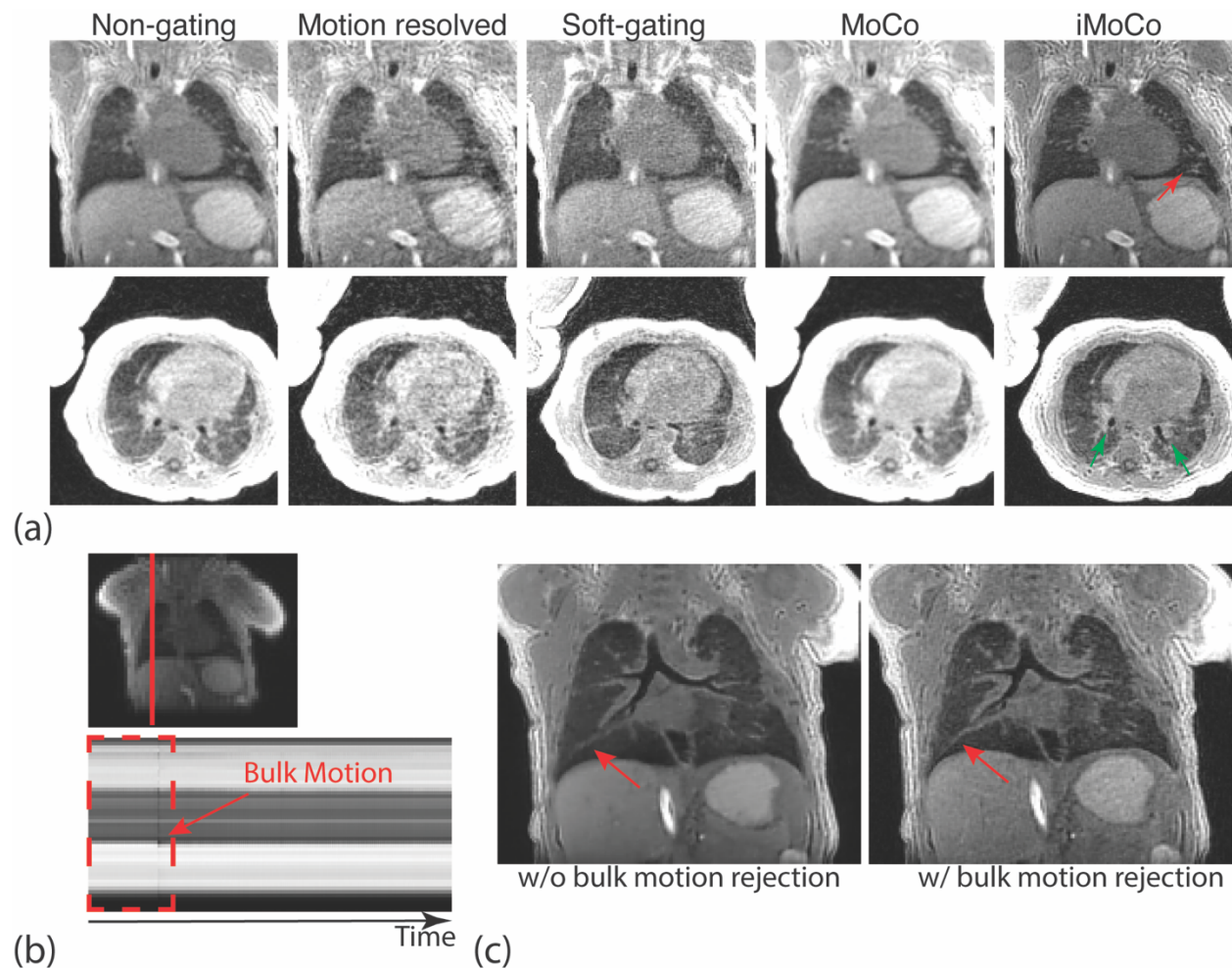
Figure 3.10 10-week-old infant study results. (a) One coronal and one axial slice reconstructed with different motion correction and reconstruction strategies (with bulk motion rejection) are plotted. Vessels (red arrow) and airways (green arrows) are pointed out on the iMoCo images, showing improved delineation and contrast compared to other methods. (b) Bulk motion of the infant during the 5-minute scan was detected by an image based navigator, so data acquired prior to the bulk movement (red dashed rectangle time window) were rejected. (c) Images reconstructed by using iMoCo with and without bulk motion rejection are shown, where bulk motion rejection further reduces the motion effects.

Vessel structures (red arrow) and airways (green arrows) are largely improved with iMoCo reconstruction compared to other methods. An image based navigator[34] was also used in this study to capture the bulk motion of the baby, then the data corrupted by bulk motion were rejected, shown in (b). Image results with bulk motion rejection shows sharper vessels and diaphragm (red arrows) compared to without bulk motion rejection, in (c). iMoCo with the same hyperparameters were used for both of the Figure 3.10 (c) reconstructions.

3.4. Discussion

In this work, I proposed a new motion correction strategy by combining UTE, motion compensation, and a compressed sensing reconstruction to achieve high resolution free breathing lung MRI, called iMoCo UTE. Although soft-gating type reconstruction strategies have been widely used, they inevitably suffer from the residual motion in the reconstruction data. As the desired reconstructed spatial resolution goes higher, fine structure cannot be reconstructed due to this residual motion. The other option is to use a motion resolved type reconstruction, where all data are binned to different motion states then using spatial similarity across different motion states to reduce the downsampling artifacts. As the number of bins increases, on one hand, the residual motion would reduce, however, on the other hand, a higher undersampling factor in each bin would induce undersampling artifacts. iMoCo, aims to model the respiratory motion effects, and incorporate spatial motion compensation instead of directly weighting data or segmenting data. Through volunteers and pediatric patient studies,

iMoCo shows capability to achieve high resolution, high SNR lung images without inducing motion artifacts. According to the quantitative comparison, the iMoCo and motion resolved reconstructions have the highest MD, and iMoCo and MoCo have higher aSNR compared to other methods. In addition, iMoCo is a general motion correction and reconstruction framework, so it could be extended to other applications, and is compatible with different trajectory designs.

3.4.1. Motion Resolved Reconstruction and Motion Fields Estimation

In iMoCo reconstruction, motion fields estimation largely depends on the motion resolved reconstruction as well as registration algorithms. Two experiments are designed to compare the final estimated motion fields with different reconstructions and registration algorithms.

The first experiment is designed to investigate how the regularization terms in the motion resolved reconstruction affect the motion estimation that is used for the motion compensation. Three different regularization combinations were used in this experiment, where the weightings for regularizations were empirically selected based on our previous experiments. All three reconstructions have motion dimension total variation regularizations (temporal TV) following the standard XD-GRASP[49] reconstruction. After all reconstructions, the same Demons based non-rigid registration was used to estimation the motion field. An example of motion fields comparison in shown in Figure 3.11. And the correlation coefficients and mean Euclidean distances

among three motion fields indicate the motion fields are very consistent, indicating the motion estimation is robust to change of the regularizations, summarized in Table 3.1.
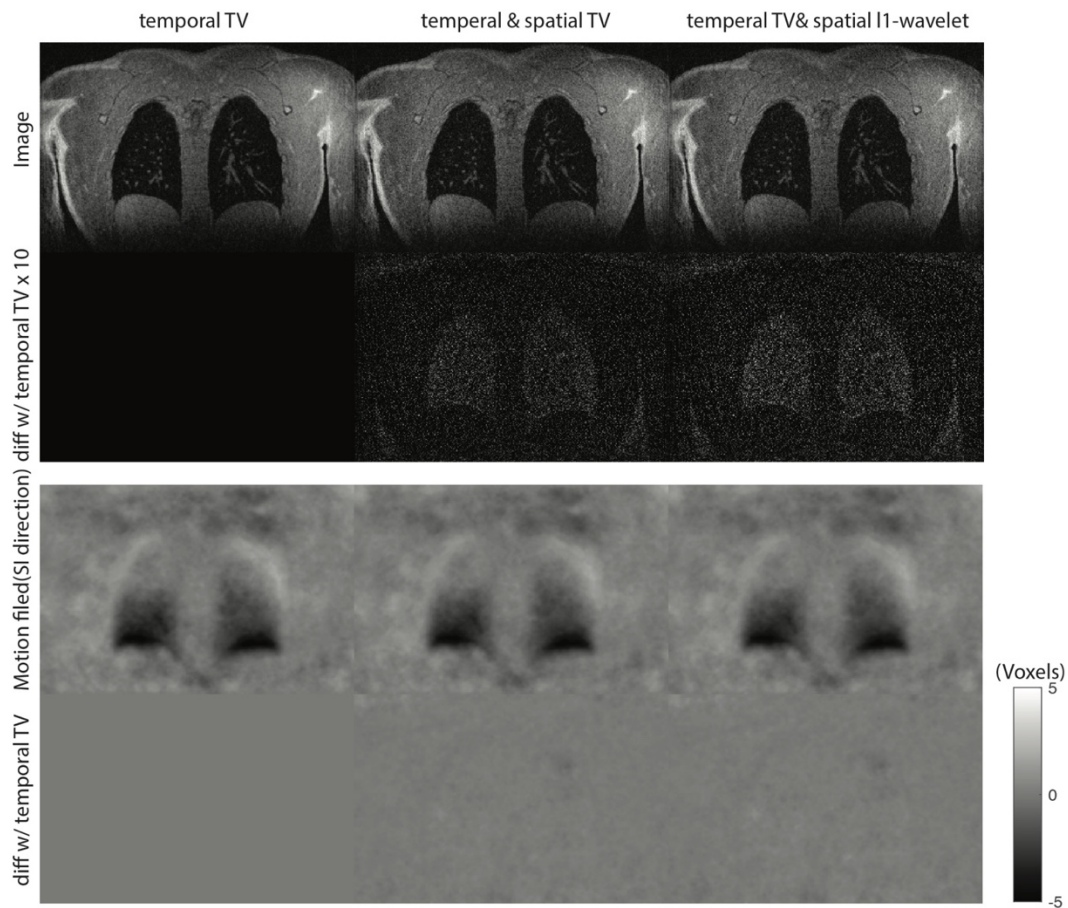
Figure 3.11 Example of motion resolved reconstructions. In the first row are one end expiratory state image from the motion resolved reconstructions. In the second row are the estimated motion field in the S/I direction between the expiratory to inspiratory state.

Table 3.1 Summary of correlation coefficient and mean Euclidean distance of motion fields with different regularizations.

N = 11	Temporal & spatial TV	Temporal TV & spatial l1-wavelet
correlation coefficient	0.95±0.02	0.99±0.01
mean Euclidean distance (voxels)	0.20±0.04	0.07±0.04

The second experiment is to evaluate different registration algorithms including Demons, SyN with mean square error (MSE) similarity[72], and b-spline registration[73], as shown in Figure 3.12 . According to the results, Demons based and SyN with MSE similarity registration well registered two different motion states images. However, slight misalignment could be seen by using b-spline registration.
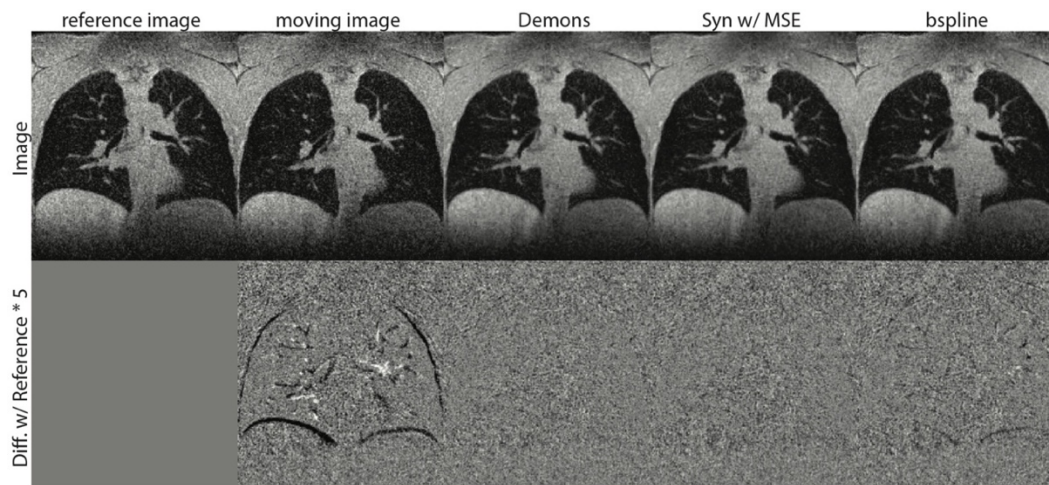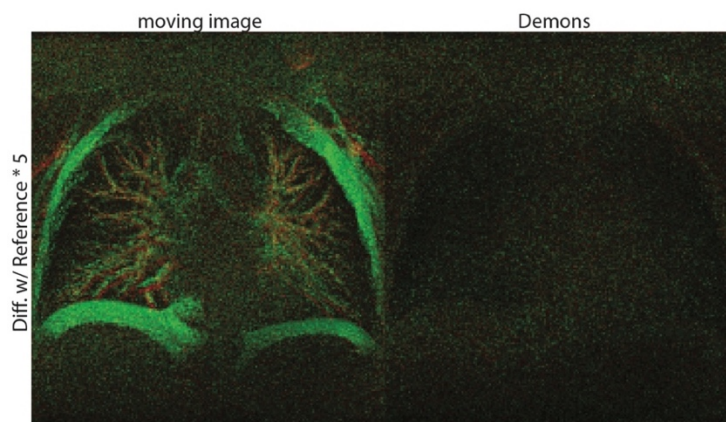
Figure 3.12 Performance comparison among different registration methods. Three different registration methods, Demons, SyN with MSE similarity, and bspline, results are plotted in first row, (a). Difference between aligned image and reference image are plotted in second row, (a). Maximum Intensity Projection of the difference map between aligned image and reference image are shown in (b).

As mentioned in the results, the number of motion states in motion resolved reconstruction determines the intra-bin residual motion, which would significantly affect the final reconstruction. However, iMoCo also largely depends on the motion field estimation. More motion states might degrade the motion resolved reconstruction images, leading to image registration errors. iMoCo also depends on accurate motion field estimation, and errors in the motion field would propagate to final reconstructed image causing blurring or ghosting artifacts.

Previous UTE lung studies have reconstructed 4-6 motion states in motion resolved reconstruction with an approximately 2-fold undersampling rate overall that resulted in around 10-fold undersampling rate in each motion state data[34,50]. For the motion resolved reconstruction this work, we increased the number of motion states to reduce the intra-bin motion and also used a slightly coarser spatial resolution to reduce the undersampling rate. This was aimed to ensure that the reconstructed image quality would not degrade the motion fields estimation and following motion compensated reconstruction. We set the motion resolved reconstruction to 1.5mm isotropic resolution to keep the undersampling rate in single motion state under or around 10, as the number of motion states was set up to 12, while providing images that could distinguish inter-bin motion as small as 1.5mm.

The regularization terms and values for the motion-resolved reconstruction in Equation (3-1) were chosen empirically based on qualitative evaluation. There also maybe room to improve the proposed method through more sophisticated techniques, such as locally low rank contraints[74], which also could improve the overall iMoCo method.

In this work, we used one-to-one image registration between pairs of motion state images, and registration error might be further reduced by using group-wise registration. All the motion states images could be registered simultaneously, which might improve the robustness of registration process by taking advantage of the registration correlation among the motion states, and some work has shown promising results in 4D CT applications[75].

3.4.2. 3D Navigator and Irregular Motion Handling

In this chapter, the self-navigator signals are simply used for respiratory motion binning. By using more sophisticated techniques, a 3D image based navigator could be extracted, then used to detect the bulk motion or irregular motion. In this work, data contaminated with bulk motion are discarded[34,39], which reduces the scan efficiency. We could also be able to incorporate bulk motion or even more complicated irregular motion into iMoCo reconstruction, which might increase the scan efficiency as well as robustness to irregular motion.

3.4.3. Respiration Related Pulmonary Abnormalities

Some pulmonary abnormalities, such as air trapping, might lead to local intensity changes during respiration[76]. One of the limitations of our studies is that iMoCo assumed no signal intensity change over time in the models, which might lead to missing the dynamic change of the abnormalities during respiration. In the next chapter, I extended the iMoCo reconstruction to a higher dimension reconstruction to overcome the drawback.

3.5. Conclusion

In this work, we proposed a new free breathing high resolution pulmonary MRI strategy, combining motion compensation, UTE, and compressed sensing, called iMoCo UTE. iMoCo UTE has been validated and evaluated via both volunteers and patient studies, and shows potential in pediatric and infant pulmonary MRI studies.

Chapter 4 Motion Compensated Low-rank Constrained (MoCoLoR) Reconstruction for 4D MRI

4.1. Introduction

As mentioned in the previous chapter, motion, especially respiratory motion, is one of the most challenging problems in thoracic as well as abdominal MRI, because of the limited encoding speed of MRI. Routine clinical protocols require patients to hold breath for single or multiple short durations (10~15 seconds) to reduce motion. However, for 3D high resolution or 4D, such as dynamic contrast-enhanced, acquisitions, the total scan time would increase to a few minutes, which is impossible for patients to sustain breath-holds, and even shorter breath holds are challenging for pediatric patients and the patients suffering from compromised pulmonary function. Alternatively, external devices are used to monitor respiratory motion and trigger acquisition at specific motion states to reduce motion artifacts, but it would largely reduce the scan efficiency and prolong the total acquisition time.

3D non-Cartesian acquisition schemes, such as kooshball[20], cones[22], Stack-of-Stars[49], etc., have a few advantages over Cartesian schemes in the free breathing acquisition situation. Firstly, most of the non-Cartesian acquisition schemes repeatedly acquire the center k-space, which could be used as a self-navigator retrospectively gating data to certain motion state. In addition, by adding a random or pseudo-random

ordering[77–79] into the design, non-Cartesian acquisitions would have increased temporal

sampling incoherence, which would improve the following motion correction steps.

To reduce motion artifacts without sacrificing scan efficiency, one widely-used

strategy is to group data into different motion states based on the motion signal, then

reconstruct multiple motion states images using compressed sensing and parallel

imaging, called motion resolved reconstruction. One well-known regularization used in

the compressed sensing reconstruction is the total variation (TV) norm along the motion

states dimension, and implementation details are described in XD-GRASP[49]. An

alternative to the TV constraint is to reformulate the image series into a spatio-temporal

matrix, known as Casorati[80] matrix, then enforcing low-rank or locally low-rank on the

Casorati matrix, which has been used in free breathing cardiac MRI, as well as dynamic

contrast-enhanced (DCE) MRI[81–83].

However, it has been reported in some computer vision applications that the low-rank

model breaks down if the images are misaligned[84]. Similarly, in MRI applications,

especially under free breathing imaging situation, the low-rank model might also fail

because of the subject motion induced misalignment. Some recent studies integrate

motion information in the low-rank constrained reconstruction models, such as motion

adaptive patch-based low-rank constrained reconstruction[85,86], and block low-rank

sparsity with motion-guidance reconstruction[87]. The main idea of the above methods is

to preserve the low-rank property of spatio-temporal matrices by searching the similar

patches locally from the image series. However, when the problem extends from 2D to

3D, the patch-based searching strategy might largely increase the computational

complexity. In addition, all patch-based methods are assuming that the spatial

misalignment is only caused by translational motion. However, the assumption might not hold when it is applied to the thoracic and abdominal imaging[88].

In this work, I proposed a new strategy to directly incorporate motion compensation in the low-rank constrained reconstruction model, called Motion Compensated Low Rank (MoCoLoR) reconstruction. There are two major steps in the MoCoLoR reconstruction framework. The first step is a motion survey. Lower quality motion resolved or dynamic images are reconstructed for motion field estimation. Secondly, derived motion information, such as respiratory motion or bulk motion, are added into the low-rank constrained reconstruction framework. We applied the proposed technique to two different studies: 3D high resolution motion resolved lung MRI, and 3D DCE abdominal MRI. The results showed that the proposed MoCoLoR method could further reduce motion artifacts and noise compared to the methods without motion compensation.

4.2. Theory

4.2.1. MRI Signal Model with Motion

The general non-Cartesian MRI acquisition can be modeled as below,

$$d_i(\boldsymbol{k}, t) = \int S_i(\boldsymbol{r}) I(\boldsymbol{r}, t) \exp\left(-i2\pi \boldsymbol{r}\boldsymbol{k}\right) \mathbf{d}\boldsymbol{r} \tag{4-1}$$

Here, the $\boldsymbol{r}$ and $\boldsymbol{k}$ are locations in image and k-space domain respectively. $S_i (i = 1,2,\dots N)$ represent coil sensitivity maps, $I(\boldsymbol{r}, t)$ are motion resolved or time resolved images, $d_i(\boldsymbol{k}, t)$ are k-space data.

For free breathing acquisitions without contrast enhancement, we assume that image changes are associated with respiratory motion. Then, acquisition model could be extended to incorporating motion information,

$$d_i(\boldsymbol{k}, m) = \int S_i(\boldsymbol{r})I(\boldsymbol{r}, m)\exp(-i2\pi\boldsymbol{r}\boldsymbol{k})\mathbf{d}\boldsymbol{r}. \tag{4-2}$$

The continuous acquisition could be segmented to finite motion states, indexed by m. Furthermore, all the linear operators could be discretized as matrix multiplications,

$$d_i(\boldsymbol{k}, m) = P(\boldsymbol{k}(m))FS_i(\boldsymbol{r})I(\boldsymbol{r}, m) = \boldsymbol{E}(m)I(m) \tag{4-3}$$

Here, $P(\boldsymbol{k}(m))$ represents non-Cartesian sampling pattern in the k-space at a certain motion state m. F represents the Fourier transform. $P(\boldsymbol{k}(m))FS_i(\boldsymbol{r})$ could be combined into a single linear operator $\boldsymbol{E}(m)$.

As for DCE MRI studies, contrast change over time should be included in the signal model as well. The continuous acquisition data would be sorted by time, and motion states m would be also indexed by time. Equation (4-3) could be rewritten to include contrast change as below,

$$d_i(\boldsymbol{k}(t), m(t)) = P(\boldsymbol{k}(t))FS_i(\boldsymbol{r})I(\boldsymbol{r}, m(t), t) = \boldsymbol{E}(t)I(m(t), t) \tag{4-4}$$

Here, $m(t)$ represents the motion state at a certain time t. And $I(\text{t})$ is a dynamic image series with the $m(t)$ motion state. To derive and model the subject motion, a motion survey step is required before the final reconstruction.

Two types of motion, bulk motion and respiratory motion, are considered within the scope of free-breathing body MRI. **Error! Reference source not found.** illustrates how to derive the above two types of motion from the continuous 3D radial acquisition.
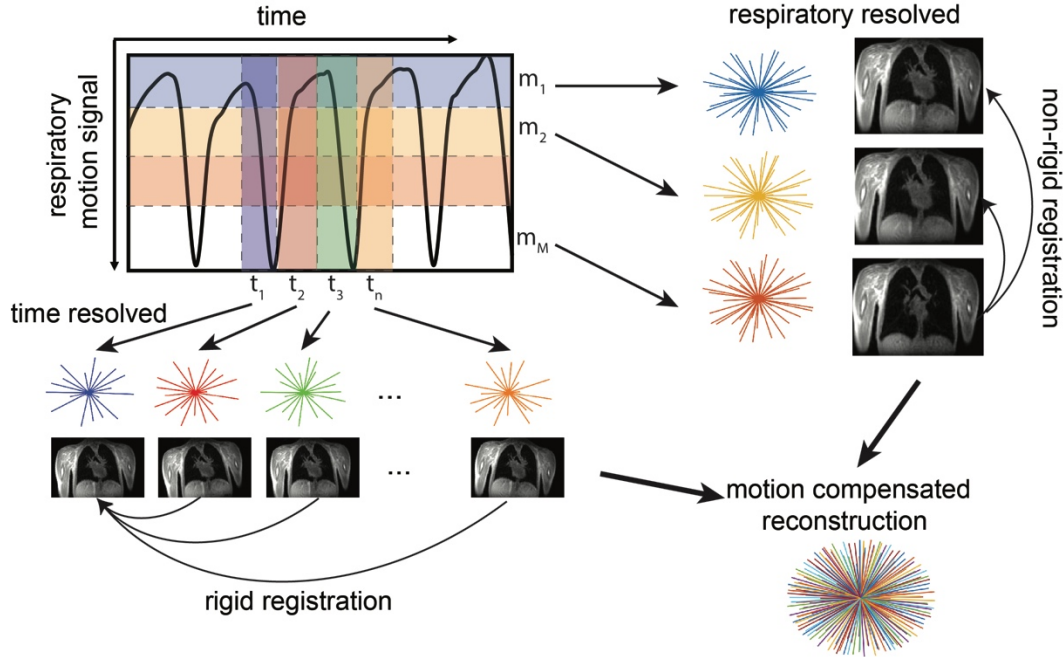
Figure 4.1 Workflow of bulk motion and respiratory motion estimation for 3D radial sequence. For bulk motion, data are sorted by acquisition order, and high temporal but low spatial resolution images are reconstructed, then rigid registration is applied to derive the bulk motion over time. For respiratory motion, data are binned to different respiratory motion states based on the respiratory signal. Then different motion states images are reconstructed by constrained motion resolved reconstruction, followed by a non-rigid registration to derive respiratory motion. Finally, both the derived bulk and respiratory motion are incorporated in the proposed reconstruction.

4.2.2. Bulk Motion Estimation

Typically, high resolution 3D free-breathing acquisitions take a few minutes, and the longer acquisition time would have a larger possibility to induce bulk motion. To capture the bulk motion, we applied the time resolved reconstruction on the center k-space to generate high temporal resolution coarser spatial resolution image navigator[34]. Then, a frame-by-frame image based rigid registration is applied on the image navigators to capture bulk motion.

$$\underset{M_{bulk}(t,t_0)}{\operatorname{argmax}} \ \mathrm{MI}\big(I_t, M_{bulk}(t,t_0)I_{t_0}\big) \tag{4-5}$$

Here, I_t represents the image navigator at certain time point t, and t_0 is the reference time point. $M_{bulk}(t, t_0)$ is the rigid transformation from time point t to the reference time t_0. And the similarity objective function is mutual information, MI[89].

4.2.3. Respiratory Motion Estimation

Since the center k-space data can be repeatedly acquired in each or every few TRs with non-Cartesian acquisition schemes, a self-navigator technique is applied to extract respiratory motion information. The multi-channel center k-space data are combined with varied α_i via an optimal weighting strategy,

$$d(\mathbf{0}, m(t)) = \sum_{i=1}^{N_{coil}} \alpha_i P(\mathbf{0}) FS_i(\mathbf{r}) I(\mathbf{r}, m, t) \tag{4-6}$$

Then, the combined self-navigator signals go through a low-pass filter (cut off frequency at 1Hz), and baseline correction, as described in Chapter 4. As for DCE MRI, we assume that the self-navigator signal could be modeled as an low frequency baseline drift added to the motion signal, which could be removed via baseline correction

$$\hat{d}(\mathbf{0}, m(t)) + C(t) = d(\mathbf{0}, m(t)) \tag{4-7}$$

After that, data are then binned to different respiratory motion states, indexed by m. Binned data are used to reconstruct images representing different motion states I_m via the motion resolved reconstruction. Since the motion resolved images are usually highly undersampled, a regularization term with TV constraint along the motion dimension and a reduced reconstruction resolution are used to reduce undersampling artifacts, which would benefit the following registration step.

$$\underset{I_m,\, m\in\{1,2,\dots M\}}{\mathrm{argmin}} \frac{1}{2}\left\|\boldsymbol{E}_m I_m - d(\boldsymbol{k},m)\right\|_2^2 + \lambda_{TV}\left\|\nabla_m I_m\right\|_1 \qquad (4\text{-}8)$$

Then, deformations from $I_m,\; m \in \{1,2,\dots M\}$ to reference state image $I_{m_{ref}}$ are

derived via image based hierarchical Demons non-rigid registration[90].

$$\underset{M_{resp}(m,m_{ref})}{\mathrm{argmin}} \left\|I_m - M_{resp}(m, m_{ref})I_{m_{ref}}\right\|_2^2 \qquad (4\text{-}9)$$

For DCE images, the pre-contrast data are cropped from the full dynamic dataset

then go through the motion resolved reconstruction and respiratory motion estimation

mentioned above. And the full dynamic dataset goes through a time resolved

reconstruction for rigid bulk motion estimation. The comprehensive motion

transformation is given by combining the respiratory and bulk motion fields:

$$M(t,t_0) = M_{resp}(m(t), m_{ref})M_{bulk}(t,t_0) \qquad (4\text{-}10)$$

Then motion fields are restored for the later low-rank constrained reconstruction.

4.2.4. Motion Compensated Low-rank Constrained

(MoCoLoR) Reconstruction

As mentioned before, spatial misalignment will break down or degrade the low-rank

property of the spatio-temporal matrix. Figure 4.2 describes how spatial registration

affects the low-rank property. A 2D continuous acquired images, (a), are reformulated

as Casorati matrix, (b), then the Casorati matrix would go through the singular value

decomposition (SVD), (c). With image registration, images are aligned well, (d).

Structural information are mainly stored in the first and second components with image

registration. In contrast, without image registration, structural information spread to

higher rank components, (e). Accordingly, the singular values decay faster with than

without image registration, (f).
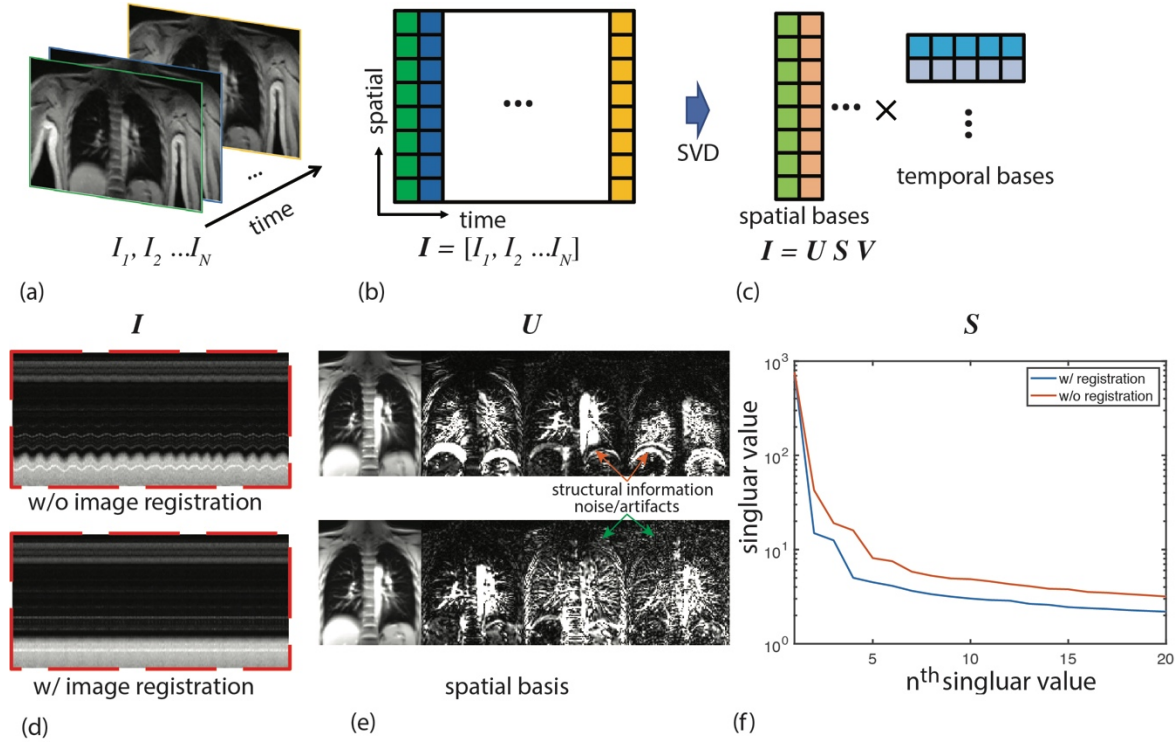
Figure 4.2 Effect of image registration on the low-rank property of the spatio-temporal matrix. Free breathing acquired images (a) are reformulated as spatio-temporal matrix (b). This matrix is decomposed into spatial bases and temporal bases via singular vector decomposition. Line profiles of images series with and without image registration are shown in (d), 4 principal spatial bases and singular values are shown in (e) and (f).

Similarly, to improve the low-rank constrained model, motion compensation is

incorporated into the reconstruction. Then, it could be formulated as an unregularized

optimization problem:

$$\underset{I_m, m \in \{1,2,...M\}}{\operatorname{argmin}} \frac{1}{2} \left\| E_m I_m - d(\boldsymbol{k}, m) \right\|_2^2 + \lambda_L \left\| \mathbf{M I} \right\|_* \qquad (4\text{-}11)$$

Here, the left term is squared-error data consistency term and the right term is low-rank

penalty on the motion compensated spatio-temporal matrix, where $\mathbf{I} = [I_1, I_2, ..., I_m]$ are

the motion-state 3D images, and $\mathbf{M} = [M_1, M_2, ..., M_m]$ are motion fields corresponding to

motion states images, which are derived from the motion estimation step. λ_L is the low-rank penalty regularization parameter.

In (4-11), the **M** operator is a non-invertible transformation, because the spatial interpolation step in deformation would decrease the spatial resolution. However, to solve the original problem directly, $\mathbf{M}^{-1}$ is required, which is not achievable. To avoid $\mathbf{M}^{-1}$ calculation, we can rewrite the problem as below,

$$\underset{Z,I}{\text{argmin}}\frac{1}{2}\left|\left|E_m I_m - d(\boldsymbol{k},m)\right|\right|_2^2 + \lambda_L \left|\left|\mathbf{Z}\right|\right|_*, \ s.t.\, \mathbf{Z} = \mathbf{MI} \tag{4-12}$$

Then the problem could be solved via alternating direction method of multipliers (ADMM)[91]. ADMM would split the optimization problem into two subproblems, and update the subproblems separately.

Data consistency subproblem update

Conjugate gradient descent is used to solve the quadratic programming subproblem,

$$I_m^{K+1} = \underset{I}{\text{argmin}}\frac{1}{2}\left|\left|E_m I_m - d(\boldsymbol{k},m)\right|\right|_2^2 + \left|\left|\mathbf{MI} - \boldsymbol{Z}^K + Y^K/\rho\right|\right|_2^2 \tag{4-13}$$

Low-rank constrained subproblem update

The second step is to update low-rank constraint,

$$\boldsymbol{Z}^{K+1} = \underset{Z}{\text{argmin}}\,\lambda_L \left|\left|\boldsymbol{Z}\right|\right|_* + \left|\left|\mathbf{MI}^{K+1} - \boldsymbol{Z} + Y^K/\rho\right|\right|_2^2 \tag{4-14}$$

Singular value thresholding (SVT)[92] can be easily applied to solve that subproblem.

Dual variable update

After updating all the subproblems, the dual variable is updated via gradient ascent,

$$Y^{K+1} = Y^K + \rho(\mathbf{MI}^{K+1} - \boldsymbol{Z}^{K+1}) \tag{4-15}$$

For DCE MRI, we could reformulate equation (4-10), by sorting data and indexing imaging and motion operators by time t. Then using the same reconstruction algorithm (4-13) to (4-15) to solve.

$$\underset{Z,I}{\operatorname{argmin}} \frac{1}{2}\left|\left|E_t I_t - d(\boldsymbol{k},t)\right|\right|_2^2 + \lambda_L \left|\left|\mathbf{Z}(t)\right|\right|_* \quad s.t. \mathbf{Z}(t) = \mathbf{M}(t)\mathbf{X}(t) \qquad (4\text{-}16)$$

4.2.5. Implementation

Algorithms are implemented using a high-performance workstation with 256GB memory, and Nvidia GeForce Gtx Titan 6GB GPU. Most of the MRI reconstruction operations such as coil sensitivity calibration, and NUFFT are implemented with SigPy (https://github.com/mikgroup/sigpy.git), which is a python package designed for MRI reconstruction. Both rigid and non-rigid registration are carried out by a standard registration toolbox ANTs[72].

4.3. Methods

The proposed methods are applied to two different studies. One is 3D motion resolved lung MRI, the other is 3D abdominal DCE MRI. Both types of studies acquired data under free breathing lasting a few minutes. All the human studies were performed under IRB approval.

4.3.1. 3D Free Breathing Lung MRI

An optimized 3D UTE sequence with a golden angle ordering acquisition scheme was used for free breathing lung MRI. The total scan time was approximately 5 min to 5 min 30 s. $TE = 70\mu s$, $TR = 2.7 - 3.1 ms$ where TR increased as the prescribed FOV was

reduced, flip angle $4°$, bandwidth was 125 kHz, number of total acquired spokes of each scan was approximately 100,000. The spatial resolution was reconstructed 1mm isotropic. The experiment was run on a 3T MR system (GE Healthcare, Waukesha, WI) equipped with an 8-channel cardiac coil.

4.3.2. 3D Abdominal DCE MRI

A golden angle cones trajectory UTE sequence was used for DCE acquisition. Total scan time was 5 minutes 11 seconds, TE=0.1 ms, TR=7.4 ms, flip angle 15 degrees, bandwidth was 125 kHz. The number of readout points was 711, and the number of interleaves was 41,861. The spatial resolution was reconstructed at $1 \times 1 \times 1.8$ mm^3, and the matrix size was $288 \times 156 \times 126$. The experiment was run on a 3T MR system (GE Healthcare, Waukesha, WI) equipped with a 12-channel coil. DCE MRI reconstructions used a 2.8 second (400 readouts per time frame) temporal resolution.

4.3.3. Quantitative Evaluation

Two quantitative metrics are used in this work to evaluate the performance of the proposed MoCoLoR reconstruction. Maximum derivative (MD) of diaphragm is used to evaluate the motion correction improvement, where higher MD value represents sharper diaphragm structure and indicates better motion correction improvement. Since SNR is difficult to measure in *in vivo* studies, the apparent SNR (aSNR), mean signal intensity over background standard deviation is calculated to evaluate reconstructed image quality.

4.4. Results

4.4.1. 3D Free Breathing Lung MRI

For comparison, directly gridding (NUFFT), low-rank constrained reconstruction without motion compensation (NMC LoR), and the proposed MoCoLoR reconstruction are implemented and applied on the same datasets.

30 coronal slices maximum intensity projection (MIP) images reconstructed by different methods are shown in Figure 4.3. Due to the high undersampling factor, noise and streaking artifacts are obvious on NUFFT reconstructed images, and the low-rank constrained reconstruction largely reduces the artifacts and noise. However, the low-rank constraint blurs some detailed features in areas with large motion, such as the diaphragm, because of the spatial misalignment. In contrast, the proposed MoCoLoR method reduces artifacts and noise without blurring out the details. Overall, the proposed MoCoLoR shows sharper vessels than the other two methods, and the improvement of MoCoLoR is obvious in the area with large motion, indicated by the arrows.
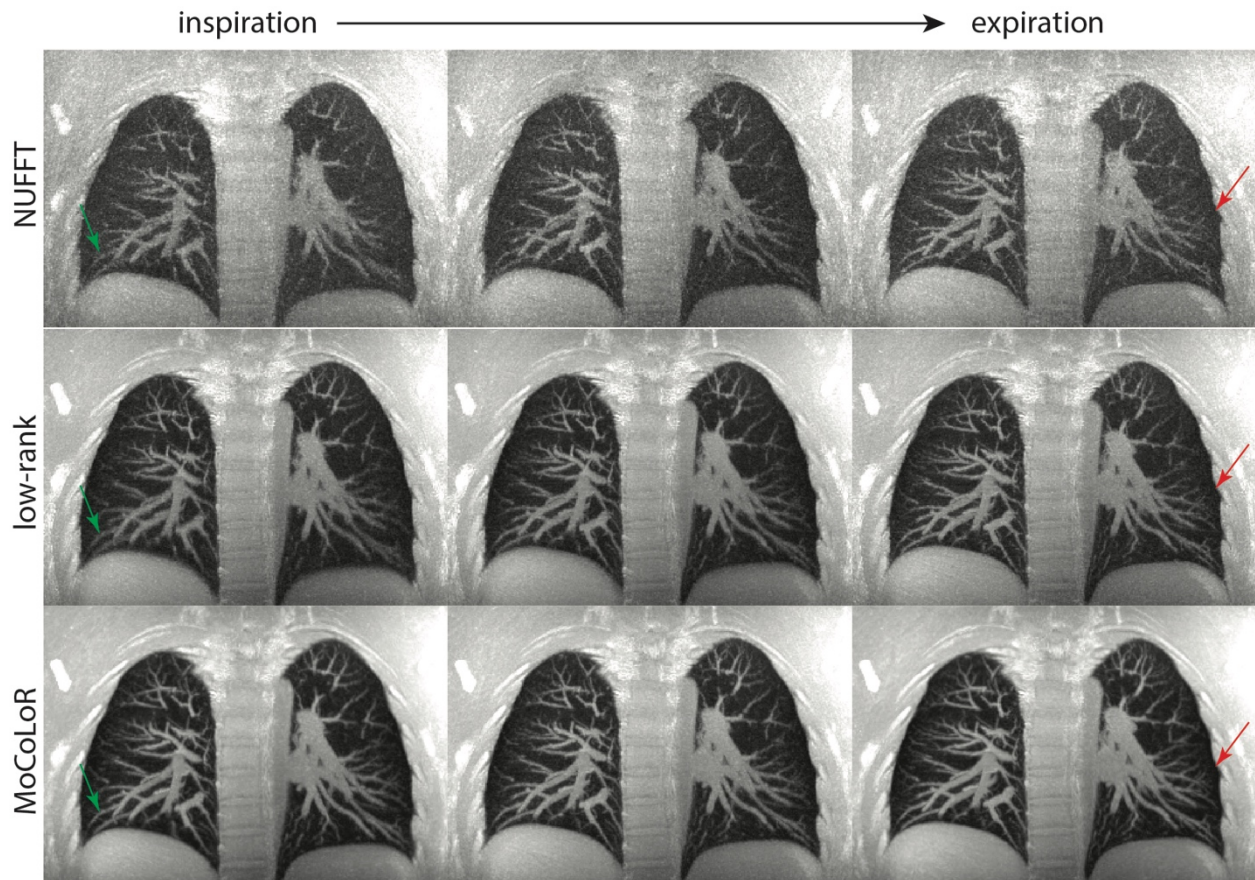
Figure 4.3 Healthy volunteer lung MRI study. Maximum intensity projection of 30 coronal slices reconstructed with the three methods are generated to compare performance among different reconstructions.

MD of diaphragm and aSNR of different structures are measured to evaluate the performance of different reconstructions, summarized in Table 4.1 and Table 4.2. MoCoLoR achieved the highest MD in the inspiration state among the three methods, and similar MD in the expiration state compared to the other two methods. As for aSNR, MoCoLoR achieves much higher vessel and parenchyma aSNR compared to the other two reconstructions, and keeps the airway aSNR close to 0.

A comparison of the patient images is shown in Figure 4.4. A small cyst could be found in the back of the lung, pointed out by red arrows on the right. With NMC LoR, undersampling artifacts are largely suppressed, however, the cyst is blurred and

enlarged in the inspiration state. Images carried out by the MoCoLoR shows clear
contour of the cyst and airway structures.

Table 4.1 Maximum derivative of diaphragm comparison on volunteer lung MRI study.

	NUFFT	Low-rank	MoCoLoR
Inspiration	0.233±0.013	0.178±0.006	**0.275±0.004**
Expiration	**0.282±0.006**	0.266±0.007	0.272±0.003

Table 4.2 Apparent SNR comparison on volunteer lung MRI study.

	NUFFT	Low-rank	MoCoLoR
Vessel	6.67	7.04	**16.6**
airway	0.47	0.28	0.39
parenchyma	1.04	1.15	**2.57**
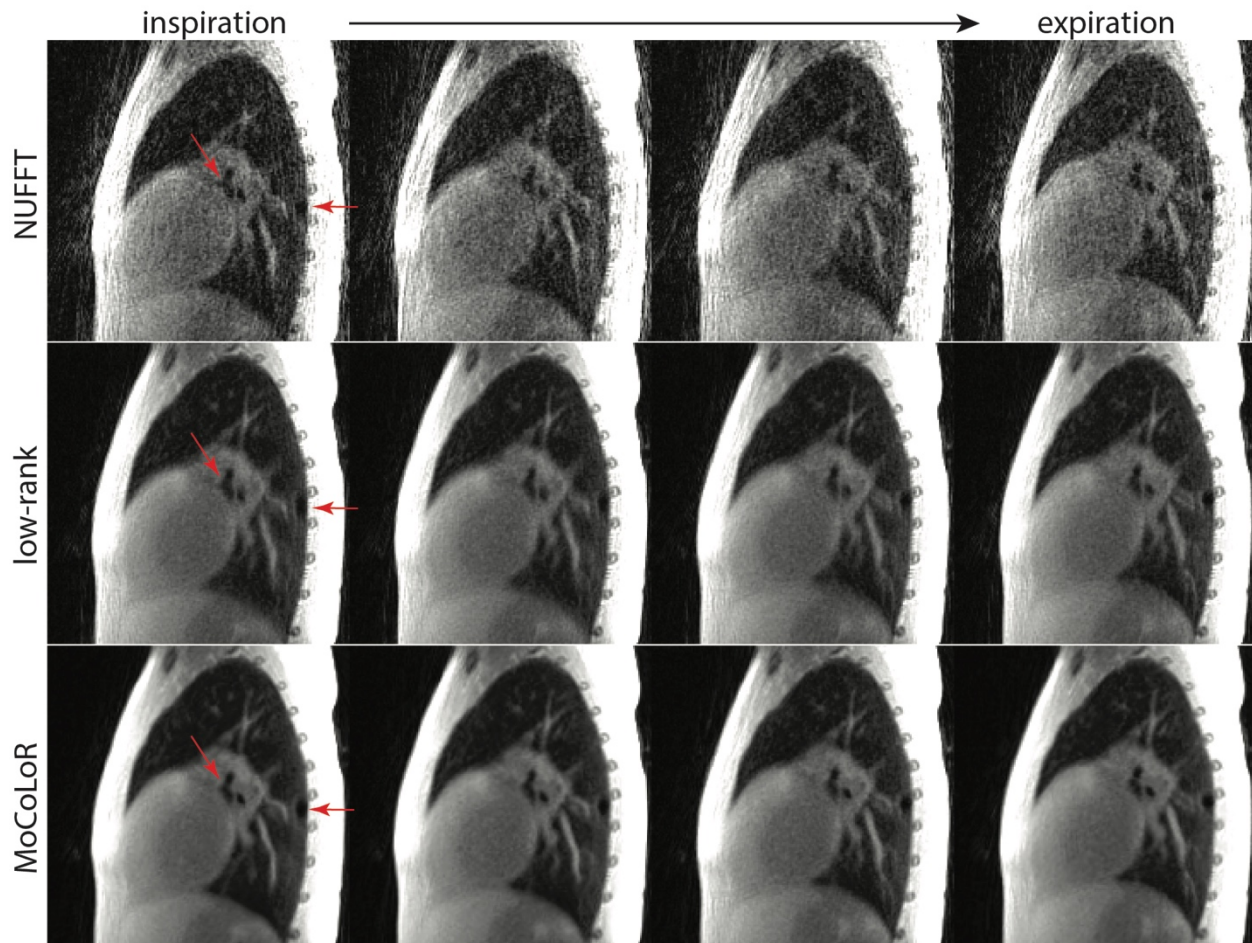
Figure 4.4 Pediatric patient lung MRI study. A pediatric patient was scanned free-breathing with the 3D UTE sequence. Motion resolved images reconstructed by the three different methods from expiration state to expiration state are shown. A small lung cyst, and main airways are is pointed to by red arrows.

4.4.2. 3D DCE MRI

Low-rank constrained without motion compensation (NMC-LoR), Low-rank constrained with soft-gating (SG-LoR), and proposed MoCoLoR reconstructions are compared on the DCE dataset in which there was clear bulk motion of the subject. SG-LoR is implemented following the details in previous work[93]. Two levels of motion compensation are used in the MoCoLoR, one is only respiratory motion compensation (rMC), the other is both respiratory motion and bulk motion compensation (both MC).
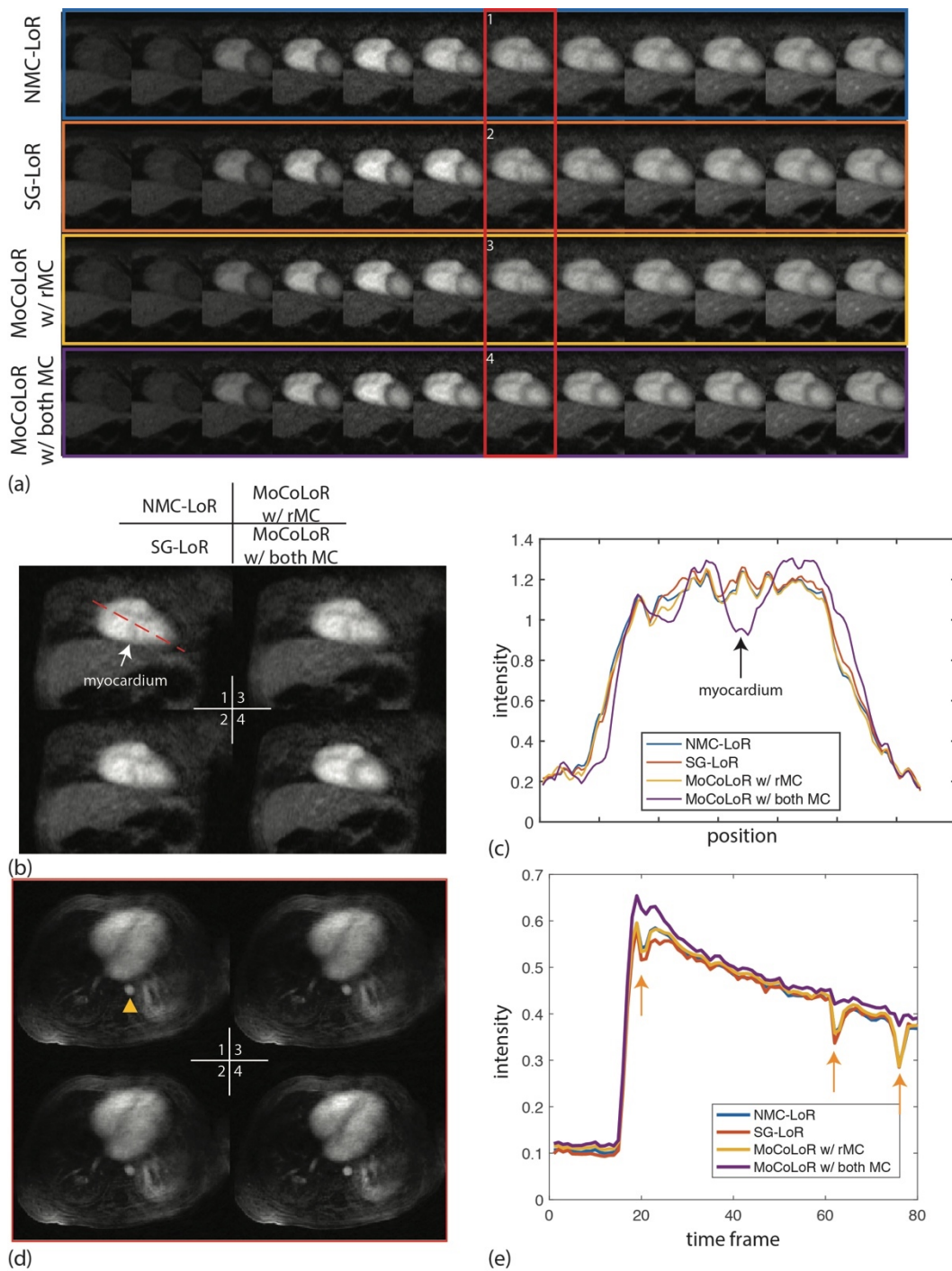
Figure 4.5 DCE MRI reconstruction results. DCE images reconstructed by 4 different reconstruction strategies are plotted in (a). Images framed by the red rectangle are shown in (b). Line profiles across the heart are plotted in (c). The axial plane images are shown in (d). Dynamic signals of thoracic aorta are plotted in (e), the signals corrupted by bulk motion are pointed out by orange arrows.

The results are summarized in Figure 4.5. Dynamic images series covering the contrast arrival process are reconstructed by different algorithms, plotted in (a). Single time point images framed with red rectangle are highlighted, shown in (b), the images are corrupted by bulk motion. With the MoCoLoR with both MC reconstruction, the myocardium is well delineated compared to other methods. Line profiles across the heart are plotted in (c), showing the myocardium can be clearly differentiated from the blood using the MoCoLoR with both MC. The same axial slice of each reconstruction at the time point are shown in (d), and the dynamic curve of the thoracic aorta (pointed by orange triangle) are plotted in (e). The MoCoLoR with both MC, well preserves the contour of aorta and corrects the motion induced signal drop, pointed out by orange arrows in (e).
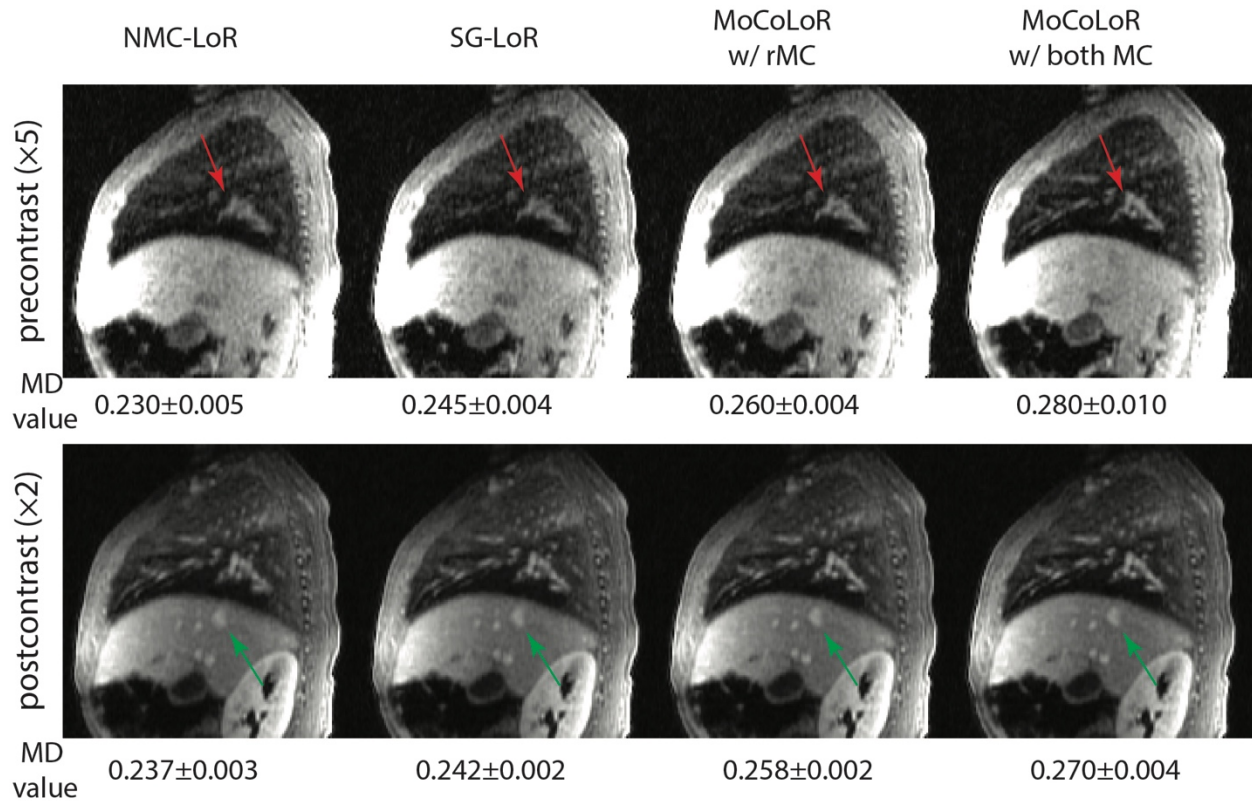
Figure 4.6 Respiratory motion correction comparison on DCE data. Both precontrast (top row) and postcontrast (bottom row) images reconstructed with different strategies are compared, airway and vessels in the lung (red arrows) and vessels in the liver (green arrows) are pointed out.

Sagittal images from both precontrast and postcontrast time points that had no obvious bulk motion are shown in Figure 4.6 to compare the respiratory motion correction performance of different reconstructions. MoCoLoR with respiratory MC and with both MC showed clearer vessels in liver and achieved higher MD of the diaphragm compared to NMC-LoR and SG-LoR strategies in both precontrast and postcontrast images.

4.5. Discussion

In this chapter, I proposed a new reconstruction framework for free breathing low-rank constrained high dimensional MRI reconstruction. By incorporating motion compensation in the reconstruction, the low-rank property of the spatio-temporal matrix is preserved. The proposed reconstruction is applied and evaluated on two different applications under free breathing acquisition situation, one is 3D radial motion resolved lung MRI, the other is a 3D abdominal DCE MRI. The proposed MoCoLoR improved the final reconstruction images compared to the standard low-rank constrained reconstruction in motion resolved lung MRI and soft-gating low-rank constrained reconstruction in DCE MRI.

Compared to motion adaptive low-rank strategies, the proposed method directly extracts motion information from the images instead of searching in the local region, which would be more robust to undersampling artifacts. In addition, most of motion adaptive low-rank strategies consider only translational motion, however, subject motion is usually non-rigid, especially in chest and abdomen. In contrast, MoCoLoR is able to adapt more sophisticated motion models.

In this work, I only used the global low-rank constraint in the reconstruction, but it could be extended to use locally low-rank and multi-scale low-rank constrained reconstruction to further improve the DCE reconstruction[82,93]. In addition, the MoCoLoR can adapt to other low-rank or model based reconstructions, such as T2 shuffling[94], MR Fingerprinting[95], and magnetization preparation shuffling[96], which are also sensitive to subject motion.

One of the challenges in the proposed method is computational complexity, especially for high temporal resolution DCE reconstruction. A compressed representation of low rank model could be used to reduce computation and memory usage, which has been well established in the Extreme MRI method[97]. Similarly, we could also estimate the temporal bases by using coarser resolution then only update spatial components in the full resolution reconstruction, as proposed in the GRASP-pro method[98].

4.6. Conclusion

In this chapter, I proposed a 4D reconstruction method for free breathing MRI by incorporating motion compensation in the low-rank constrained reconstruction model, called MoCoLoR. The proposed method outperforms the standard low-rank constrained reconstruction in both motion resolved lung MRI and abdominal DCE MRI.

Chapter 5 5-minute non-sedated neonatal and pediatric pulmonary UTE based MRI studies

5.1. Introduction

Computed tomography (CT) is the standard and widely used imaging technique for assessing lung anatomy, due to short scan time and high spatial resolution. But CT inevitably requires radiation exposure for subjects, which is particularly concerning for neonatal and pediatric patients[70]. MRI would be an alternative to CT for neonatal and pediatric pulmonary screening, and its flexibility also lends to further tissue characterization and testing of cardiac function.

However, lots of challenges make neonatal and pediatric pulmonary MRI difficult. First of all, low proton density and short T_2* properties largely reduce the parenchymal signal[32]. In addition, compared to CT, MRI requires a much longer scan time, which makes pulmonary MRI vulnerable to subject motion artifacts, especially from respiratory motion[47,49]. Recently, ultrashort echo time (UTE) acquisition schemes combined with motion correction strategies have been applied to pulmonary imaging in adults[34,99]. UTE overcomes the fast signal decay in lung parenchyma and motion correction allows free breathing scans.

As for neonatal and pediatric MRI, it is more challenging, especially under a non-sedated free breathing situation. Unlike adults, it is difficult for children to keep still during a long scan and their respiration rates tend to be higher and less regular. Therefore, a limited scan time and motion robust imaging techniques are required.

Additionally, most of the MRI hardware and software are designed with adult anatomy and physiology in mind, so these factors should also be optimized to suite the unique anatomy and physiology of children[70].

To overcome the above challenges, a 5-minute UTE based MRI strategy is proposed, combining the optimized sequence, specific hardware setups and motion correction strategies. This chapter firstly compared the differences between adult and pediatric studies from the technical aspects, and then the proposed strategy was described in details. Finally, the strategy was applied on several subjects with age range from several-week-old newborns to teenagers with different lung abnormalities.

5.2. Methods

5.2.1. Adult and Neonatal/Pediatric Scan Comparison

A few differences between adults and pediatric scans are summarized in Figure 5.1. Compared to adults, anatomical structures of children and newborns, such as airways, vessels are smaller, which require higher imaging resolution, shown in (a). Similarly, varied size of receiver coils, in (b), are also used to fit different size of subjects. For newborns and children, smaller but denser elements coil arrays, which can provide higher local SNR, are used. As for older subjects, like teenagers or adults, larger element coil arrays are used because of better penetration depth. In addition, higher respiratory rates and different breathing patterns of newborns and children are shown in the comparison according to the respiratory signals derived from different 4 subjects, in (c). Therefore, the standard lung MRI protocols and motion correction strategies for adults might need to be optimized for pediatric or neonatal studies.
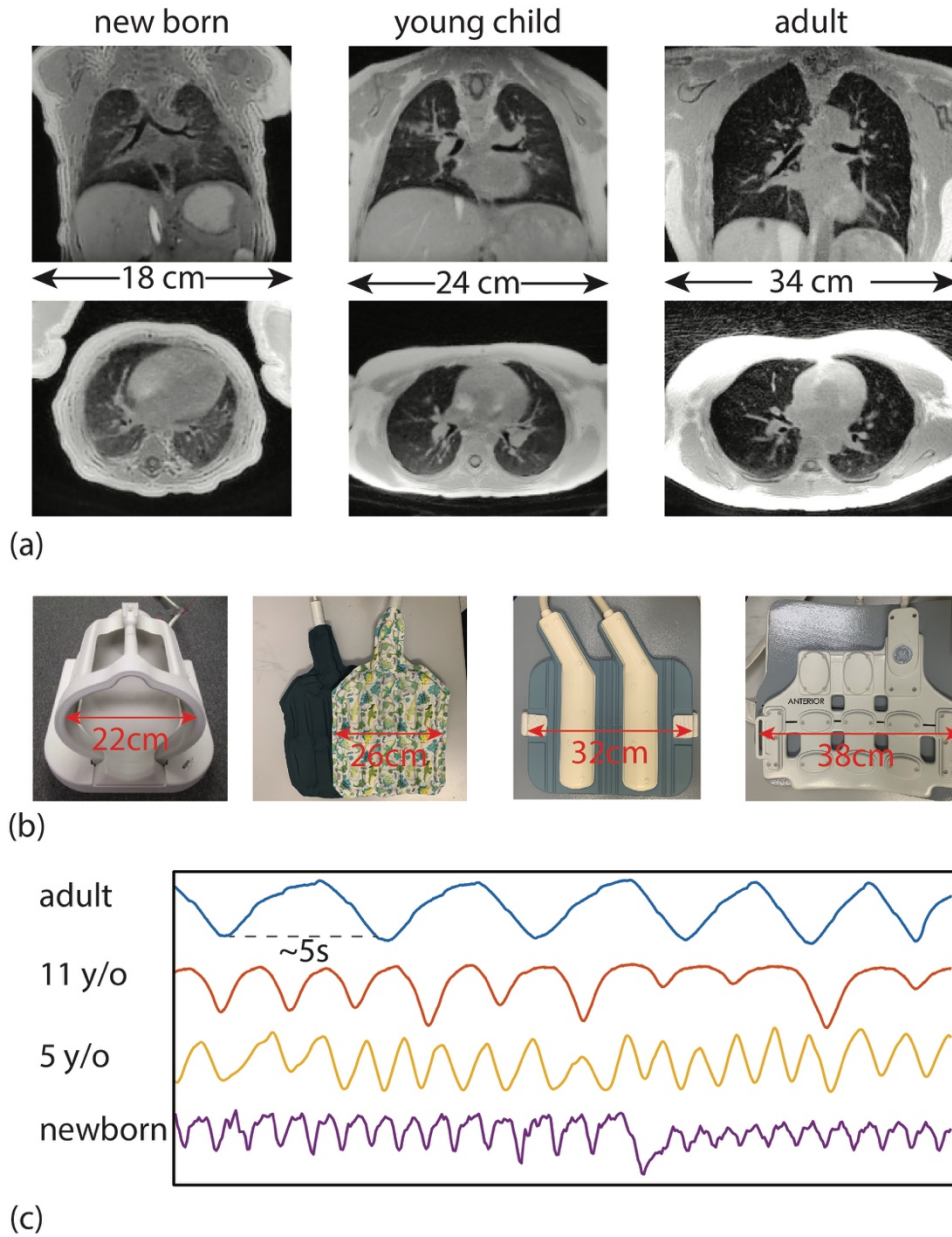
Figure 5.1 Pulmonary UTE scan comparison among newborns, young children, and adults. Slices from both coronal and axial view of three different subjects are shown in (a). Different receive coil arrays are selected for different size subjects, in (b). An example of respiratory waveforms comparison shows different respiratory rates and patterns between a newborn, young child, pre-teenager, and adult, plotted in (c).

5.2.2. Patient Recruitment

Pediatric and neonatal patients were recruited for MRI, with Institutional Review Board approval and parental informed consent.

5.2.3. Data Acquisition

All the studies were run on clinical 3T scanners (GE Healthcare, Waukesha, WI), with different coil arrays depending on size of the subjects. All the patients were scanned under free breathing situation and without sedation. An SNR optimized 3D UTE sequence[36] with golden angle ordering was used for all the scans, TE = 0.08~0.1 ms, TR = 3.1~3.4ms, flip angle = 4° . For newborns and children patients, image resolution was set to 1.1mm isotropic or even higher. All scans acquired ~100,000 radial spokes, with total scan time no more than 5.5 minutes.

For comparison, patients were also scanned with a T1 weighted (T1w) sequence and a T2 weighted (T2w) sequence. The T1w images were acquired with breath holds, TE = 1ms, TR = 2.1ms, $1.1 \times 1.1 \times 4mm^3$ spatial resolution, and total scan time was 12s. Axial PROPELLER fast spin echo (FSE) sequence, and single-short fast spin echo (SSFSE) sequence with $1.4 \times 1.4 \times 4mm^3$ spatial resolution, were used for T2w acquisition. The SSFSE T2w sequence was run with prospective navigator for respiratory gating, the PROPELLER FSE was run without any gating. The T2w sequences usually took 3~4 minutes.

5.2.4. Image Reconstruction and Motion Correction for UTE Acquisition

Two types of reconstructions were used in the clinical studies. One is direct non-uniform fast Fourier transform (NUFFT) reconstruction without motion correction, the other is a motion corrected reconstruction. The data transfer and reconstruction workflow are

illustrated in Figure 5.2 . Direct NUFFT images would be sent back to the scanner

before the end of the exam for quality control. And the motion corrected reconstruction

would be run to generate high quality motion free images, then the images are sent

back to the scanner and picture archiving and communication system (PACS).

For the motion corrected reconstruction, a self-navigator strategy was first applied to

the UTE data for extracting respiratory motion. Self-navigator signals with large drift

caused by bulk motion were rejected before continuing onto the final reconstruction.

Then, the iMoCo reconstruction, introduced in Chapter 3, was used to reconstruct the

3D high SNR motion corrected exhale state images.
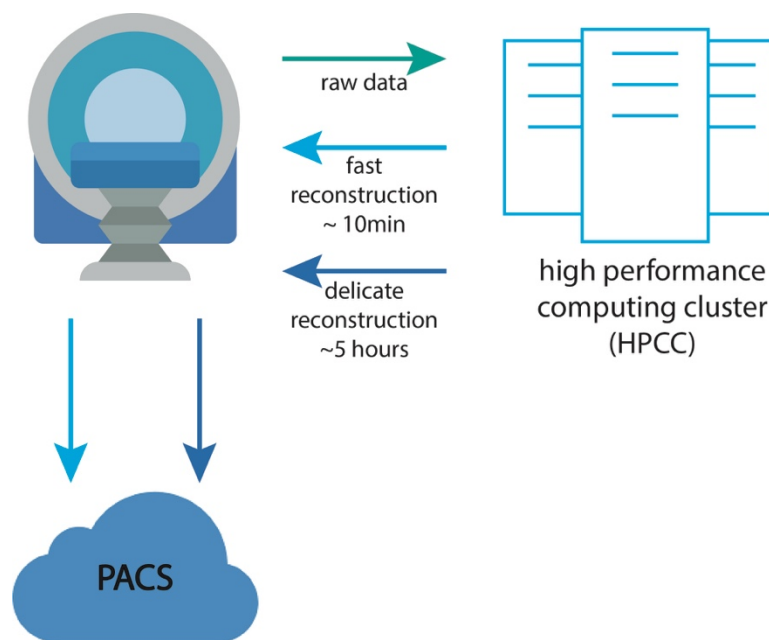
Figure 5.2 Clinical workflow of the UTE reconstruction. After the UTE sequence is completed, raw data would be transferred to a high performance computing cluster (HPCC) and then go through two reconstructions. A fast reconstruction carried out by direct NUFFT algorithm takes total around 10 minutes (including data transfer time) to send images back to the scanner for quality control. A motion corrected reconstruction algorithm would be run for a few hours to get a high quality motion free images, which would be sent back to the scanner then to the PACS after the MRI exam.

5.3. Results

The 5-min free breathing UTE scans from seven subjects, including two newborns, three young children, and two teenagers, are shown in Figure 5.3 . Newborns were scanned with 8-channel head coil array, with less than 1mm isotropic resolution. Young children were scanned with the 32-channel cardiac array or 12-channel shown in Figure 5.1 (b), with 1 to 1.1mm resolution. Teenagers were scanned with 8-channel cardiac array, with 1.1 to 1.4mm resolution. With the optimized sequence, parameters, and motion correction, images show high SNR and clear small structures (vessels and airways) in the lungs.
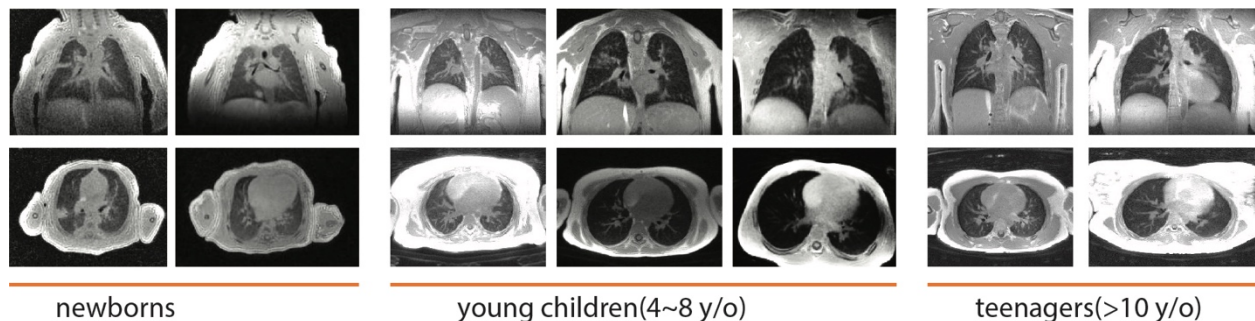
Figure 5.3 Example images from seven pediatric/neonatal studies. For each case, two slices (coronal and axial) from the 3D UTE images are shown, and subjects are sorted to three groups based on their ages.

The comparisons with other sequences are summarized in Figure 5.4. For the SSFSE sequence, the prospective respiratory gating with pencil-beam navigator sequence was used. The UTE images have higher SNR, and less motion artifacts, compared to the GRE and the SSFSE images. The bottom row shows the comparison on a newborn subject. The hypointense area, pointed out by red arrows, can be clearly observed in the UTE images, which is difficult to differentiate on the T1w or T2w images.
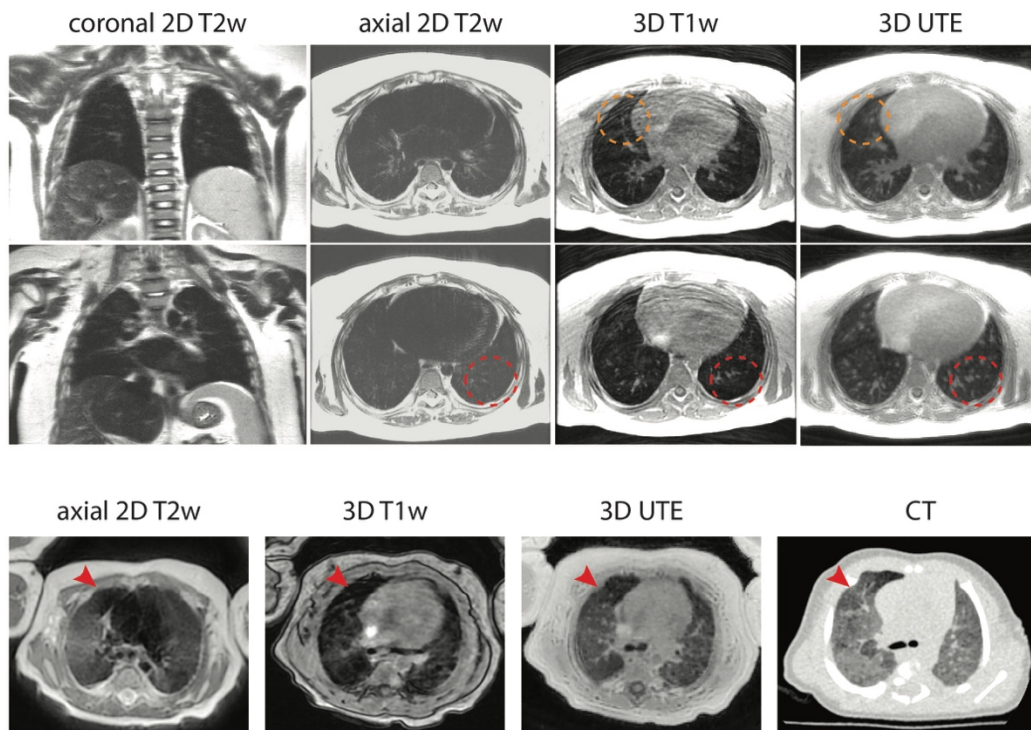
Figure 5.4 MRI sequence images comparison in the lungs. Two SSFSE T2w sequences with navigator based respiratory gating, one axial 3D GRE breath-hold sequence, and the optimized UTE sequence images from one pediatric patient are compared (top two rows). UTE images showed higher SNR (dashed red circle) and were more robust to motion (dashed orange circle) compared to other sequences. In the bottom row, the axial PROPELLER FSE T2w sequence, the axial 3D GRE sequence, the optimized UTE sequence, and a CT scan are compared. The air trapping area (red arrows) shows hypointense in both CT and UTE images.

The UTE images are also compared to standard clinical CT images on three pediatric patients, as shown in Figure 5.5. Images in the first row are from an 8 year-old female with Surfactant Protein C deficiency and lung disease, where a small lung cyst (pointed out by red arrows) is well delineated by the chest CT as well as the 3D UTE. The second row shows the images from a 5 year-old female, in which a small lung nodule could be distinguished from UTE images (surrounded by orange arrows), comparable to CT scan. The third row shows scans from a 4 year-old male with systemic juvenile

idiopathic arthritis who has childhood interstitial lung disease. Ground-glass opacity observed on the CT is also observed in the UTE images, circled by dashed green line.
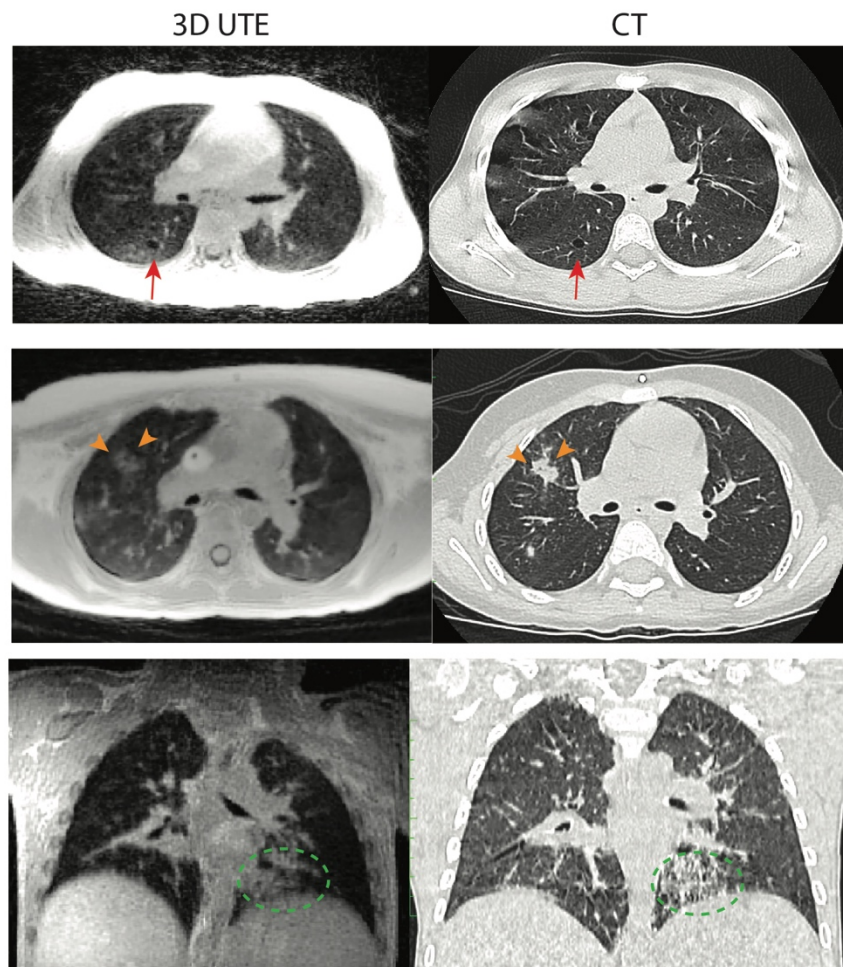
Figure 5.5 UTE and CT comparisons. UTE images of three patients with different abnormalities are compared to their CT scans. The first row images are from a 8 year-old female with Surfactant Protein C deficiency and lung disease, where small lung cyst is pointed out by red arrows. The second row shows a 5 year-old female both UTE and CT images, where a small lung nodule is surrounded by orange arrows. The third row shows scans from 4 year-old male with systemic juvenile idiopathic arthritis who has childhood interstitial lung disease, and ground-glass opacity is circled by dashed green line.

The results of two patients with a 6-month follow-up MRI scan are shown in Figure 5.6. Images of both patients show consistent image quality of the UTE from two different visits, which indicate the reproducibility of the proposed strategy and feasibility for longitudinal studies. For patient 1, septal thickening, pointed out by red arrows, are

consistently observed on the CT and both UTE scans. For patient 2, similar shape and size lung nodule could be observed in CT and the first visit UTE, and the nodule appears to be gone in the 6-month follow-up UTE image.
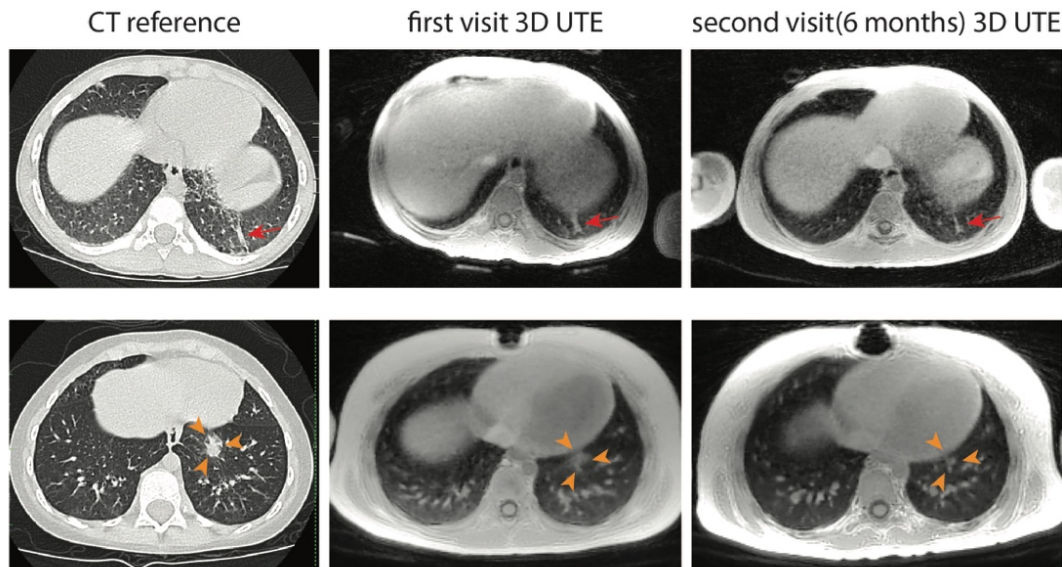
Figure 5.6 Follow-up studies results. Two pediatric patients got their second MRI exam 6 months after their first MRI, and the CT scans happened around their first MRI exams. For patient 1, septal thickening is pointed out by red arrows. For patient 2, a lung nodule region is surrounded by orange arrows.

5.4. Discussion

This chapter discussed the practical considerations in neonatal and pediatric pulmonary MRI studies. Imaging parameters, hardware setups, and motion correction strategies need to be optimized for neonatal and pediatric studies. The proposed 5-min free breathing non-sedated neonatal and pediatric lung UTE is highlighted, and applied to patients varied from newborns to teenagers. The optimized UTE outperforms other sequences and achieves high image quality for distinguishing different lung abnormalities. The results also show the feasibility of 3D UTE for longitudinal follow-up studies.

As mentioned before, the clinical workflow of the lung UTE scan needs data transfer and a long reconstruction time for motion corrected reconstruction. To add the UTE protocol into regular clinical scan, we would put more efforts to shorten the waiting time for the high quality reconstruction. In the future, we would leverage parallel and distributed computing techniques to speed up the reconstruction[100,101], and optimize the iterative algorithm to increase the rate of convergence.

5.5. Conclusion

In this chapter, I proposed an optimized 5-minute non-sedated neonatal and pediatric pulmonary UTE strategy considering practical challenges in pediatric MRI. The optimized UTE strategy outperforms the standard T1w and T2w sequences in lung MRI, and captures abnormalities comparable to chest CT, which has potentials for a broad range of clinical applications in pediatrics and neonatology.

Chapter 6 Optimizing Trajectory Ordering for Fast Radial ultra-short TE (UTE) Acquisition

6.1. Introduction

Ultra-short echo time (UTE) MRI exhibits great promises in imaging short T2* components, such as bone, lung, etc. To achieve the shortest TE, UTE sequences usually start acquisition right after the RF excitation from the center k-space, as mentioned in Chapter 2. Center-out radial acquisition is a widely used trajectory for UTE acquisition. There are a few benefits using radial trajectory, such as simple gradient design, robust to chemical shift and B0 inhomogeneity, etc. One major application of UTE sequence is lung MRI. However, 3D UTE acquisition usually takes a few minutes to achieve high resolution image, which is impractical to acquire under breath-holding condition. To increase the robustness to respiratory motion, random or pseudo-random ordering schemes would be applied to UTE design. One of the widely used pseudo-random ordering schemes is golden angle ordering scheme. The original golden angle scheme is designed for 2D radial trajectory or 3D stack-of-stars trajectory. Recently, a 3D golden angle scheme with two golden ratios is proposed for the 3D koosh ball radial trajectory[79].

Like standard GRE sequences, UTE sequence usually requires a large spoiling gradient before each TR to dephase residual transverse magnetization in the subsequent TRs. However, spoiling gradients[102] prolong the TR and reduce the encoding efficiency. An alternative is to use an RF spoiling strategy by changing the

phase of RF excitation TR by TR, but it still requires a rewinding gradient to refocus the magnetization. Lin[103] proposed to combine randomized RF phases with strong spoiler gradient to achieve a steady state with very slight fluctuation. In short, even with RF spoiling strategy, spoiler gradient and rewinder gradient are still required in the UTE sequence.

To reduce total acquisition time and increase scan efficiency, reducing or even removing spoiler gradient should be considered. Similar idea has been used in zero TE (ZTE) sequences[104]. In ZTE, encoding gradients are adjusted slightly between the successive excitations, and a short waiting time is added to the end of acquisition to serve as a small spoiler gradient. This scheme could be also applied to the UTE acquisition to reduce or remove spoiler gradient. In addition, adding RF spoiling to the sequence might further improve the spoiling effects. Roeloffs et al., investigated the effect of view ordering on spoiler gradient free 2D radial MRI with randomized RF phases[105]. Compared to the schemes with large angle change, such as the golden angle scheme, small incremental angle radial schemes show much lower artifact levels in the final images.

In this chapter, I firstly theoretically demonstrated the gradient spoiling effects of the center-out radial UTE view ordering. Based on that, I proposed a reordered 2D golden angle (r2DGA) scheme to smoothly adjust encoding gradients, but still keep the robustness to respiratory motion. The proposed r2DGA ordering is compared to the sequential and the 3D Golden Angle (3DGA) ordering schemes. I evaluated the proposed method in both phantom and free breathing volunteer lung MRI studies. I also

applied the proposed scheme to breath-holding scan to increase scan efficiency and improve the image quality.

6.2. Theory

6.2.1. Signal Evolution in Spoiler Gradient Free UTE

To help describe the refocusing and dephasing phenomena of the transverse magnetizations in the UTE sequence, the sequence could be decomposed into three components: RF effect, gradient effect, and "other" (including relaxation, diffusion, and exchange etc.). According to the Bloch equations[106,107], the RF effect on the magnetization could be given by:

$$\begin{bmatrix} M_+ \\ M_- \\ M_z \end{bmatrix}^+ = \begin{bmatrix} \cos^2\frac{\alpha}{2} & e^{2i\Phi}\sin^2\frac{\alpha}{2} & -ie^{i\Phi}\sin\alpha \\ e^{-2i\Phi}\sin^2\frac{\alpha}{2} & \cos^2\frac{\alpha}{2} & ie^{-i\Phi}\sin\alpha \\ -\frac{i}{2}e^{-i\Phi}\sin\alpha & \frac{i}{2}e^{i\Phi}\sin\alpha & \cos\alpha \end{bmatrix} \begin{bmatrix} M_+ \\ M_- \\ M_z \end{bmatrix}^- = R\begin{bmatrix} M_+ \\ M_- \\ M_z \end{bmatrix}^- \qquad (6\text{-}1)$$

Where $[M]^-$ and $[M]^+$ are the magnetization before and after the RF pulse, α and Φ are flip angle and phase of the RF pulse. M_+ and M_- , representing transverse magnetization, can be converted to M_x, and M_y via a unitary transformation[108].

  Gradient effects could be written as a diagonal matrix multiplication. Gradients would have a phase accumulation effect on the transverse magnetization.

$$\begin{bmatrix} M_+ \\ M_- \\ M_z \end{bmatrix} = \begin{bmatrix} e^{i\gamma\int Gr\mathrm{dt}} & 0 & 0 \\ 0 & e^{-i\gamma\int Gr\mathrm{dt}} & 0 \\ 0 & 0 & 1 \end{bmatrix} \begin{bmatrix} M_+ \\ M_- \\ M_z \end{bmatrix} = P\begin{bmatrix} M_+ \\ M_- \\ M_z \end{bmatrix} \qquad (6\text{-}2)$$

Here, the G and r represent spatial encoding gradient and spatial location. Similarly, relaxation could be modeled as below,

$$\begin{bmatrix} M_+ \\ M_- \\ M_z \end{bmatrix} = \begin{bmatrix} e^{-\frac{TR}{T_2}} & 0 & 0 \\ 0 & e^{-\frac{TR}{T_2}} & 0 \\ 0 & 0 & -e^{-\frac{TR}{T_1}} \end{bmatrix} \begin{bmatrix} M_+ \\ M_- \\ M_z \end{bmatrix} + \begin{bmatrix} 0 \\ 0 \\ M_0(1-e^{-\frac{TR}{T_1}}) \end{bmatrix} = A \begin{bmatrix} M_+ \\ M_- \\ M_z \end{bmatrix} + B \qquad (6\text{-}3)$$

Here, T_1 and T_2 are the longitude and transverse relaxation time, and TR is the

repetition time. As for diffusion, we simplify the model as a Gaussian diffusion model,

where $\boldsymbol{k}$ is the k-space location and is equal to $\int_0^t \gamma \boldsymbol{G}\, t$.

$$\begin{bmatrix} M_+ \\ M_- \\ M_z \end{bmatrix} = \begin{bmatrix} e^{-D\int k^2 dt} & 0 & 0 \\ 0 & e^{-D\int k^2 dt} & 0 \\ 0 & 0 & 1 \end{bmatrix} \begin{bmatrix} M_+ \\ M_- \\ M_z \end{bmatrix} = D \begin{bmatrix} M_+ \\ M_- \\ M_z \end{bmatrix} \qquad (6\text{-}4)$$

We can now ensemble the above components together.

$$M_{n+1} = D_{n+1}P_{n+1}(A_{n+1}R_{n+1}M_n + B_{n+1}) \qquad (6\text{-}5)$$

In this study, we used a few assumptions for the gradient spoiling analysis. In the

context of the UTE sequence, the flip angle is usually set to be very small, so the

refocused signal only accounts for less than 0.27% of the total signal (for flip angle

smaller than 6°), which could be ignored in the analysis. In addition, chemical exchange

effect is also ignored under small flip angle condition, resulting in the following

simplification of Equation (6-1):

$$\begin{bmatrix} \cos^2\frac{\alpha}{2} & e^{2i\Phi}\sin^2\frac{\alpha}{2} & -ie^{i\Phi}\sin\alpha \\ e^{-2i\Phi}\sin^2\frac{\alpha}{2} & \cos^2\frac{\alpha}{2} & ie^{-i\Phi}\sin\alpha \\ -\frac{i}{2}e^{-i\Phi}\sin\alpha & \frac{i}{2}e^{i\Phi}\sin\alpha & \cos\alpha \end{bmatrix} \approx \begin{bmatrix} 1 & 0 & -ie^{i\Phi}\alpha \\ 0 & 1 & ie^{-i\Phi}\alpha \\ -\frac{i}{2}e^{-i\Phi}\alpha & \frac{i}{2}e^{i\Phi}\alpha & 1 \end{bmatrix} \qquad (6\text{-}6)$$

Plugging (6-2,3,6) into (6-5), we get:

$$\begin{bmatrix} M_+ \\ M_- \end{bmatrix}_{n+1} \approx \begin{bmatrix} e^{i\gamma\int \boldsymbol{G}r dt}e^{-\frac{t}{T_2}} & 0 \\ 0 & e^{-i\gamma\int \boldsymbol{G}r dt}e^{-\frac{t}{T_2}} \end{bmatrix} e^{-D\int k^2 dt} \begin{bmatrix} -ie^{i\Phi}\alpha M_z \\ ie^{-i\Phi}\alpha M_z \end{bmatrix}_n$$

$$+ \begin{bmatrix} e^{i\gamma\int \boldsymbol{G}r dt}e^{-\frac{t}{T_2}} & 0 \\ 0 & e^{-i\gamma\int \boldsymbol{G}r dt}e^{-\frac{t}{T_2}} \end{bmatrix} e^{-D\int (k_n+k)^2 dt} \begin{bmatrix} M_+ \\ M_- \end{bmatrix}_n \qquad (6\text{-}7)$$

M_{n+1} can be split to two parts, the excitation magnetization term (first row, desired signal) , and the previous transverse magnetization term (second row, undesired residual signal), both terms share the same phase accumulation and T2 decay in each TR, but with different diffusion b-values. Diffusion effects on the previous transverse magnetizations depend on the previous accumulated phases as well as the gradient in the current TR. k_n represents the accumulated phase after n TRs, given by:

$$k_n = \sum_{i=0}^{n} \int_{TR_i}^{TR_{i+1}} \gamma G(t) dt \tag{6-8}$$

According to Equation (6-7), decay of the previous transverse magnetization depends on the k_n sequence. To suppress the previous residual transverse magnetizations, we need to maximize $|k_n|$ in (6-8) in the following TRs, which would induce a strong dephasing effect as well as a large diffusion effect. Therefore, the ordering design plays an important role in spoiler gradient free UTE.

A 2D center-out radial sequence with 20 radial spokes are simulated to show how radial ordering schemes affect the spoiler gradient free sequence. Two ordering schemes, sequential and golden angle ordering, are compared in Figure 6.1. Trajectory orderings are color-encoded, plotted in (a), and the respective pulse sequence sketches are plotted in (b). The accumulated gradient spoiling moments evolutions of each excitation, calculated from (6-8), are plotted in (c). The sequential ordering scheme has a smooth change of readout direction, which would increase the accumulated gradient spoiling moments as well as the diffusion attenuation effect. In contrast, due to large readout direction change, the golden angle scheme would refocus residual transverse signal in the following excitations causing signal contamination. In addition, larger accumulated gradient spoiling moments of the sequential ordering scheme would

associate with stronger diffusion effects, which would further attenuate the residual

transverse signals, shown in (d).
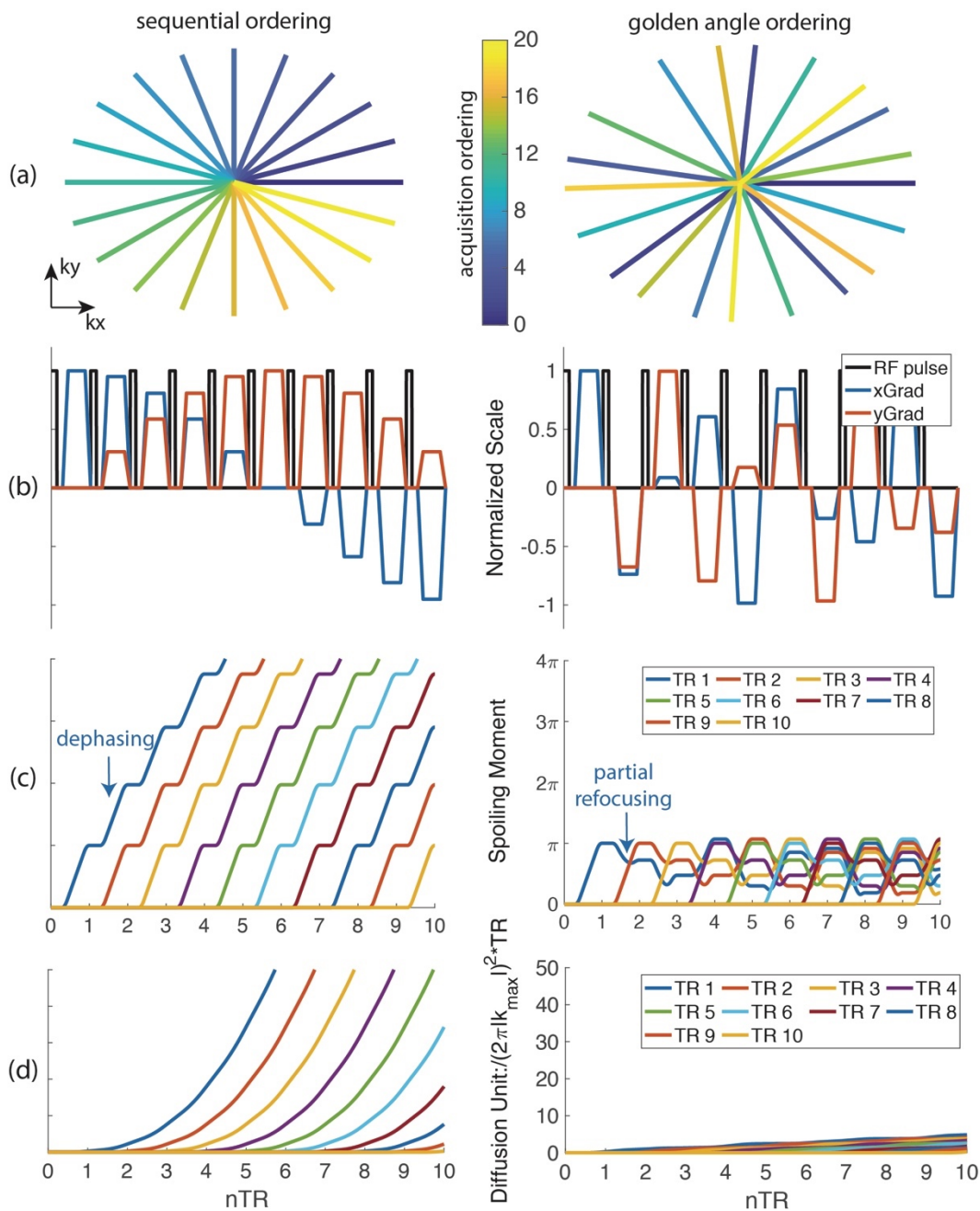
Figure 6.1 Effect of 2D radial ordering on gradient spoiling. Sequential and golden angle ordering schemes with 20 spokes are plotted in (a). The corresponding sequence sketches are shown in (b). Spoiling moments and diffusion effects induced by the encoding gradients of two different ordering schemes are plotted in (c) and (d).

A simple digital simulation on a uniform circle phantom are shown in Figure 6.2. The same acquisition schemes are used with Figure 6.1 . The 6th TR is selected for comparison, the accumulated gradient spoiling moments are plotted in (b), a zoomed-in of Figure 6.1 (c). The observed signals in 6th TR of simulation are plotted in (c), and the signals are decomposed to signals from different excitations according to (b). With the sequential scheme, residual signals are suppressed, the observed signal is well-aligned with the desired signal. However, with the golden angle scheme, the observed signal is largely corrupted by refocused residual signal.

Similarly, for the 3D UTE acquisition, smoothly changing radial readout directions can reduce the need for a spoiler gradient.
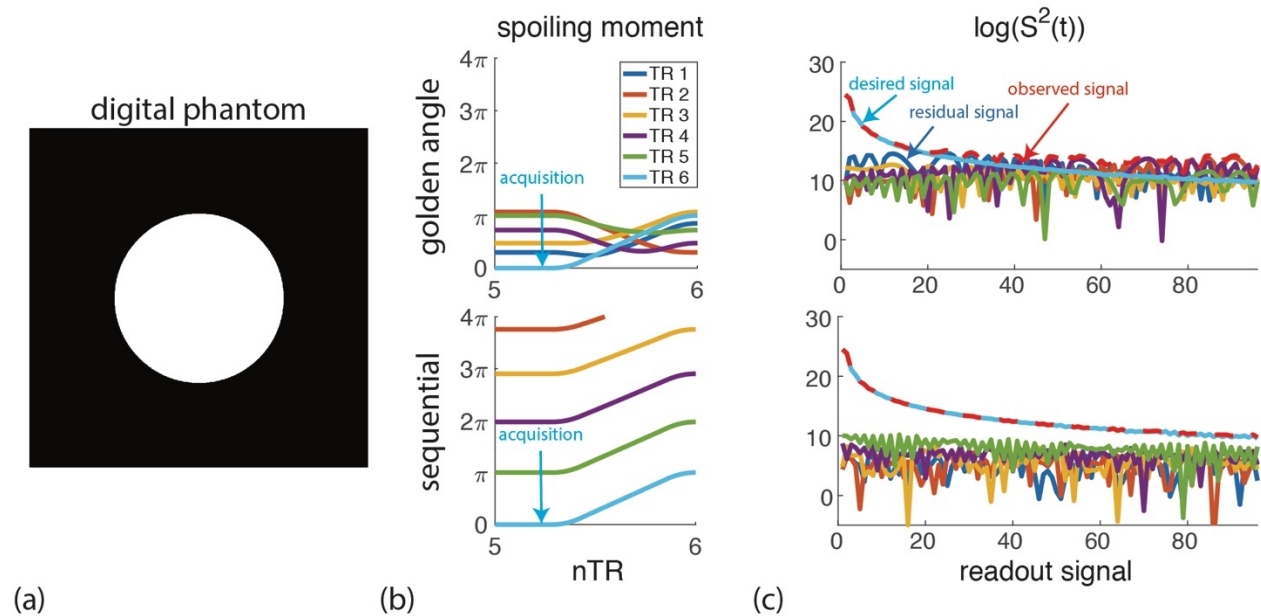
Figure 6.2 Simulation of gradient spoiling effect with different ordering schemes. The digital phantom, (a), is used for simulation. Spoiling moments of all excitations in 6th TR are shown in (b). Signal acquired from 6th TR are plotted in (c). Dashed red lines show the acquired signal, and signal from the current excitation and residual transverse signals are plotted in the same colors as in (b).

6.2.2. View Ordering Design for 3D UTE Acquisition

To maximize the gradient spoiling moments of the spoiler free UTE sequence, the encoding gradients should be smoothly changed. Sequential ordering, similar to the 2D example above, is one of the candidates fulfilling the requirement. However, sequential ordering is not robust to subject motion. In contrast, golden angle ordering is more robust to motion than sequential ordering. As for 3D acquisitions, to balance the robustness to motion and smoothness of the readout direction changes, I proposed to combine a through-plane (z-axis) continuous acquisition with an in-plane golden angle acquisition scheme, and named it reordered 2D golden angle scheme.

Three different view ordering schemes, sequential ordering, the proposed reordered 2D golden angle (r2DGA), and 3D golden angle (3DGA) schemes, are used in this work.

1000 continuously acquired spokes out of the total 100,000 spokes with three ordering schemes are plotted in Figure 6.3 (a), and the pseudo-code to generate the ordering schemes are listed in (b). Average accumulated spoiling moments of transverse magnetization in the following TRs are used to evaluate the accumulated spoiling effects, as plotted in (c). Similar to the 2D example, the 3DGA scheme generates a small accumulated spoiling moments which might not be enough to dephase residual transverse magnetizations without spoiler gradients. In contrast, the sequential and r2DGA schemes generate much larger spoiling moments to dephase the residual signals.

sequntial ordering	reordered 2DGA	3DGA
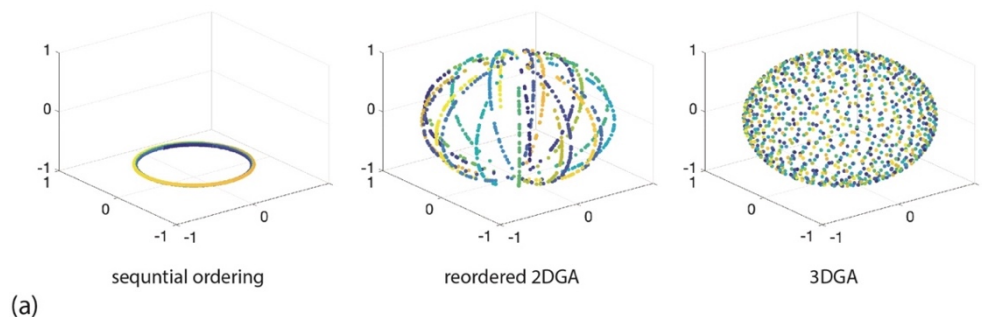
(a)

Sequential ordering scheme	Reordered 2D golden angle(r2DGA) scheme	3D golden angle(3DGA) scheme
Define N(number of radial spokes);	Define N, x, y, z from sequential trajectory, $\eta = 0.618$, N_g number of groups, G group number;	Define $N, g_1 = 0.465, g_2 = 0.682$;
$for\ i = 1:N$ $z = \dfrac{2i-1}{N}$ $x = asin(z) * \cos\left(\sqrt{2N\pi i}\right)$ $y = asin(z) * \sin\left(\sqrt{2N\pi i}\right)$ end	$for\ i = 1:N$ $\theta_i = \arctan(x[i]/y[i])$ $G[i] = \underset{\theta_k = 2\pi\eta k,\ k \in N_g}{argmax} \cos(\theta_i - \theta_k)$ end $for\ k = 1:N_g$ if k is odd, $\mathbf{G_k}$ sorted *by z in descending order*; if k is even, $\mathbf{G_k}$ sorted *by z in ascending order*. end ($\mathbf{G_k}$ is k^{th} group of spokes)	$for\ i = 1:N$ $z = 2 * mod(ig_1, 1) - 1$ $x = asin(z) * \cos(2\pi g_2 i)$ $y = asin(z) * \sin(2\pi g_2 i)$ end

(b)
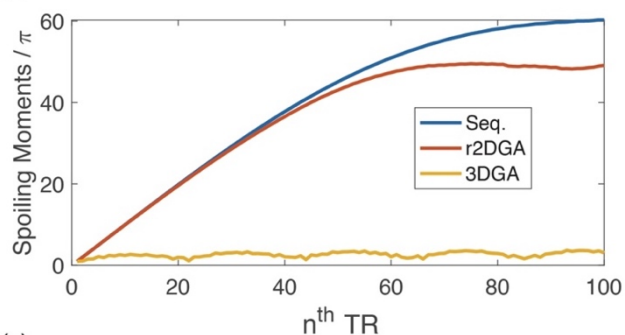
(c)

Figure 6.3 3D trajectory ordering schemes and spoiling effect analysis. 1000 continuous spokes are plotted in (a), sequential acquisition only covers a small part of k-space, however, r2DGA and 3DGA schemes sample the k-space more uniformly. Pseudo-code to generate acquisition trajectory schemes are summarized in (b). The average accumulated spoiling moments created by different schemes in the subsequent TRs are plotted in (c), the sequential and the r2DGA schemes creates much larger spoiling moments than the 3DGA in the following TRs.

(a)

(b)
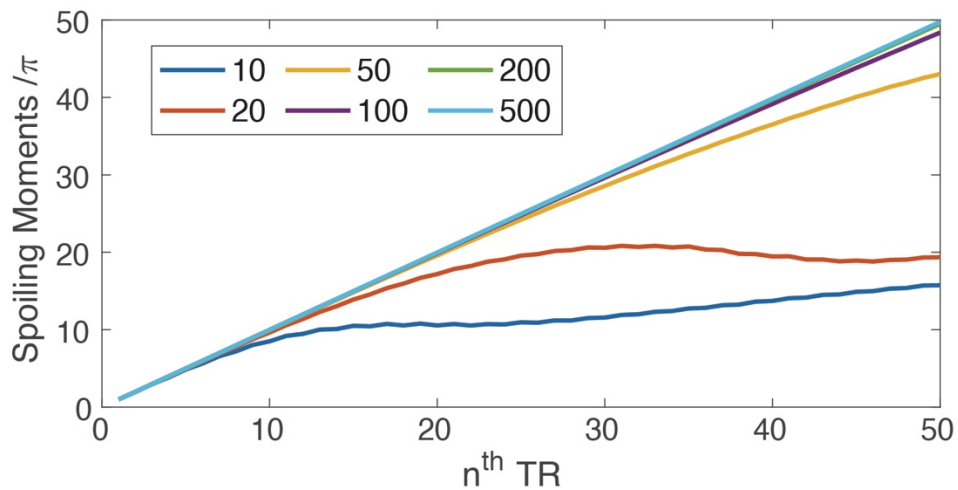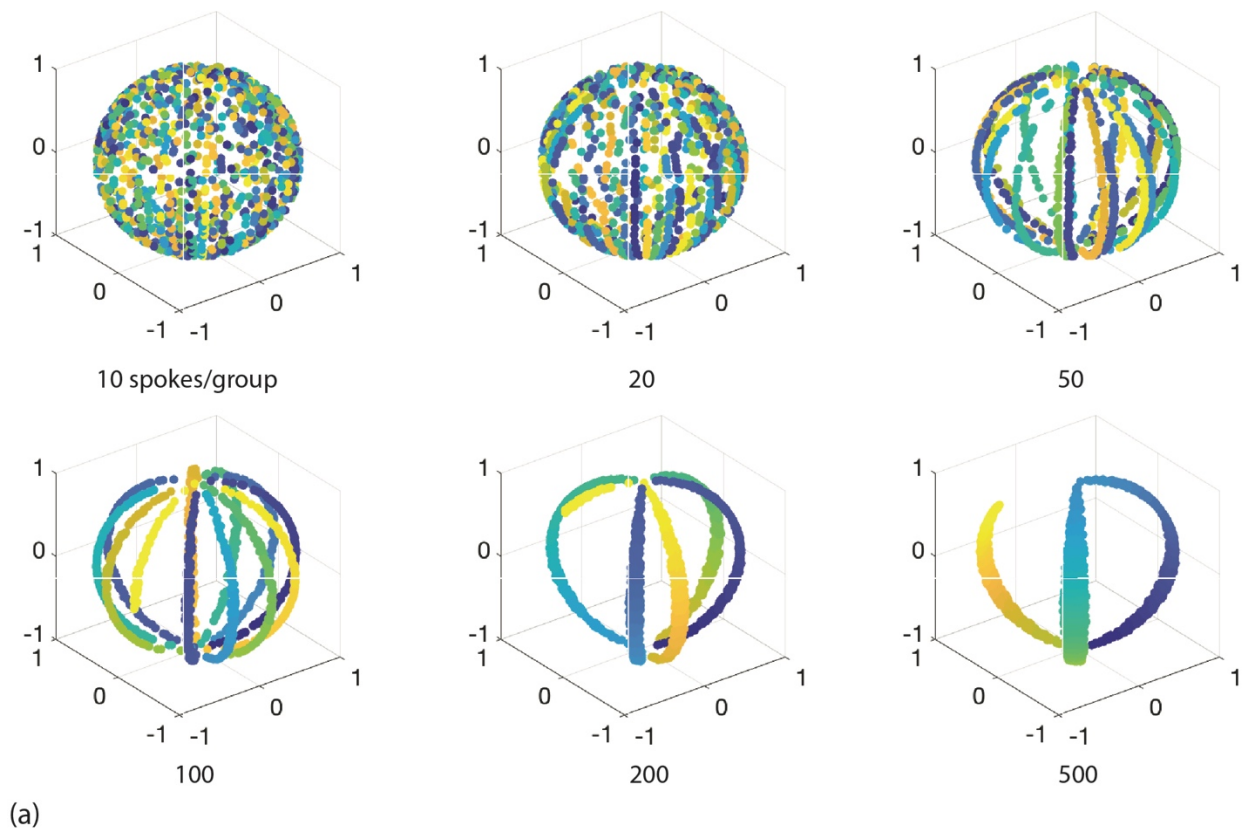
Figure 6.4 Number of spokes per group in the r2DGA ordering design. 1000 spokes distributions with different number of spokes per group are plotted in (a), and the accumulated spoiling moments are plotted in (b) accordingly. As the number of spokes per group increases, the accumulated spoiling moment increases, at the expense of less uniform spatial sampling over time.

There is one tunable parameter in the r2DGA design algorithm, the number of spokes per group. 1000 continuous spokes with 6 different number of spokes per group are plotted in Figure 4, (a), and the average accumulated spoiling moments are plotted in (b) accordingly. As the number of spokes per group increases, the average accumulated spoiling moments also increase in the later TRs. Meanwhile, sampling pattern with more number of spokes per group are less uniformly distributed, and thus are also more sensitive to motion.

6.3. Methods

6.3.1. MRI Experiments

All experiments were run on a 3T MR scanner (General Electric, Milwaukee, WI) with the 8-channel phased array cardiac coils. An optimized variable density readout center-out radial UTE sequence was used in all the experiments. The 3DGA ordering sequence with constant 4π (4 units) spoiler gradient with the same FOV, spatial resolution, and sampling bandwidth as other scans is acquired as the reference for both phantom and *in vivo* studies.

6.3.2. Phantom Study

A multi-purpose phantom is used in all the experiments. Data were acquired with 1mm isotropic resolution, image matrix size 200 × 200 × 200, TE=100μs, readout bandwidth=125kHz, TR=2.2ms. The UTE sequences with sequential, 3DGA and proposed r2DGA ordering schemes acquired without spoiler gradient are compared. All

three sequences are acquired with 100,000 spokes. Phantom is also scanned with different scales spoiler gradients with r2DGA trajectory ordering, with shortest TR (2.2ms~3.1ms). To fairly compare the acquisition ordering schemes, direct NUFFT with density compensation followed by the coil combination reconstruction are used for the phantom studies. Apparent SNR (aSNR) of the reconstructed images are measured to evaluate the performance of different ordering schemes.

6.3.3. Human Study

All the volunteer studies conducted were approved by UCSF Institutional Review Board (IRB). Two types of acquisitions are designed for human studies, free breathing scan and breath-holding scan.

For free breathing scans, data were acquired with 1.25mm isotropic spatial resolution, image matrix size 256 × 256 × 256, TE=70µs, 100,000 spokes, with around 2-fold undersampling. Motion corrected image was reconstructed with the self-navigated soft-gating reconstruction. The TRs depended on the moments of the spoiler gradient, in the range of 1.9 and 3.7ms, and the flip angles were set to 4~6° accordingly to target Ernst angle with 1s T1.

For breath-holding scans, data were acquired with 2mm isotropic spatial resolution, image matrix size reduced to 160 × 160 × 160, TE=70µs, and number of spokes were calculated to fit the whole sequence in 15 seconds. 3DGA scheme with 4 units spoiler gradient acquired ~6000 spokes, and r2DGA schemes without spoiler gradient acquired ~10000 spokes in 15 seconds. Because little respiratory motion is assumed in the

breath-holding scans, direct NUFFT with density compensation followed by coil combination reconstruction are used without any motion correction.

6.4. Results

6.4.1. Phantom Study

Single axial slices at the same location from 3DGA with 4 units spoiler gradient, 3DGA and r2DGA without spoiler gradient, are shown in Figure 6.5 . Compared to 3DGA without spoiler gradient, the r2DGA ordering scheme largely suppresses the unwanted residual transverse signals and has a much lower root mean square (RMS) of the difference with reference.

    However, there are still slight artifacts shown on the image without spoiler gradient. Therefore, spoiler gradients with varied scales were added to the sequence with the r2DGA scheme to investigate the improvement contributed from the extra spoiler gradients. Figure 6.6 shows 5 datasets with different scales of spoiler gradients. One axial slice of each data are plotted in (a), and line profiles across the comb structure (red dashed line) are plotted in (b). By adding a small spoiler gradient, the aSNR largely increases. As the moment of spoiler gradient further increases, the aSNRs are slightly elevated. However, the scan time largely increases due to the longer TR. From the line profiles comparison, it could be observed that by adding a small spoiler gradient the comb structure becomes sharper and the background becomes flatter compared to the acquisition without a spoiler gradient.

| 3DGA reference | 3DGA w/o spoiler | r2DGA w/o spoiler |
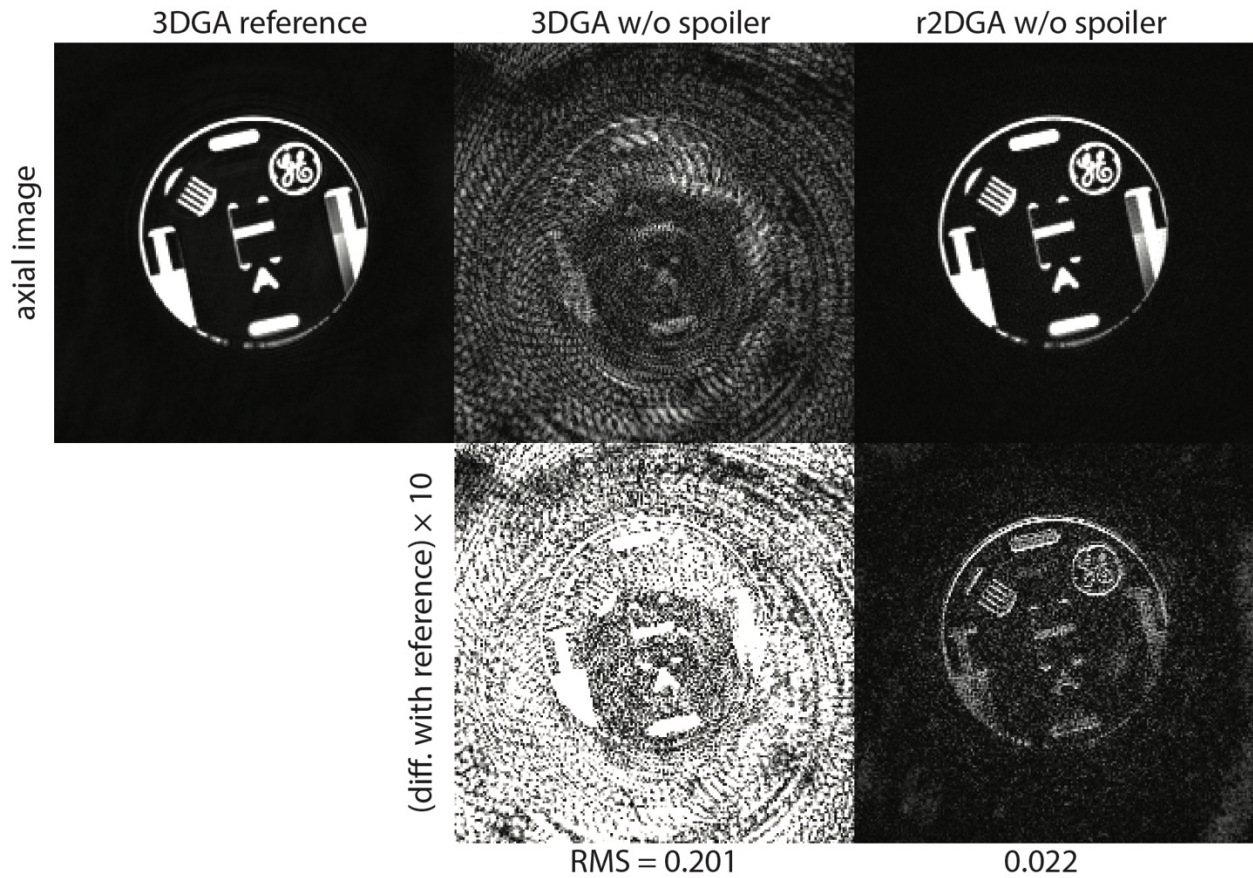
Figure 6.5 Phantom study with different ordering schemes. Images acquired with the reference sequence, the 3DGA without spoiler gradient, and the r2DGA without spoiler gradient are compared. Compared to reference scan, the image acquired with the r2DGA ordering scheme has very light noise-like artifacts, 3DGA without spoiler gradient shows strong artifacts compared to the other two, and the root mean square of difference with reference much higher.
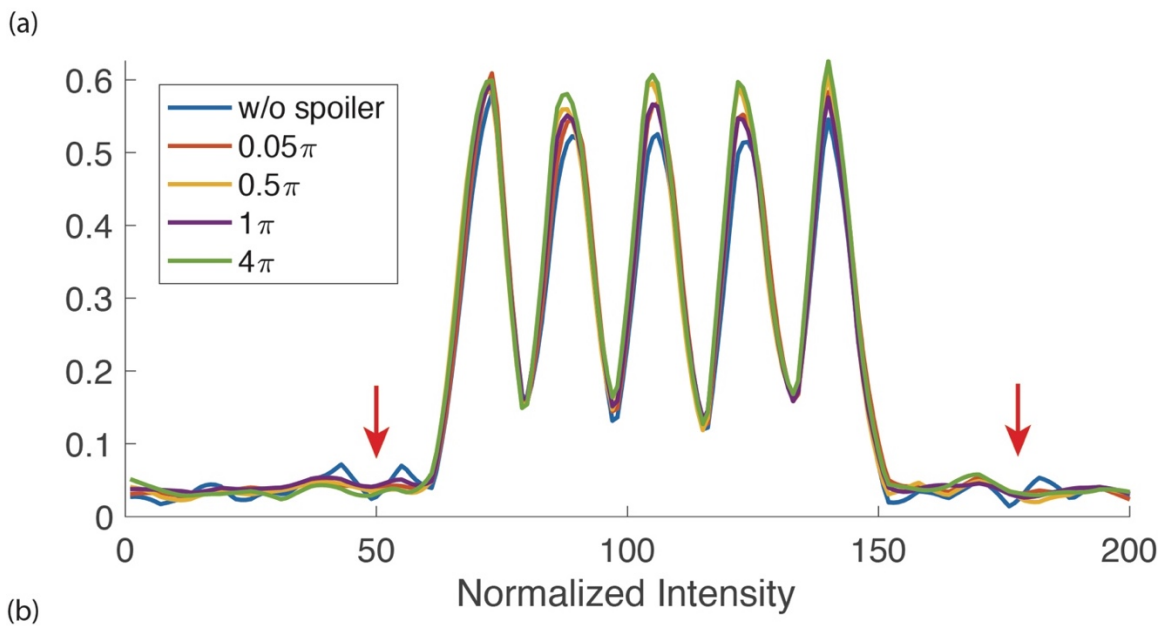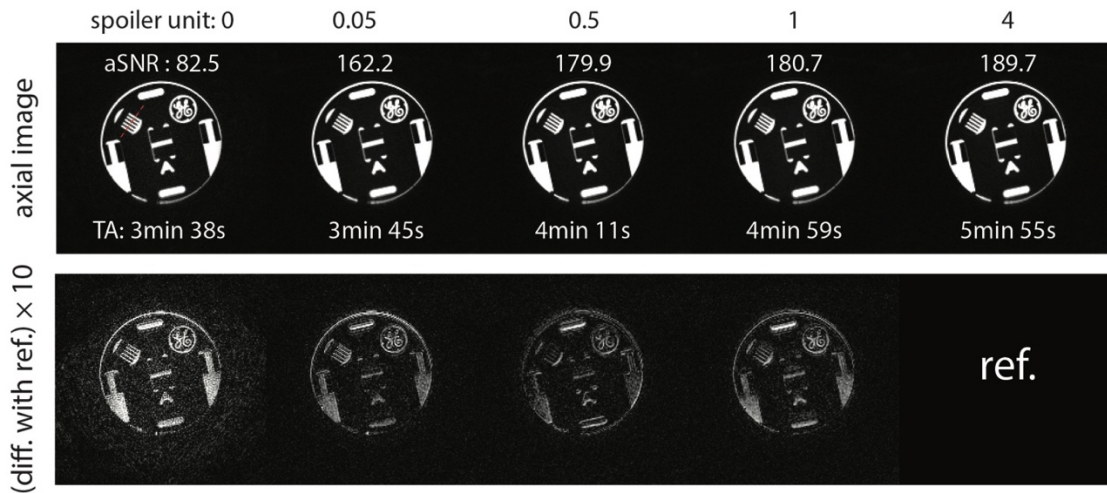
Figure 6.6 Phantom study with different spoiler gradients using the r2DGA scheme. In (a), spoiler gradients with different spoiling moments are compared, as spoiling moment scale increases, scan time and apparent SNR increases. The line profiles (red dashed line plotted in (a)) are compared in (b). Without a spoiler gradient, small fluctuating signals (pointed out by red arrows) show up in the background.

6.4.2. Volunteer Study

Images acquired with the 3DGA ordering with 4 units spoiler gradient (reference), the r2DGA without spoiler gradient, and the r2DGA with a 1 unit spoiler gradient are shown in Figure 6.7.

GA w/ 4 unit spoiler
scan time: 5min 5s

GA w/o spoiler
scan time: 3min 2s

GA w/ 1unit spoiler
scan time: 4min 12s

(a)

(b)
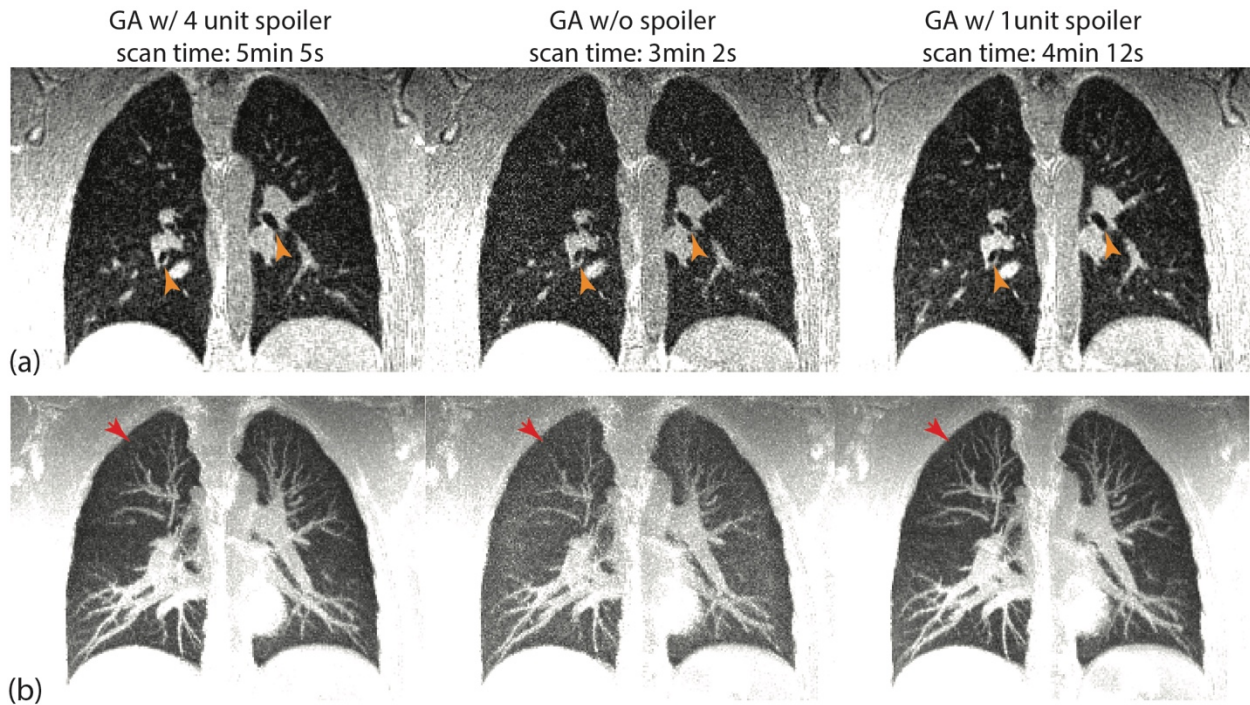
Figure 6.7 Free-breathing volunteer study. One coronal slice of 3D volume with different ordering schemes are shown in (a), the image acquired by the r2DGA without spoiler is slightly noisier than the reference scan, but reduces the scan time by 40%. Maximum intensity projection (MIP) of 15 coronal slices from each volume are plotted in (b), the r2DGA with small spoiling gradient delineates most small vessels and has a relatively shorter scan time compared to the reference scan.

The r2DGA acquisition without the spoiler gradient can save 40% scan time compare to reference scan. However, slightly noise-like artifacts show up in the images with the spoiler free acquisition, which make small airways difficult to distinguish from parenchyma tissue (pointed out by orange arrows). By adding a 1 unit spoiler gradient, these artifacts are largely suppressed, and image quality is comparable to reference scan. And the scan time is still 20% shorter than the reference. Maximum intensity projection (MIP) maps of 15 coronal slices from each acquisition are shown in (b), r2DGA with 1 unit spoiler gradient largely reduce the artifacts compared to without spoiler gradient acquisition and preserve more fine structures, pointed out by red arrows.
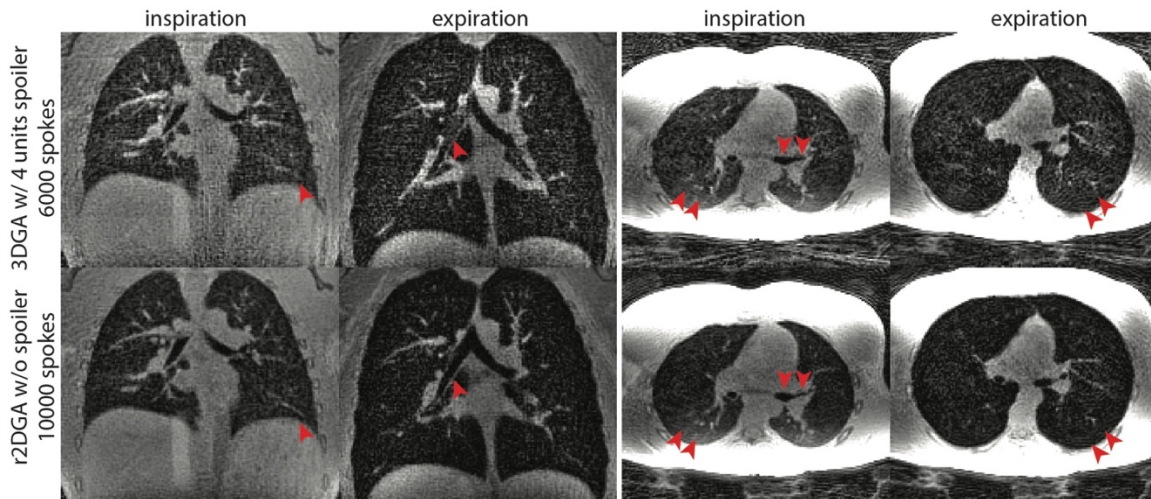
Figure 6.8 Breath-holding volunteer study. Two acquisition schemes, 3DGA with 4 units spoiler gradient and r2DGA without spoiler gradient, were used to acquire breath-holding images in 15 seconds. Both inspiration and expiration breath-holding situations are compared. The r2DGA shows less streaking artifacts and clearer lung structures than 3DGA scheme because of higher scan efficiency.

It is more valuable to shorten the TR and increase total number of readouts for breath-holding scans. Figure 6.8 shows a 15 seconds breath-holding acquisition with two different acquisition schemes. With 4 units spoiler gradient, the 3DGA sequence acquires ~6000 spokes in 15 seconds, and has approximately 12-fold undersampling. In contrast, the r2DGA acquisition can fit ~10000 spokes within the same duration, reducing the undersampling factor to 7.2. Both the coronal and axial slices from the same subject under different types of breath-holding, inspiration and expiration are compared. Much less streaking artifacts could be seen with the r2DGA spoiler free acquisition compared to with the 3DGA. And the small anatomical structures, such as vessels, parenchyma, and airways (pointed out by red arrows) are also better delineated with the r2DGA spoiler free acquisition.

6.5. Discussion

In this chapter, I analyzed how the 3D center-out radial trajectory ordering affects the transverse magnetization spoiling, and proposed a new reordering scheme named reordered 2D Golden Angle scheme to reduce or remove the need of spoiler gradient in conventional UTE sequence. Compared to the 3D golden angle scheme, the r2DGA changes encoding gradient much more smoothly, which would induce larger spoiling moments and diffusion effects to suppress the residual transverse magnetization. In addition, the r2DGA scheme still samples randomly in two dimensions to keep the robustness to subject motion. Number of spokes per group is a tunable parameter in the r2DGA design algorithm. By reducing the number of spokes per group, sampling pattern would be more uniform in the k-space, however, the induced spoiling moments and diffusion effects would decrease. Empirically, the number of spokes per group is set to 50 targeting at around 100ms per group, and the number of groups is total spokes divided by number of spokes per group.

In addition to increasing encoding efficiency, there are a few other benefits by using the r2DGA spoiler gradient free sequence. Firstly, eddy current effects might be reduced by reducing or removing the large spoiling gradients. Secondly, the acoustic noise and associated vibrations would also be reduced without the large spoiler gradient, since rapid changes of gradient pulses create the majority of acoustic noise in MRI.

I did not quantify or quantitatively analyze the residual transverse magnetizations evolution in this work, since they largely depend on the subject structure as well as T1, T2 relaxation property of the subject. In essence, the accumulated spoiling moments of

the transverse magnetization could be treated as sampling the k-space at very high frequency. We assume signal intensity decreases as the spoiling moment increases (high frequency components in the k-space), regardless of the diffusion effect. If the subject has repeated high frequency features, without large spoiler gradients, the residual transverse magnetizations might still corrupt the signals in the following TRs.

In this chapter, the proposed ordering design is one of the options for free breathing acquisition. By revisiting the gradient spoiling analysis, the ordering design could be formulated as a convex optimization problem, with certain sampling criteria, such as uniformity of the sampling scheme. However, as the number of radial spokes increases, the computational complexity of the problem grows quickly. Group-wise optimization may help reduce the computational complexity.

Besides the center-out radial trajectory demonstrated, cones, radial cones, and FLORET[109] trajectories can be used for UTE acquisition. Because of their curvature in k-space compared to the center-out radial trajectory, without spoiler gradient the transverse magnetization might be refocused by the following encoding gradient with those trajectories.

6.6. Conclusion

In this chapter, I analyzed how ordering schemes affect transverse magnetization spoiling, and proposed a new ordering scheme, named reordered 2D golden angle for 3D UTE sequence to reduce the need of spoiler gradient and increase the encoding efficiency. We evaluated the ordering scheme by comparing to 3D golden angle and sequential ordering on both phantom and volunteer study. I applied the proposed

ordering on both free breathing and breath-holding lung UTE scans, which largely

shortened the free breathing UTE scan with high SNR and improved image quality of

the breath-holding scan.

Chapter 7 Summary and Future Research Directions

7.1. Summary of Dissertation

This dissertation presents novel techniques developed for lung MRI and their improvements in clinical pediatric studies. For free breathing scans, one widely used motion correction strategy is called gating. However, gating would largely reduce the scan efficiency due to throwing away the motion corrupted data.

The proposed iMoCo UTE could reconstruct motion free lung images with very high efficiency by incorporating motion compensation model in the reconstruction. In addition, a spatial total generalized variation (TGV) constraint was added to the reconstruction further suppressing the artifacts caused by undersampling and residual motion.

However, iMoCo reconstruction would only generate single motion state 3D images. To reconstruct images of different motion states or images with dynamics, the iMoCo model is extended to a 4D reconstruction with a spatio-temporal low-rank constraint. By compensating the motion spatially, the low-rank property of the spatio-temporal matrix is preserved. The proposed method was demonstrated in *in vivo* studies for both motion resolved reconstruction and dynamic contrast-enhanced reconstruction and showed improvements compared to traditional motion correction methods.

The iMoCo UTE then was evaluated clinically for pediatric and neonatal lung MRI studies. Besides reconstruction and motion correction, MRI receiver coils and scan

parameters were optimized for young children and newborns. The results show that iMoCo UTE can reconstruct high SNR motion free lung images, and outperforms standard T1w and T2w sequences. Most importantly, most of the abnormalities observed on CT scans could be also found with iMoCo UTE images, which indicates it is promising to use free breathing UTE acquisition for pediatric lung screening.

In revisiting the UTE sequence, I observed the large spoiler gradient before each TR costs up to 40% of the TR, which decreases the encoding efficiency of the UTE sequence. The proposed reordered 2D golden angle ordering scheme reduces the need of the spoiler gradients by leveraging the spoiling effect of the readout gradient. When it was applied to free breathing lung imaging, total scan time could be shortened by 40% with comparable image quality. When it was applied to breath-holding scans, more readouts could fit in a single breath hold to reduce undersampling artifacts.

7.2. Future Research Directions

This section summarizes some new directions related to this dissertation and speculates on their applications.

7.2.1. Model Based Reconstruction with Motion Compensation

In this dissertation, I made many efforts to model body motion and incorporate them in the existing reconstruction frameworks. Similarly, motion compensation could be also applied to other model based reconstructions. Recently, lots of multi-contrast imaging or parameter mapping techniques are developed, such as MR Fingerprinting[95], T2

shuffling[94], and magnetization preparation shuffling[96] techniques. Those methods show great results in brain or knee applications, but none of them reports applications in the body. One major concern is the subject motion. Similar to the low-rank constrained reconstruction, spatial misalignment might also lead to failure of the model based reconstructions. By compensating the motion during the reconstruction, the assumed model would be better preserved, which may improve the final images or quantitative mapping. Since most of the model based reconstructions use the similar reconstruction formulation as the low-rank constrained reconstruction[110], the MoCoLoR reconstruction should be easily extended to other model based reconstructions.

7.2.2. ZTE Lung MRI

Besides UTE, the zero echo time (ZTE) sequence is also a good candidate for lung MRI[111–113]. In addition, compared to UTE, ZTE has much less acoustic noise, which might make patients, especially pediatric patients, more comfortable.

However, ZTE also has some limitations. Flip angle and allowed maximum receiver bandwidth are limited, which might lead to low SNR of the ZTE images. Using better hardware setups, such as high SNR receiver coil array, may compensate that drawback.

Standard ZTE sequence usually provides proton density or modest T1 contrast. By adding magnetization preparation pulses, ZTE might also provide other contrast images[114]. As for motion, some methods have been proposed to adapt ZTE acquisition to free breathing lung imaging[115]. Advanced reconstruction and motion correction strategies could be also applied to ZTE to improve the SNR and shorten the scan time.

7.2.3. Low Field Lung MRI

Another opportunity for lung MRI is imaging the lung in low field strength MR systems[116–119]. At low field, T2* of lung tissue is expected to be much longer than in the higher field. With a shorter T1 and longer T2*, there is more flexibility for pulse sequence design for lung MRI. In addition, researchers have reported oxygen enhanced (OE) lung MRI is a promising method for imaging certain lung diseases, such as asthma, chronic obstructive pulmonary disease (COPD), etc[120–123]. At lower field strengths, T1 is more sensitive to oxygen level change, which may further benefit the OE lung MRI.

7.2.4. Low Dose CT Lung Imaging

This dissertation mostly focuses on how to reduce both scan time as well as motion effects in lung MRI. However, as mentioned before, the acquisition time of 3D lung MRI is still much longer than the CT. By using low dose CT, which has been widely used for lung cancer screening[124–127], both radiation exposure and subject motion problems could be solved. Recently, deep learning (DL) was introduced to different medical imaging research areas. By using DL methods to reconstruct CT images[128–131] and denoise images after reconstruction[132–134], the low dose CT could achieve comparable image quality as the standard CT, which is also very promising for pediatric lung imaging.

References

1. El-Dahshan EAS, Mohsen HM, Revett K, Salem ABM. Computer-aided diagnosis of human brain tumor through MRI: A survey and a new algorithm. *Expert Syst Appl*. 2014;41(11):5526-5545. doi:10.1016/j.eswa.2014.01.021

2. Wibmer A, Hricak H, Gondo T, et al. Haralick texture analysis of prostate MRI: utility for differentiating non-cancerous prostate from prostate cancer and differentiating prostate cancers with different Gleason scores. *Eur Radiol*. 2015;25(10):2840-2850. doi:10.1007/s00330-015-3701-8

3. Jack CR, Petersen RC, Xu YC, et al. Prediction of AD with MRI-based hippocampal volume in mild cognitive impairment. *Neurology*. 1999;52(7):1397-1403. doi:10.1212/wnl.52.7.1397

4. Schocke MFH, Seppi K, Esterhammer R, et al. Diffusion-weighted MRI differentiates the Parkinson variant of multiple system atrophy from PD. *Neurology*. 2002;58(4):575-580. doi:10.1212/WNL.58.4.575

5. Pujadas S, Reddy GP, Weber O, Lee JJ, Higgins CB. MR imaging assessment of cardiac function. *J Magn Reson Imaging*. 2004;19(6):789-799. doi:10.1002/jmri.20079

6. Li W, Stern JS, Mai VM, Pierchala LN, Edelman RR, Prasad P V. MR assessment of left ventricular function: Quantitative comparison of fast imaging employing steady-state acquisition (FIESTA) with fast gradient echo cine technique. *J Magn Reson Imaging*. 2002;16(5):559-564. doi:10.1002/jmri.10197

7. Van Klaveren RJ, Oudkerk M, Prokop M, et al. Management of lung nodules detected by volume CT scanning. *N Engl J Med*. 2009;361(23):2221-2229.

doi:10.1056/NEJMoa0906085

8.   Bach PB, Mirkin JN, Oliver TK, et al. Benefits and harms of CT screening for lung cancer: A systematic review. *JAMA - J Am Med Assoc*. 2012;307(22):2418-2429. doi:10.1001/jama.2012.5521

9.   Brenner DJ, Elliston CD, Hall EJ, Berdon WE. Estimated risks of radiation-induced fatal cancer from pediatric CT. *Am J Roentgenol*. 2001;176(2):289-296. doi:10.2214/ajr.176.2.1760289

10.   Linton OW, Mettler FA. National conference on dose reduction in CT, with an emphasis on pediatric patients. *Am J Roentgenol*. 2003;181(2):321-329. doi:10.2214/ajr.181.2.1810321

11.   Huda W, Vance A. Patient Radiation Doses from Adult and Pediatric CT. *Am J Roentgenol*. 2007;188(2):540-546. doi:10.2214/AJR.06.0101

12.   Hahn AD, Higano NS, Walkup LL, et al. Pulmonary MRI of neonates in the intensive care unit using 3D ultrashort echo time and a small footprint MRI system. *J Magn Reson Imaging*. 2017;45(2):463-471. doi:10.1002/jmri.25394

13.   Higano NS, Fleck RJ, Spielberg DR, et al. Quantification of neonatal lung parenchymal density via ultrashort echo time MRI with comparison to CT. *J Magn Reson Imaging*. 2017;46(4):992-1000. doi:10.1002/jmri.25643

14.   Wild JM, Marshall H, Bock M, et al. MRI of the lung (1/3): Methods. *Insights Imaging*. 2012;3(4):345-353. doi:10.1007/s13244-012-0176-x

15.   Zhu X, Chan M, Lustig M, Johnson KM, Larson PEZ. Iterative motion-compensation reconstruction ultra-short TE (iMoCo UTE) for high-resolution free-breathing pulmonary MRI. *Magn Reson Med*. 2020;83(4):1208-1221.

doi:10.1002/mrm.27998

16.   Geva T. Magnetic Resonance Imaging: Historical Perspective. *J Cardiovasc Magn Reson*. 2006;8(4):573-580. doi:10.1080/10976640600755302

17.   Brown RW, Cheng YCN, Haacke EM, Thompson MR, Venkatesan R. *Magnetic Resonance Imaging: Physical Principles and Sequence Design: Second Edition*. Vol 9780471720.; 2014. doi:10.1002/9781118633953

18.   Zur Y, Wood ML, Neuringer LJ. Spoiling of transverse magnetization in steady-state sequences. *Magn Reson Med*. 1991;21(2):251-263. doi:10.1002/mrm.1910210210

19.   Hargreaves B. Rapid gradient-echo imaging. *J Magn Reson Imaging*. 2012;36(6):1300-1313. doi:10.1002/jmri.23742

20.   Shattuck MD, Gewalt SL, Glover GH, Hedlund LW, Johnson GA, Fitzsimons EG. MR microimaging of the lung using volume projection encoding. *Magn Reson Med*. 1997;38(6):938-942. doi:10.1002/mrm.1910380613

21.   Gurney PT, Hargreaves BA, Nishimura DG. Design and analysis of a practical 3D cones trajectory. *Magn Reson Med*. 2006;55(3):575-582. doi:10.1002/mrm.20796

22.   Zucker EJ, Cheng JY, Haldipur A, Carl M, Vasanawala SS. Free-breathing pediatric chest MRI: Performance of self-navigated golden-angle ordered conical ultrashort echo time acquisition. *J Magn Reson Imaging*. 2018;47(1):200-209. doi:10.1002/jmri.25776

23.   Barger A V., Block WF, Toropov Y, Grist TM, Mistretta CA. Time-resolved contrast-enhanced imaging with isotropic resolution and broad coverage using an undersampled 3D projection trajectory. *Magn Reson Med*. 2002;48(2):297-305.

doi:10.1002/mrm.10212

24.   Madelin G. Sodium Magnetic Resonance Imaging: Biomedical Applications. December 2012. http://arxiv.org/abs/1212.4400. Accessed February 27, 2020.

25.   Macovski A. Noise in MRI. *Magn Reson Med*. 1996;36(3):494-497. doi:10.1002/mrm.1910360327

26.   Zhu Z, Zhu X, Ohliger MA, et al. Coil combination methods for multi-channel hyperpolarized 13 C imaging data from human studies. *J Magn Reson*. 2019;301:73-79. doi:10.1016/j.jmr.2019.01.015

27.   Nazareth JL. Conjugate gradient method. *Wiley Interdiscip Rev Comput Stat*. 2009;1(3):348-353. doi:10.1002/wics.13

28.   Lustig M, Donoho DL, Santos JM, Pauly JM. Compressed sensing MRI: A look at how CS can improve on current imaging techniques. *IEEE Signal Process Mag*. 2008;25(2):72-82. doi:10.1109/MSP.2007.914728

29.   Togao O, Tsuji R, Ohno Y, Dimitrov I, Takahashi M. Ultrashort echo time (UTE) MRI of the lung: Assessment of tissue density in the lung parenchyma. *Magn Reson Med*. 2010;64(5):1491-1498. doi:10.1002/mrm.22521

30.   Krohmer S, Meier K, Sorge I, Hirsch W, Till H, Weber D. MRI of the lungs in children. *Eur J Radiol*. 2008;68(2):278-288. doi:10.1016/j.ejrad.2008.05.017

31.   Pearce MS, Salotti JA, Little MP, et al. Radiation exposure from CT scans in childhood and subsequent risk of leukaemia and brain tumours: A retrospective cohort study. *Lancet*. 2012;380(9840):499-505. doi:10.1016/S0140-6736(12)60815-0

32.   Yu J, Xue Y, Song HK. Comparison of lung T2* during free-breathing at 1.5 T and

3.0 T with ultrashort echo time imaging. *Magn Reson Med*. 2011;66(1):248-254. doi:10.1002/mrm.22829

33. Larson PEZ, Johnson KM, Hope MD, et al. Detection of Small Pulmonary Nodules with Ultrashort Echo Time Sequences in Oncology Patients by Using a PET/MR System. *Radiology*. 2015;278(1):239-246. doi:10.1148/radiol.2015150489

34. Jiang W, Ong F, Johnson KM, et al. Motion Robust High Resolution 3D Free-Breathing Pulmonary MRI Using Dynamic 3D Image Self-Navigator. 2018;2967(October 2017):2954-2967. doi:10.1002/mrm.26958

35. Weiger M, Brunner DO, Dietrich BE, Müller CF, Pruessmann KP. ZTE imaging in humans. *Magn Reson Med*. 2013;70(2):328-332. doi:10.1002/mrm.24816

36. Johnson KM, Fain SB, Schiebler ML, Nagle S. Optimized 3D ultrashort echo time pulmonary MRI. *Magn Reson Med*. 2013;70(5):1241-1250. doi:10.1002/mrm.24570

37. Zucker EJ, Cheng JY, Haldipur A, Carl M, Vasanawala SS. Free-breathing pediatric chest MRI: Performance of self-navigated golden-angle ordered conical ultrashort echo time acquisition. *J Magn Reson Imaging*. 2018;47(1):200-209. doi:10.1002/jmri.25776

38. Delacoste J, Chaptinel J, Beigelman-Aubry C, Piccini D, Sauty A, Stuber M. A double echo ultra short echo time (UTE) acquisition for respiratory motion-suppressed high resolution imaging of the lung. *Magn Reson Med*. 2018;79(4):2297-2305. doi:10.1002/mrm.26891

39. Higano NS, Thomen RP, Cao X, et al. Retrospective respiratory self-gating and removal of bulk motion in pulmonary UTE MRI of neonates and adults. *Magn*

Reson Med. 2016;77(3):1284-1295. doi:10.1002/mrm.26212

40. Weick S, Völker M, Hemberger K, et al. Desynchronization of Cartesian k-space sampling and periodic motion for improved retrospectively self-gated 3D lung MRI using quasi-random numbers. *Magn Reson Med*. 2016;00(July 2015). doi:10.1002/mrm.26159

41. Holmes JE, Bydder GM. MR imaging with ultrashort TE (UTE) pulse sequences: Basic principles. *Radiography*. 2005;11(3):163-174. doi:10.1016/j.radi.2004.07.007

42. Mendes Pereira L, Wech T, Weng AM, et al. UTE-SENCEFUL: first results for 3D high-resolution lung ventilation imaging. *Magn Reson Med*. 2018;(April):1-10. doi:10.1002/mrm.27576

43. Tibiletti M, Paul J, Bianchi A, et al. Multistage three-dimensional UTE lung imaging by image-based self-gating. *Magn Reson Med*. 2016;75(3):1324-1332. doi:10.1002/mrm.25673

44. Josan S, Yen YF, Hurd R, Pfefferbaum A, Spielman D, Mayer D. Application of double spin echo spiral chemical shift imaging to rapid metabolic mapping of hyperpolarized [1 -13C]-pyruvate. *J Magn Reson*. 2011;209(2):332-336. doi:10.1016/j.jmr.2011.01.010

45. Bonanno G, Puy G, Wiaux Y, Van Heeswijk RB, Piccini D, Stuber M. Self-navigation with compressed sensing for 2D translational motion correction in free-breathing coronary MRI: A feasibility study. *PLoS One*. 2014;9(8). doi:10.1371/journal.pone.0105523

46. Pallack M, Hricak H, Higgins C, McNamara M, Ehman R. Magnetic resonance

imaging with respiratory gating: techniques and advantages. *Am J Roentgenol*. 1984;143(6):1175-1182. doi:10.2214/ajr.143.6.1175

47. Cheng JY, Zhang T, Ruangwattanapaisarn N, et al. Free-breathing pediatric MRI with nonrigid motion correction and acceleration. *J Magn Reson Imaging*. 2015;42(2):407-420. doi:10.1002/jmri.24785

48. Zhang T, Yousaf U, Hsiao A, et al. Clinical performance of a free-breathing spatiotemporally accelerated 3-D time-resolved contrast-enhanced pediatric abdominal MR angiography. *Pediatr Radiol*. 2015;45(11):1635-1643. doi:10.1007/s00247-015-3384-y

49. Feng L, Axel L, Chandarana H, Block KT, Sodickson DK, Otazo R. XD-GRASP: Golden-angle radial MRI with reconstruction of extra motion-state dimensions using compressed sensing. *Magn Reson Med*. 2015;00(October 2014):n/a-n/a. doi:10.1002/mrm.25665

50. Feng L, Delacoste J, Smith D, et al. Simultaneous Evaluation of Lung Anatomy and Ventilation Using 4D Respiratory-Motion-Resolved Ultrashort Echo Time Sparse MRI. *J Magn Reson Imaging*. 2019;49(2):411-422. doi:10.1002/jmri.26245

51. Jung H, Sung K, Nayak KS, Kim EY, Ye JC. K-t FOCUSS: A general compressed sensing framework for high resolution dynamic MRI. *Magn Reson Med*. 2009;61(1):103-116. doi:10.1002/mrm.21757

52. Pang J, Bhat H, Sharif B, et al. Whole-Heart Coronary MRA with 100 % Respiratory Gating Efficiency : Self-Navigated Three-Dimensional Retrospective Image-Based Motion Correction (TRIM). 2014;74:67-74. doi:10.1002/mrm.24628

53. Rank CM, Heußer T, Wetscherek A, Kachelrieß M. Respiratory Motion

Compensation for Simultaneous PET / MR based on strongly undersampled radial MR data. *EJNMMI Phys*. 2015;2(Suppl 1):A24. doi:10.1186/2197-7364-2-S1-A24

54.   Grimm R, Fürst S, Dregely I, et al. Self-gated radial MRI for respiratory motion compensation on hybrid PET/MR systems. *Lect Notes Comput Sci (including Subser Lect Notes Artif Intell Lect Notes Bioinformatics)*. 2013;8151 LNCS(PART 3):17-24. doi:10.1007/978-3-642-40760-4_3

55.   Botnar RM, Nekolla SG, Prieto C, Munoz C, Neji R, Kunze KP. Respiratory- and cardiac motion-corrected simultaneous whole-heart PET and dual phase coronary MR angiography. *Magn Reson Med*. 2018;81(3):1671-1684. doi:10.1002/mrm.27517

56.   Reiner CS, Stolzmann P, Husmann L, et al. Protocol requirements and diagnostic value of PET/MR imaging for liver metastasis detection. *Eur J Nucl Med Mol Imaging*. 2014;41(4):649-658. doi:10.1007/s00259-013-2654-x

57.   Petibon Y, Ouyang J, Zhu X, et al. Cardiac motion compensation and resolution modeling in simultaneous PET-MR: A cardiac lesion detection study. *Phys Med Biol*. 2013;58(7):2085-2102. doi:10.1088/0031-9155/58/7/2085

58.   Batchelor PG, Atkinson D, Irarrazaval P, Hill DLG, Hajnal J, Larkman D. Matrix description of general motion correction applied to multishot images. *Magn Reson Med*. 2005;54(5):1273-1280. doi:10.1002/mrm.20656

59.   Rank CM, Heußer T, Buzan MTA, et al. 4D respiratory motion-compensated image reconstruction of free-breathing radial MR data with very high undersampling. *Magn Reson Med*. 2016;00(February). doi:10.1002/mrm.26206

60. Pang J, Chen Y, Fan Z, et al. High efficiency coronary MR angiography with nonrigid cardiac motion correction. *Magn Reson Med*. 2016;76(5):1345-1353. doi:10.1002/mrm.26332

61. Prieto C, Doneva M, Usman M, et al. Highly efficient respiratory motion compensated free-breathing coronary MRA using golden-step Cartesian acquisition. *J Magn Reson Imaging*. 2015;41(3):738-746. doi:10.1002/jmri.24602

62. Cruz G, Atkinson D, Henningsson M, Botnar RM, Prieto C. Highly efficient nonrigid motion-corrected 3D whole-heart coronary vessel wall imaging. *Magn Reson Med*. 2017;77(5):1894-1908. doi:10.1002/mrm.26274

63. Cruz G, Atkinson D, Buerger C, Schaeffter T, Prieto C. Accelerated motion corrected three-dimensional abdominal MRI using total variation regularized SENSE reconstruction. *Magn Reson Med*. 2016;75(4):1484-1498. doi:10.1002/mrm.25708

64. J.-P.Thirion. Image matching as a diffusion process : an analogy with Maxwell ' s demons. *Med Image Anal*. 2004;2(3):243-260.

65. Knoll F, Bredies K, Pock T, Stollberger R. Second order total generalized variation (TGV) for MRI. *Magn Reson Med*. 2011;65(2):480-491. doi:10.1002/mrm.22595

66. Zhang T, Cheng JY, Chen Y, Nishimura DG, Pauly JM, Vasanawala SS. Robust self-navigated body MRI using dense coil arrays. *Magn Reson Med*. 2016;76(1):197-205. doi:10.1002/mrm.25858

67. Chambolle A, Pock T. A First-Order Primal-Dual Algorithm for Convex Problems with Applications to Imaging. 2011:120-145. doi:10.1007/s10851-010-0251-1

68. Winkler SA, Corea J, Lechêne B, et al. Evaluation of a Flexible 12-Channel

Screen-printed Pediatric MRI Coil. *Radiology*. 2019:181883. doi:10.1148/radiol.2019181883

69.   Uecker M, Tamir JI, Ong F, Lustig M. The BART Toolbox for Computational Magnetic Resonance Imaging. In: *ISMRM*. ; 2016:DOI:10.5281/zenodo.592960. doi:10.5281

70.   Hahn AD, Higano NS, Walkup LL, et al. Pulmonary MRI of Neonates in the Intensive Care Unit Using 3D Ultrashort Echo Time and a Small Footprint MRI System. *J Magn Reson Imaging*. 2016;45(2):463-471. doi:10.1002/jmri.25394

71.   Higano NS, Spielberg DR, Fleck RJ, et al. Neonatal pulmonary magnetic resonance imaging of bronchopulmonary dysplasia predicts short-term clinical outcomes. *Am J Respir Crit Care Med*. 2018;198(10):1302-1311. doi:10.1164/rccm.201711-2287OC

72.   Avants BB, Tustison NJ, Song G, Cook PA, Klein A, Gee JC. A reproducible evaluation of ANTs similarity metric performance in brain image registration. *Neuroimage*. 2011;54(3):2033-2044. doi:10.1016/j.neuroimage.2010.09.025

73.   Yin Y, Hoffman EA, Lin CL. Mass preserving nonrigid registration of CT lung images using cubic B-spline. *Med Phys*. 2009;36(9):4213-4222. doi:10.1118/1.3193526

74.   Zhang T, Pauly JM, Levesque IR. Accelerating Parameter Mapping with a Locally Low Rank Constraint. 2015;661:655-661. doi:10.1002/mrm.25161

75.   Metz CT, Klein S, Schaap M, Walsum T Van, Niessen WJ. Nonrigid registration of dynamic medical imaging data using n D + t B-splines and a groupwise optimization approach. *Med Image Anal*. 2011;15(2):238-249.

doi:10.1016/j.media.2010.10.003

76. Small, J. H., Flower, C. D. R., Traill, Z. C., & Gleeson F V. Air-trapping in Extrinsic Allergic Alveolitis on Computed Tomography. *Clin Radiol*. 1996;51(10):684-688.

77. Morokoff WJ, Caflisch RE. Quasi-Random Sequences and Their Discrepancies. *SIAM J Sci Comput*. 1994;15(6):1251-1279. doi:10.1137/0915077

78. Wong STS, Roos MS. A strategy for sampling on a sphere applied to 3D selective RF pulse design. *Magn Reson Med*. 1994;32(6):778-784. doi:10.1002/mrm.1910320614

79. Chan RW, Ramsay EA, Cunningham CH, Plewes DB. Temporal stability of adaptive 3D radial MRI using multidimensional golden means. *Magn Reson Med*. 2009;61(2):354-363. doi:10.1002/mrm.21837

80. Furnival T, Leary RK, Midgley PA. Denoising time-resolved microscopy image sequences with singular value thresholding. *Ultramicroscopy*. 2017;178:112-124. doi:10.1016/j.ultramic.2016.05.005

81. Nakarmi U, Wang Y, Lyu J, Liang D, Ying L. A Kernel-Based Low-Rank (KLR) Model for Low-Dimensional Manifold Recovery in Highly Accelerated Dynamic MRI. *IEEE Trans Med Imaging*. 2017;36(11):2297-2307. doi:10.1109/TMI.2017.2723871

82. Ong F, Lustig M. Beyond Low Rank + Sparse: Multiscale Low Rank Matrix Decomposition. *IEEE J Sel Top Signal Process*. 2016;10(4):672-687. doi:10.1109/JSTSP.2016.2545518

83. Otazo R, Candès E, Sodickson DK. Low-rank plus sparse matrix decomposition for accelerated dynamic MRI with separation of background and dynamic

components. *Magn Reson Med*. 2015;73(3):1125-1136. doi:10.1002/mrm.25240

84. Peng Y, Ganesh A, Wright J, Xu W, Ma Y. RASL: Robust alignment by sparse
     and low-rank decomposition for linearly correlated images. *IEEE Trans Pattern
     Anal Mach Intell*. 2012;34(11):2233-2246. doi:10.1109/TPAMI.2011.282

85. Asif MS, Hamilton L, Brummer M, Romberg J. Motion-adaptive spatio-temporal
     regularization for accelerated dynamic MRI. *Magn Reson Med*. 2013;70(3):800-
     812. doi:10.1002/mrm.24524

86. Yoon H, Kim KS, Kim D, Bresler Y, Ye JC. Motion adaptive patch-based low-rank
     approach for compressed sensing cardiac cine MRI. *IEEE Trans Med Imaging*.
     2014;33(11):2069-2085. doi:10.1109/TMI.2014.2330426

87. Chen X, Salerno M, Yang Y, Epstein FH. Motion-compensated compressed
     sensing for dynamic contrast-enhanced MRI using regional spatiotemporal
     sparsity and region tracking: Block low-rank sparsity with motion-guidance
     (BLOSM). *Magn Reson Med*. 2014;72(4):1028-1038. doi:10.1002/mrm.25018

88. Ledesma-Carbayo MJ, Kellman P, Arai AE, McVeigh ER. Motion corrected free-
     breathing delayed-enhancement imaging of myocardial infarction using nonrigid
     registration. *J Magn Reson Imaging*. 2007;26(1):184-190. doi:10.1002/jmri.20957

89. El-Gamal FEZA, Elmogy M, Atwan A. Current trends in medical image registration
     and fusion. *Egypt Informatics J*. 2016;17(1):99-124. doi:10.1016/j.eij.2015.09.002

90. Vercauteren T, Pennec X, Perchant A, Ayache N. Diffeomorphic demons: efficient
     non-parametric image registration. *Neuroimage*. 2009;45(1 Suppl):S61-S72.
     doi:10.1016/j.neuroimage.2008.10.040

91. Boyd S, Parikh N, Chu E, Peleato B, Eckstein J. Distributed optimization and

statistical learning via the alternating direction method of multipliers. *Found Trends Mach Learn*. 2010;3(1):1-122. doi:10.1561/2200000016

92. Cai JF, Candès EJ, Shen Z. A singular value thresholding algorithm for matrix completion. *SIAM J Optim*. 2010;20(4):1956-1982. doi:10.1137/080738970

93. Zhang T, Cheng JY, Potnick AG, et al. Fast pediatric 3D free-breathing abdominal dynamic contrast enhanced MRI with high spatiotemporal resolution. *J Magn Reson Imaging*. 2015;41(2):460-473. doi:10.1002/jmri.24551

94. Tamir JI, Uecker M, Chen W, et al. T2 shuffling: Sharp, multicontrast, volumetric fast spin-echo imaging. *Magn Reson Med*. 2017;77(1):180-195. doi:10.1002/mrm.26102

95. Ma D, Gulani V, Seiberlich N, et al. Magnetic resonance fingerprinting. *Nature*. 2013;495(7440):187-192. doi:10.1038/nature11971

96. Cao P, Zhu X, Tang S, Leynes A, Jakary A, Larson PEZ. Shuffled magnetization-prepared multicontrast rapid gradient-echo imaging. *Magn Reson Med*. 2018;79(1):62-70. doi:10.1002/mrm.26986

97. Ong F, Zhu X, Cheng JY, et al. Extreme MRI: Large-Scale Volumetric Dynamic Imaging from Continuous Non-Gated Acquisitions. September 2019. http://arxiv.org/abs/1909.13482. Accessed February 27, 2020.

98. Feng L, Wen Q, Huang C, Tong A, Liu F, Chandarana H. GRASP-Pro: imProving GRASP DCE-MRI through self-calibrating subspace-modeling and contrast phase automation. *Magn Reson Med*. 2020;83(1):94-108. doi:10.1002/mrm.27903

99. Feng L, Delacoste J, Smith D, et al. Simultaneous Evaluation of Lung Anatomy and Ventilation Using 4D Respiratory- Motion-Resolved Ultrashort Echo Time

Sparse MRI. 2018:1-12. doi:10.1002/jmri.26245

100. Tamir JI, Taviani V, Alley MT, et al. Targeted rapid knee MRI exam using T2 shuffling. *J Magn Reson Imaging*. 2019;49(7):e195-e204. doi:10.1002/jmri.26600

101. Anderson MJ, Tamir JI, Turek JS, et al. Clinically Deployed Distributed Magnetic Resonance Imaging Reconstruction: Application to Pediatric Knee Imaging. September 2018. http://arxiv.org/abs/1809.04195. Accessed March 2, 2020.

102. Sekihara K. Steady-State Magnetizations in Rapid NMR Imaging Using Small Flip Angles and Short Repetition Intervals. *IEEE Trans Med Imaging*. 1987;6(2):157-164. doi:10.1109/TMI.1987.4307816

103. Wei L, Hee KS. Improved signal spoiling in fast radial gradient-echo imaging: Applied to accurate t1 mapping and flip angle correction. *Magn Reson Med*. 2009;62(5):1185-1194. doi:10.1002/mrm.22089

104. Weiger M, Brunner DO, Dietrich BE, Müller CF, Pruessmann KP. ZTE imaging in humans. *Magn Reson Med*. 2013;70(2):328-332. doi:10.1002/mrm.24816

105. Roeloffs V, Voit D, Frahm J. Spoiling without additional gradients: Radial FLASH MRI with randomized radiofrequency phases. *Magn Reson Med*. 2016;75(5):2094-2099. doi:10.1002/mrm.25809

106. Jaynes ET. Matrix treatment of nuclear induction. *Phys Rev*. 1955;98(4):1099-1105. doi:10.1103/PhysRev.98.1099

107. Bloch F. Nuclear induction. *Phys Rev*. 1946;70(7-8):460-474. doi:10.1103/PhysRev.70.460

108. Weigel M. Extended phase graphs: Dephasing, RF pulses, and echoes - Pure and simple. *J Magn Reson Imaging*. 2015;41(2):266-295. doi:10.1002/jmri.24619

109. Robison RK, Anderson AG, Pipe JG. Three-dimensional ultrashort echo-time imaging using a FLORET trajectory. *Magn Reson Med*. 2017;78(3):1038-1049. doi:10.1002/mrm.26500

110. Fessler J. Model-based image reconstruction for MRI. In: *IEEE Signal Processing Magazine*. Vol 27. Institute of Electrical and Electronics Engineers Inc.; 2010:81-89. doi:10.1109/MSP.2010.936726

111. Bianchi A, Tibiletti M, Kjørstad Å, et al. Three-dimensional accurate detection of lung emphysema in rats using ultra-short and zero echo time MRI. *NMR Biomed*. 2015;28(11):1471-1479. doi:10.1002/nbm.3417

112. Weiger M, Wu M, Wurnig MC, et al. Rapid and robust pulmonary proton ZTE imaging in the mouse. *NMR Biomed*. 2014;27(9):1129-1134. doi:10.1002/nbm.3161

113. Bae K, Jeon KN, Hwang MJ, et al. Comparison of lung imaging using three-dimensional ultrashort echo time and zero echo time sequences: preliminary study. *Eur Radiol*. 2019;29(5):2253-2262. doi:10.1007/s00330-018-5889-x

114. Yuan J, Hu Y, Menini A, et al. Near-silent distortionless DWI using magnetization-prepared RUFIS. *Magn Reson Med*. 2019. doi:10.1002/mrm.28106

115. Gibiino F, Sacolick L, Menini A, Landini L, Wiesinger F. Free-breathing, zero-TE MR lung imaging. *Magn Reson Mater Physics, Biol Med*. 2015;28(3):207-215. doi:10.1007/s10334-014-0459-y

116. Campbell-Washburn AE, Ramasawmy R, Restivo MC, et al. Opportunities in interventional and diagnostic imaging by using high-performance low-field-strength MRI. *Radiology*. 2019;293(2):384-393. doi:10.1148/radiol.2019190452

117. Chang KJ, Kamel IR, Macura KJ, Bluemke DA. 3.0-T MR imaging of the Abdomen: Comparison with 1.5 T. *Radiographics*. 2008;28(7):1983-1998. doi:10.1148/rg.287075154

118. Grist TM. The next chapter in MRI: Back to the future? *Radiology*. 2019;293(2):394-395. doi:10.1148/radiol.2019192011

119. Marques JP, Simonis FFJ, Webb AG. Low-field MRI: An MR physics perspective. *J Magn Reson Imaging*. 2019;49(6):1528-1542. doi:10.1002/jmri.26637

120. Zha W, Kruger SJ, Johnson KM, et al. Pulmonary ventilation imaging in asthma and cystic fibrosis using oxygen-enhanced 3D radial ultrashort echo time MRI. *J Magn Reson Imaging*. 2018;47(5):1287-1297. doi:10.1002/jmri.25877

121. Ohno Y, Koyama H, Nogami M, et al. Dynamic oxygen-enhanced MRI versus quantitative CT: pulmonary functional loss assessment and clinical stage classification of smoking-related COPD. *AJR Am J Roentgenol*. 2008;190(2). doi:10.2214/AJR.07.2511

122. Ohno Y, Hatabu H, Takenaka D, Van Cauteren M, Fujii M, Sugimura K. Dynamic oxygen-enhanced MRI reflects diffusing capacity of the lung. *Magn Reson Med*. 2002;47(6):1139-1144. doi:10.1002/mrm.10168

123. Edelman RR, Hatabu H, Tadamura E, Li W, Prasad P V. Noninvasive assessment of regional ventilation in the human lung using oxygen-enhanced magnetic resonance imaging. *Nat Med*. 1996;2(11):1236-1239. doi:10.1038/nm1196-1236

124. Swensen SJ, Jett JR, Hartman TE, et al. CT screening for lung cancer: Five-year prospective experience. *Radiology*. 2005;235(1):259-265. doi:10.1148/radiol.2351041662

125. Swensen SJ, Jett JR, Sloan JA, et al. Screening for lung cancer with low-dose spiral computed tomography. *Am J Respir Crit Care Med*. 2002;165(4):508-513. doi:10.1164/ajrccm.165.4.2107006

126. Yau G, Lock M, Rodrigues G. Systematic review of baseline low-dose CT lung cancer screening. *Lung Cancer*. 2007;58(2):161-170. doi:10.1016/j.lungcan.2007.07.006

127. Marshall HM, Bowman R V., Yang IA, Fong KM, Berg CD. Screening for lung cancer with low-dose computed tomography: A review of current status. *J Thorac Dis*. 2013;5(SUPPL.5):S524. doi:10.3978/j.issn.2072-1439.2013.09.06

128. Wu D, Kim K, El Fakhri G, Li Q. Iterative Low-dose CT Reconstruction with Priors Trained by Artificial Neural Network. *IEEE Trans Med Imaging*. September 2017. doi:10.1109/TMI.2017.2753138

129. Kim K, El Fakhri G, Li Q. Low-dose CT reconstruction using spatially encoded nonlocal penalty. *Med Phys*. 2017;44(10):e376-e390. doi:10.1002/mp.12523

130. Willemink MJ, Noël PB. The evolution of image reconstruction for CT—from filtered back projection to artificial intelligence. *Eur Radiol*. 2019;29(5):2185-2195. doi:10.1007/s00330-018-5810-7

131. Lee H, Lee J, Kim H, Cho B, Cho S. Deep-Neural-Network-Based Sinogram Synthesis for Sparse-View CT Image Reconstruction. *IEEE Trans Radiat Plasma Med Sci*. 2018;3(2):109-119. doi:10.1109/trpms.2018.2867611

132. Chen H, Zhang Y, Kalra MK, et al. Low-Dose CT with a residual encoder-decoder convolutional neural network. *IEEE Trans Med Imaging*. 2017;36(12):2524-2535. doi:10.1109/TMI.2017.2715284

133. Yang Q, Yan P, Zhang Y, et al. Low-Dose CT Image Denoising Using a Generative Adversarial Network With Wasserstein Distance and Perceptual Loss. *IEEE Trans Med Imaging*. 2018;37(6):1348-1357. doi:10.1109/TMI.2018.2827462

134. Kang E, Chang W, Yoo J, Ye JC. Deep Convolutional Framelet Denosing for Low-Dose CT via Wavelet Residual Network. *IEEE Trans Med Imaging*. 2018;37(6):1358-1369. doi:10.1109/TMI.2018.2823756

Publishing Agreement

It is the policy of the University to encourage open access and broad distribution of all theses, dissertations, and manuscripts. The Graduate Division will facilitate the distribution of UCSF theses, dissertations, and manuscripts to the UCSF Library for open access and distribution. UCSF will make such theses, dissertations, and manuscripts accessible to the public and will take reasonable steps to preserve these works in perpetuity.

I hereby grant the non-exclusive, perpetual right to The Regents of the University of California to reproduce, publicly display, distribute, preserve, and publish copies of my thesis, dissertation, or manuscript in any form or media, now existing or later derived, including access online for teaching, research, and public service purposes.

DocuSigned by:

Xucheng Zhu

—1B04EAE39A954F4...   Author Signature

3/12/2020

Date